

The Vera C. Rubin Observatory Data Preview 1

1
2 VERA C. RUBIN OBSERVATORY TEAM,¹ TATIANA ACERO-CUELLAR ² EMILY ACOSTA ¹ CHRISTINA L. ADAIR ³
3 PRAKRUTH ADARI ⁴ JENNIFER K. ADELMAN-McCARTHY ⁵ ANASTASIA ALEXOV ¹ RUSS ALLBERY ¹
4 ROBYN ALLSMAN,¹ YUSRA ALSAYYAD ⁶ JHONATAN AMADO ⁵ NATHAN AMOUROUX ⁷ PIERRE ANTILOGUS ⁸
5 ALEXIS ARACENA ALCAYAGA,⁹ GONZALO ARAVENA-ROJAS ⁹ CLAUDIO H. ARAYA CORTES,⁹ ÉRIC AUBOURG ¹⁰
6 TIM S. AXELROD ¹¹ JOHN BANOVETZ ¹² CARLOS BARRÍA,⁹ AMANDA E. BAUER ¹³ BRIAN J. BAUMAN,¹⁴
7 ELLEN BECHTOL ¹⁵ KEITH BECHTOL ^{1,16} ANDREW C. BECKER ¹⁷ VALERIE R. BECKER ¹⁸ MARK G. BECKETT ¹⁹
8 ERIC C. BELLM ²⁰ PEDRO H. BERNARDINELLI ²¹ FEDERICA B. BIANCO ^{2,22,23} ROBERT D. BLUM ¹⁸
9 JOANNE BOGART,²⁴ ADAM BOLTON ³ MICHAEL T. BOOTH,¹ JAMES F. BOSCH ⁶ ALEXANDRE BOUCAUD ²⁵
10 DOMINIQUE BOUTIGNY ⁷ ROBERT A. BOVILL,¹ ANDREW BRADSHAW,^{3,24} JOHAN BREGEON ²⁶ BRIAN J. BRONDEL ²⁷
11 ALEXANDER BROUGHTON ²⁴ AUDREY BUDLONG ²⁸ DIMITRI BUFFAT,²⁶ RODOLFO CANESTRARI ²⁹
12 NEVEN CAPLAR ²⁰ JEFFREY L. CARLIN ¹ ROSS CEBALLO ¹⁸ COLIN ORION CHANDLER ^{30,20,31}
13 CHIHWAY CHANG ³² GLENAVER CHARLES-EMERSON,¹ HSIN-FANG CHIANG ³ JAMES CHIANG ²⁴ YUMI CHOI ³³
14 ERIC J. CHRISTENSEN,⁹ CHARLES F. CLAVER,¹ ANDY W. CLEMENTS,¹ JOSEPH J. COCKRUM,¹ FRANCO COLLEONI,⁹
15 CÉLINE COMBET ²⁶ ANDREW J. CONNOLLY ²¹ JULIO EDUARDO CONSTANZO CÓRDOVA ⁹ HANS E CONTRERAS,⁹
16 JOHN FRANKLIN CRENSHAW ²¹ SYLVIE DAGORET-CAMPAGNE ³⁴ SCOTT F. DANIEL,²⁰ FELIPE DARUICH,⁹
17 GUILLAUME DAUBARD ⁸ GREG DAUES,³⁵ ERIK DENNIHY ¹ STEPHANIE J. H. DEPPE ¹⁸ SETH W. DIGEL ³
18 PETER E. DOHERTY,³⁶ ALEX DRLICA-WAGNER ⁵ GREGORY P. DUBOIS-FELSMANN ³⁷ FROSSIE ECONOMOU ¹
19 ORION EIGER ^{3,24} LUKAS EISERT ³ ALAN M. EISNER ³⁸ ANTHONY ENGLERT ³⁹ BADEN ERB,⁹ JUAN A. FABREGA,⁹
20 PARKER FAGRELIUS,¹ KEVIN FANNING ³ ANGELO FAUSTI NETO ¹ PETER S. FERGUSON ^{21,16} AGNÈS FERTÉ ³
21 MERLIN FISHER-LEVINE ⁴⁰ GLORIA FONSECA ALVAREZ ³³ MICHAEL D. FOSS,³ DOMINIQUE FOUCHEZ ⁴¹
22 DAN C. FUCHS ³ EMMANUEL GANGLER ⁴² IGOR GAPONENKO,³ JULEN GARCIA ⁴³ JOHN H GATES,³
23 RANPAL K. GILL ²⁷ ENRICO GIRO ⁴⁴ THOMAS GLANZMAN ³ ROBINSON GODOY,⁹ IAIN GOODENOW,¹
24 MIRANDA R. GORSUCH ¹⁶ MICHELLE GOWER ³⁵ MIKAEL GRANVIK ^{45,46} SARAH GREENSTREET ³³ WEN GUAN ¹²
25 THIBAUT GUILLEMIN ⁷ LEANNE P. GUY ⁹ DIANE HASCALL,³ AREN NATHANIEL HEINZE ²¹ FABIO HERNANDEZ ⁴⁷
26 KENNETH HERNER ⁵ ARDIS HERROLD,¹ CLARE R. HIGGS ¹⁸ JOSHUA HOBLITT ¹ ERIN LEIGH HOWARD ²⁰
27 MINHEE HYUN ⁹ PATRICK INGRAHAM ¹¹ DAVID H. IRVING ¹⁸ ŽELJKO IVEZIĆ ^{1,20} SUZANNE H. JACOBY,¹
28 BUELL T. JANNUZI ⁴⁸ SREEVANI JARUGULA ⁵ M. JAMES JEE ^{49,50} TIM JENNESS ¹ TOBY C. JENNINGS ³
29 ANDREA JEREMIE ⁷ GARRETT JERNIGAN,^{51,*} DAVID JIMÉNEZ MEJÍAS,⁹ ANTHONY S. JOHNSON ³ R. LYNNE JONES ²⁰
30 ROGER WILLIAM LEWIS JONES ⁵² CLAIRE JURAMY-GILLES ⁸ MARIO JURÍĆ ²¹ STEVEN M. KAHN ⁵³
31 J. BRYCE KALMBACH ³ YIJUNG KANG ^{24,9} ARUN KANNAWADI ^{54,6} JEFFREY P. KANTOR,¹ EDWARD KARAVAKIS ¹²
32 KSHITIJ KALKAR ⁹ LEE S. KELVIN ⁶ IVAN V. KOTOV,¹² GÁBOR KOVÁCS ²¹ MIKOLAJ KOWALIK ³⁵
33 VICTOR L. KRABBENDAM,¹ K. SIMON KRUGHOFF ^{1,*} PETR KUBÁNEK ⁹ JACOB A. KURLANDER ²¹ MILE KUSULJA,²⁶
34 CRAIG S. LAGE ⁵⁰ PAULO J. A. LAGO ²⁷ KATHERINE LALLOTIS ⁵⁵ TRAVIS LANGE ³ DIDIER LAPORTE,⁸
35 RYAN M. LAU ³³ JUAN CARLOS LAZARTE,³ QUENTIN LE BOULC'H ⁴⁷ PIERRE-FRANÇOIS LÉGET ⁶
36 LAURENT LE GUILLOU ⁸ BENJAMIN LEVINE ⁴ MING LIANG,¹ SHUANG LIANG,³ KIAN-TAT LIM ³
37 ANJA VON DER LINDEN ⁴ HUAN LIN ⁵ MARGAUX LOPEZ ³ JUAN J. LOPEZ TORO,⁹ PETER LOVE,⁵²
38 ROBERT H. LUPTON ⁶ NATE B. LUST ⁶ LAUREN A. MACARTHUR ⁶ SEAN PATRICK MACBRIDE ⁵⁶
39 GREG M. MADEJSKI,²⁴ GABRIELE MAINETTI ⁴⁷ STEVEN J. MARGHEIM ²⁷ THOMAS W. MARKIEWICZ ³
40 PHIL MARSHALL ³ STUART MARSHALL,²⁴ GUIDO MAULEN,⁹ MORGAN MAY,^{57,12} JEREMY McCORMICK ³
41 DAVID MCKAY ⁵⁸ ROBERT MCKERCHER,¹ GUILLEM MEGIAS HOMAR ⁵⁹ AARON M. MEISNER ³³
42 FELIPE MENANTEAU,³⁵ HEATHER R. MENTZER ³⁸ KRISTEN METZGER,¹⁸ JOSHUA E. MEYERS ²⁴ MICHELLE MILLER,³³
43 DAVID J. MILLS,¹ JOACHIM MOEYENS ²¹ MARC MONIEZ,³⁴ FRED E. MOOLEKAMP ⁶⁰ C. A. L. MORALES MARÍN ⁹
44 FRITZ MUELLER ³ JAMES R. MULLANEY ⁶¹ FREDDY MUÑOZ ARANCIBIA,¹ KATE NAPIER ²⁴ HOMER NEAL,³
45 ERIC H. NEILSEN, JR. ⁵ JEREMY NEVEU ³⁴ TIMOTHY NOBLE,⁶² ERFAN NOURBAKHSH ⁶ KNUT OLSEN ³³
46 WILLIAM O'MULLANE ⁹ DMITRY ONOPRIENKO,³ MARCO ORIUNNO ³ SHAWN OSIER,³ RUSSELL E. OWEN,²⁰
47 AASHAY PAI ³² JOHN K. PAREJKO ²⁰ HYE YUN PARK ⁵⁴ JAMES B. PARSONS,^{35,*} MARIA T. PATTERSON ²⁰
48 MARINA S. PAVLOVIC ⁹ KARLA PEÑA RAMÍREZ ⁹ JOHN R. PETERSON ⁶³ STEPHEN R. PIETROWICZ ³⁵
49 ANDRÉS A. PLAZAS MALAGÓN ^{3,24} REBEKAH POLEN,⁵⁴ HANNAH MARY MARGARET POLLEK,³ PAUL A. PRICE ⁶

BRUNO C. QUINT¹, JOSÉ MIGUEL QUINTERO MARIN,⁹ MARKUS RABUS¹,⁶⁴ BENJAMIN RACINE¹,⁴¹ VELJKO RADEKA,¹²
 MANON RAMEL,²⁶ ARIANNA RANABHAT¹,⁶⁵ ANDREW P. RASMUSSEN¹,²⁴ DAVID A. RATHFELDER,⁶⁶
 MEREDITH L. RAWLS¹,^{20,21} SOPHIE L. REED¹,⁶ KEVIN A. REIL¹,³ DAVID J. REISS,²⁰ MICHAEL A. REUTER¹,¹
 TIAGO RIBEIRO¹,¹ MICKAEL RIGAUT¹,⁶⁷ VINCENT J. RIOT¹,¹⁴ STEVEN M. RITZ¹,³⁸ MARIO F. RIVERA RIVERA,⁹
 BRANT E. ROBERTSON¹,³⁸ WILLIAM ROBY¹,³⁷ GABRIELE RODEGHIERO¹,⁶⁸ AARON ROODMAN¹,²⁴
 LUCA ROSIGNOLI¹,^{69,68} CÉCILE ROUCELLE¹,²⁵ MATTHEW R. RUMORE¹,¹² STEFANO RUSSO,⁸ ELI S. RYKOFF¹,²⁴
 ANDREI SALNIKOV¹,³ BRUNO O. SÁNCHEZ¹,⁴¹ DAVID SANMARTIN¹,⁹ CLARE SAUNDERS¹,⁶ RAFE H. SCHINDLER,²⁴
 SAMUEL J. SCHMIDT¹,⁵⁰ JACQUES SEBAG,⁹ BRIAN SELVY,¹ EDGARD ESTEBAN SEPULVEDA VALENZUELA,⁹
 GONZALO SERICHE¹,⁹ JACQUELINE C. SERON-NAVARETE¹,⁹ IGNACIO SEVILLA-NOARBE¹,⁷⁰ ALYSHA SHUGART¹,⁹
 JONATHAN SICK¹,^{71,1} CRISTIÁN SILVA¹,⁹ MATHEW C. SIMS¹,⁷² JALADH SINGHAL¹,³⁷ KEVIN BENJAMIN SIRUNO,⁹
 COLIN T. SLATER¹,²⁰ BRIANNA M. SMART¹,²⁰ ADAM SNYDER¹,⁵⁰ CHRISTINE SOLDAHL,³
 IOANA SOTUELA ELORRIAGA¹,⁹ BRIAN STALDER¹,¹ HERNAN STOCKEBRAND¹,⁹ ALAN L. STRAUSS¹,¹⁸
 MICHAEL A. STRAUSS¹,⁶ KRZYSZTOF SUBERLAK¹,²⁰ IAN S. SULLIVAN¹,²⁰ JOHN D. SWINBANK¹,^{73,6} DIEGO TAPIA¹,⁹
 ALESSIO TARANTO¹,^{68,69} DAN S. TARANU¹,⁶ JOHN GREGG THAYER¹,³ SANDRINE THOMAS¹,¹
 ADAM J. THORNTON¹,¹ ROBERTO TIGHE,⁹ LAURA TORIBIO SAN CIPRIANO,⁷⁰ TE-WEI TSAI¹,¹ DOUGLAS L. TUCKER¹,⁵
 MAX TURRI,³ J. ANTHONY TYSON¹,⁵⁰ ELANA K. URBACH¹,⁷⁴ YOUSUKE UTSUMI¹,⁷⁵ BRIAN VAN KLAVEREN,³
 WOUTER VAN REEVEN¹,⁹ PETER ANTHONY VAUCHER¹,³ PAULINA VENEGAS,⁹ APRAJITA VERMA¹,⁷⁶
 ANTONIA SIERRA VILLARREAL¹,³ STELIOS VOUTSINAS¹,¹ CHRISTOPHER W. WALTER¹,⁵⁴ YUANKUN (DAVID) WANG¹,²¹
 CHRISTOPHER Z. WATERS¹,⁶ CHRISTINA C. WILLIAMS¹,³³ BETH WILLMAN¹,⁷⁷ MATTHIAS WITTGEN¹,³
 W. M. WOOD-VASEY¹,⁷⁸ WEI YANG¹,³ ZHAOYU YANG¹,¹² BRIAN P. YANNY¹,⁵ PETER YOACHIM¹,²⁰
 TIANQING ZHANG¹,⁷⁸ AND CONGHAO ZHOU¹,³⁸

¹Vera C. Rubin Observatory Project Office, 950 N. Cherry Ave., Tucson, AZ 85719, USA

²Department of Physics and Astronomy, University of Delaware, Newark, DE 19716-2570, USA

³SLAC National Accelerator Laboratory, 2575 Sand Hill Rd., Menlo Park, CA 94025, USA

⁴Department of Physics and Astronomy, Stony Brook University, Stony Brook, NY 11794, USA

⁵Fermi National Accelerator Laboratory, P. O. Box 500, Batavia, IL 60510, USA

⁶Department of Astrophysical Sciences, Princeton University, Princeton, NJ 08544, USA

⁷Université Savoie Mont-Blanc, CNRS/IN2P3, LAPP, 9 Chemin de Bellevue, F-74940 Annecy-le-Vieux, France

⁸Sorbonne Université, Université Paris Cité, CNRS/IN2P3, LPNHE, 4 place Jussieu, F-75005 Paris, France

⁹Vera C. Rubin Observatory, Avenida Juan Cisternas #1500, La Serena, Chile

¹⁰Université Paris Cité, CNRS/IN2P3, CEA, APC, 4 rue Elsa Morante, F-75013 Paris, France

¹¹Steward Observatory, The University of Arizona, 933 N. Cherry Ave., Tucson, AZ 85721, USA

¹²Brookhaven National Laboratory, Upton, NY 11973, USA

¹³Yerkes Observatory, 373 W. Geneva St., Williams Bay, WI 53191, USA

¹⁴Lawrence Livermore National Laboratory, 7000 East Avenue, Livermore, CA 94550, USA

¹⁵Wisconsin IceCube Particle Astrophysics Center, University of Wisconsin—Madison, Madison, WI 53706, USA

¹⁶Department of Physics, University of Wisconsin-Madison, Madison, WI 53706, USA

¹⁷Amazon Web Services, Seattle, WA 98121, USA

¹⁸Vera C. Rubin Observatory/NSF NOIRLab, 950 N. Cherry Ave., Tucson, AZ 85719, USA

¹⁹Institute for Astronomy, University of Edinburgh, Royal Observatory, Blackford Hill, Edinburgh EH9 3HJ, UK

²⁰University of Washington, Dept. of Astronomy, Box 351580, Seattle, WA 98195, USA

²¹Institute for Data-intensive Research in Astrophysics and Cosmology, University of Washington, 3910 15th Avenue NE, Seattle, WA 98195, USA

²²Joseph R. Biden, Jr., School of Public Policy and Administration, University of Delaware, Newark, DE 19717 USA

²³Data Science Institute, University of Delaware, Newark, DE 19717 USA

²⁴Kavli Institute for Particle Astrophysics and Cosmology, SLAC National Accelerator Laboratory, 2575 Sand Hill Rd., Menlo Park, CA 94025, USA

²⁵Université Paris Cité, CNRS/IN2P3, APC, 4 rue Elsa Morante, F-75013 Paris, France

²⁶Université Grenoble Alpes, CNRS/IN2P3, LPSC, 53 avenue des Martyrs, F-38026 Grenoble, France

²⁷Vera C. Rubin Observatory/NSF NOIRLab, Casilla 603, La Serena, Chile

²⁸University of Washington, Dept. of Physics, Box 351580, Seattle, WA 98195, USA

²⁹INAF Istituto di Astrofisica Spaziale e Fisica Cosmica di Palermo, Via Ugo la Malfa 153, 90146, Palermo, Italy

³⁰LSST Interdisciplinary Network for Collaboration and Computing, Tucson, USA

³¹Department of Astronomy and Planetary Science, Northern Arizona University, P.O. Box 6010, Flagstaff, AZ 86011, USA

³²Department of Astronomy and Astrophysics, University of Chicago, 5640 South Ellis Avenue, Chicago, IL 60637, USA

³³NSF NOIRLab, 950 N. Cherry Ave., Tucson, AZ 85719, USA

- 106 ³⁴ *Université Paris-Saclay, CNRS/IN2P3, IJCLab, 15 Rue Georges Clemenceau, F-91405 Orsay, France*
 107 ³⁵ *NCSA, University of Illinois at Urbana-Champaign, 1205 W. Clark St., Urbana, IL 61801, USA*
 108 ³⁶ *Smithsonian Astrophysical Observatory, 60 Garden St., Cambridge MA 02138, USA*
 109 ³⁷ *Caltech/IPAC, California Institute of Technology, MS 100-22, Pasadena, CA 91125-2200, USA*
 110 ³⁸ *Santa Cruz Institute for Particle Physics and Physics Department, University of California–Santa Cruz, 1156 High St., Santa Cruz,*
 111 *CA 95064, USA*
 112 ³⁹ *Department of Physics, Brown University, 182 Hope Street, Providence, RI 02912, USA*
 113 ⁴⁰ *D4D CONSULTING LTD., Suite 1 Second Floor, Everdene House, Deansleigh Road, Bournemouth, UK BH7 7DU*
 114 ⁴¹ *Aix Marseille Université, CNRS/IN2P3, CPPM, 163 avenue de Luminy, F-13288 Marseille, France*
 115 ⁴² *Université Clermont Auvergne, CNRS/IN2P3, LPCA, 4 Avenue Blaise Pascal, F-63000 Clermont-Ferrand, France*
 116 ⁴³ *C. Iñaki Goenaga, 5, 20600, Guipúzcoa, Spain*
 117 ⁴⁴ *INAF Osservatorio Astronomico di Trieste, Via Giovan Battista Tiepolo 11, 34143, Trieste, Italy*
 118 ⁴⁵ *Department of Physics, P.O. Box 64, 00014 University of Helsinki, Finland*
 119 ⁴⁶ *Asteroid Engineering Laboratory, Luleå University of Technology, Box 848, SE-981 28 Kiruna, Sweden*
 120 ⁴⁷ *CNRS/IN2P3, CC-IN2P3, 21 avenue Pierre de Coubertin, F-69627 Villeurbanne, France*
 121 ⁴⁸ *University of Arizona, Department of Astronomy and Steward Observatory, 933 N. Cherry Ave, Tucson, AZ 85721, USA*
 122 ⁴⁹ *Department of Astronomy, Yonsei University, 50 Yonsei-ro, Seoul 03722, Republic of Korea*
 123 ⁵⁰ *Physics Department, University of California, One Shields Avenue, Davis, CA 95616, USA*
 124 ⁵¹ *Space Sciences Lab, University of California, 7 Gauss Way, Berkeley, CA 94720-7450, USA*
 125 ⁵² *Lancaster University, Lancaster, UK*
 126 ⁵³ *Physics Department, University of California, 366 Physics North, MC 7300 Berkeley, CA 94720, USA*
 127 ⁵⁴ *Department of Physics, Duke University, Durham, NC 27708, USA*
 128 ⁵⁵ *Center for Cosmology and Astro-Particle Physics, The Ohio State University, Columbus, OH 43210, USA*
 129 ⁵⁶ *Physik-Institut, University of Zurich, Winterthurerstrasse 190, 8057 Zurich, Switzerland*
 130 ⁵⁷ *Department of Physics Columbia University, New York, NY 10027, USA*
 131 ⁵⁸ *EPCC, University of Edinburgh, 47 Potterrow, Edinburgh, EH8 9BT, UK*
 132 ⁵⁹ *Division of Physics, Mathematics and Astronomy, California Institute of Technology, Pasadena, CA 91125, USA*
 133 ⁶⁰ *soZen Inc., 105 Clearview Dr, Penfield, NY 14526*
 134 ⁶¹ *Astrophysics Research Cluster, School of Mathematical and Physical Sciences, University of Sheffield, Sheffield, S3 7RH, United*
 135 *Kingdom*
 136 ⁶² *Science and Technology Facilities Council, Rutherford Appleton Laboratory, Harwell, UK*
 137 ⁶³ *Department of Physics and Astronomy, Purdue University, 525 Northwestern Ave., West Lafayette, IN 47907, USA*
 138 ⁶⁴ *Departamento de Matemática y Física Aplicadas, Facultad de Ingeniería, Universidad Católica de la Santísima Concepción, Alonso de*
 139 *Rivera 2850, Concepción, Chile*
 140 ⁶⁵ *Australian Astronomical Optics, Macquarie University, North Ryde, NSW, Australia*
 141 ⁶⁶ *AURA, 950 N. Cherry Ave., Tucson, AZ 85719, USA*
 142 ⁶⁷ *Université Claude Bernard Lyon 1, CNRS/IN2P3, IP2I, 4 Rue Enrico Fermi, F-69622 Villeurbanne, France*
 143 ⁶⁸ *INAF Osservatorio di Astrofisica e Scienza dello Spazio Bologna, Via P. Gobetti 93/3, 40129, Bologna, Italy*
 144 ⁶⁹ *Department of Physics and Astronomy (DIFA), University of Bologna, Via P. Gobetti 93/2, 40129, Bologna, Italy*
 145 ⁷⁰ *Centro de Investigaciones Energéticas, Medioambientales y Tecnológicas, Av. Complutense 40, 28040 Madrid, Spain*
 146 ⁷¹ *J.Sick Codes Inc., Penetanguishene, Ontario, Canada*
 147 ⁷² *Science and Technology Facilities Council, UK Research and Innovation, Polaris House, North Star Avenue, Swindon, SN2 1SZ, UK*
 148 ⁷³ *ASTRON, Oude Hoogeveensedijk 4, 7991 PD, Dwingeloo, The Netherlands*
 149 ⁷⁴ *Department of Physics, Harvard University, 17 Oxford St., Cambridge MA 02138, USA*
 150 ⁷⁵ *National Astronomical Observatory of Japan, Chile Observatory, Los Abedules 3085, Vitacura, Santiago, Chile*
 151 ⁷⁶ *Department of Physics, University of Oxford, Denys Wilkinson Building, Keble Road, Oxford, OX1 3RH, UK*
 152 ⁷⁷ *LSST Discovery Alliance, 933 N. Cherry Ave., Tucson, AZ 85719, USA*
 153 ⁷⁸ *Department of Physics and Astronomy, University of Pittsburgh, 3941 O’Hara Street, Pittsburgh, PA 15260, USA*

(Dated: January 26, 2026)

ABSTRACT

We present Rubin Data Preview 1 (DP1), the first data from the NSF-DOE Vera C. Rubin Observatory, comprising raw and calibrated single-epoch images, coadds, difference images, detection catalogs, and ancillary data products. DP1 is based on 1792 optical/near-infrared exposures acquired over 48 distinct nights by the Rubin Commissioning Camera, LSSTComCam, on the Si-

159 monyi Survey Telescope at the Summit Facility on Cerro Pachón, Chile in late 2024. DP1 covers
 160 ~ 15 deg² distributed across seven roughly equal-sized non-contiguous fields, each independently ob-
 161 served in six broad photometric bands, *ugrizy*. The median FWHM of the point-spread function
 162 across all bands is approximately 1''14, with the sharpest images reaching about 0''58. The 5σ point
 163 source depths for coadded images in the deepest field, Extended Chandra Deep Field South, are:
 164 $u = 24.55, g = 26.18, r = 25.96, i = 25.71, z = 25.07, y = 23.1$. Other fields are no more than 2.2
 165 magnitudes shallower in any band, where they have nonzero coverage. DP1 contains approximately
 166 2.3 million distinct astrophysical objects, of which 1.6 million are extended in at least one band in
 167 coadds, and 431 solar system objects, of which 93 are new discoveries. DP1 is approximately 3.5 TB
 168 in size and is available to Rubin data rights holders via the Rubin Science Platform, a cloud-based
 169 environment for the analysis of petascale astronomical data. While small compared to future LSST
 170 releases, its high quality and diversity of data support a broad range of early science investigations
 171 ahead of full operations in late 2025.

172 *Keywords:* Rubin Observatory – LSST

173 1. INTRODUCTION

174 The National Science Foundation (NSF)–Department
 175 of Energy (DOE) Vera C. Rubin Observatory is a
 176 ground-based, wide-field optical/near-infrared facility
 177 located on Cerro Pachón in northern Chile. Named in
 178 honor of Vera C. Rubin, a pioneering astronomer whose
 179 groundbreaking work in the 20th century provided the
 180 first convincing evidence for the existence of dark mat-
 181 ter (V. C. Rubin & W. K. Ford 1970; V. C. Rubin et al.
 182 1980), the observatory’s prime mission is to carry out the
 183 Legacy Survey of Space and Time (formerly Large Syn-
 184 optic Survey Telescope) (LSST) (Ž. Ivezić et al. 2019a).
 185 This 10-year survey is designed to obtain rapid-cadence,
 186 multi-band imaging of the entire visible southern sky
 187 approximately every 3–4 nights. Over its main 18,000
 188 deg² footprint, the LSST is expected to reach a depth
 189 of ~ 27 magnitude in the r-band, with ~ 800 visits per
 190 pointing in all filters (F. B. Bianco et al. 2022).

191 The Rubin Observatory system consists of four main
 192 components: the Simonyi Survey Telescope, featuring
 193 an 8.4 m diameter (6.5 m effective aperture) primary
 194 mirror that delivers a wide field of view; a 3.2-gigapixel
 195 camera, capable of imaging 9.6 square degrees per ex-
 196 posure⁷⁹ with seeing-limited quality in six broadband
 197 filters, *ugrizy* (320–1050 nm); an automated Data Man-
 198 agement System that processes and archives tens of ter-
 199 abytes of data per night, generating science-ready data
 200 products within minutes for a global community of sci-
 201 entists; and an Education and Public Outreach (EPO)

202 program that provides real-time data access, interactive
 203 tools, and educational content to engage the public. The
 204 integrated system’s étendue⁸⁰ of 319 m² deg², is over an
 205 order of magnitude larger than that of any previous op-
 206 tical observatory, enabling a fast, large-scale survey with
 207 exceptional depth in a fraction of the time compared to
 208 other observatories.

209 The observatory’s design is driven by four key science
 210 themes: probing dark energy and dark matter; taking
 211 an inventory of the solar system; exploring the tran-
 212 sient and variable optical sky; and mapping the Milky
 213 Way (Ž. Ivezić et al. 2019a). These themes inform the
 214 optimization of a range of system parameters, includ-
 215 ing image quality, photometric and astrometric accu-
 216 racy, the depth of a single visit and the co-added survey
 217 depth, the filter complement, the total number of visits
 218 per pointing as well as the distribution of visits on the
 219 sky, and total sky coverage. Additionally, they inform
 220 the design of the data processing and access systems.
 221 By optimizing the system parameters to support a wide
 222 range of scientific goals, we maximize the observatory’s
 223 scientific output across all areas, making Rubin a pow-
 224 erful discovery machine capable of addressing a broad
 225 range of astrophysical questions.

226 Throughout the duration of the LSST, Rubin Obser-
 227 vatory will issue a series of Data Releases, each repre-
 228 senting a complete reprocessing of all LSST data col-
 229 lected up to that point. Prior to the start of the LSST
 230 survey, commissioning activities will generate a signifi-
 231 cant volume of science-grade data. To make this early
 232 data available to the community, the Rubin Early Sci-
 233 ence Program (L. P. Guy et al. 2026) was established.

* Author is deceased

⁷⁹ We define an “exposure” as the process of exposing all detectors in the focal plane. It is synonymous with the term “visit” in Data Preview 1 (DP1). By contrast, an “image” is the output of a single detector following an exposure.

⁸⁰ The product of the primary mirror area and the angular area of its field of view for a given set of observing conditions.

One key component of this program is a series of Data Previews; early versions of the LSST Data Releases. These previews include preliminary data products derived from both simulated and commissioning data, which, together with early versions of the data access services, are intended to support high-impact early science, facilitate community readiness, and inform the development of Rubin’s operational capabilities ahead of the start of full survey operations. All data and services provided through the Rubin Early Science Program are offered on a shared-risk basis⁸¹.

This paper describes Rubin’s second of three planned Data Previews: DP1 (NSF-DOE Vera C. Rubin Observatory 2025a). The first, Data Preview 0 (DP0), contained data products produced from the processing of simulated LSST-like data sets. These were released together with a very early version of the Rubin Science Platform (M. Jurić et al. 2019), which provided the data access services. DP0 was released in multiple phases; DP0.1, DP0.2, and DP0.3, each building upon the previous and incorporating new data and functionalities. DP0.1 and DP0.2 uses data from the cosmoDC2 simulations (LSST Dark Energy Science Collaboration (LSST DESC) et al. 2021) prepared by the Dark Energy Science Collaboration (DESC), whereas DP0.3 is based on simulated datasets from the Solar System Science Collaboration (SSSC). Online documentation for DP0 is available at <https://dp0.lsst.io>.

DP1 contains data products derived from the reprocessing of science-grade exposures acquired by the Rubin Commissioning Camera (LSSTComCam), in late 2024. The third and final Data Preview, Data Preview 2 (DP2), is planned to be based on a reprocessing of all science-grade data taken with the Rubin’s LSST Science Camera (LSSTCam) during commissioning.

All Rubin Data Releases and Previews are subject to a two-year proprietary period, with immediate access granted exclusively to LSST data rights holders (R. Blum & the Rubin Operations Team 2020). Data rights holders⁸²See <https://www.lsst.org/scientists/international-drh-list> are individuals or institutions with formal authorization to access proprietary data collected by the Vera C. Rubin Observatory. After the two-year proprietary period, DP1 will be made public. However, even once the data become public, access for non-data rights holders will not be provided through Rubin Data

Access Centers in the US and Chile (R. Blum & the Rubin Operations Team 2020). Alternative access mechanisms are still under discussion and have not yet been finalized.

In this paper, we describe the contents and validation of Rubin DP1, the first Data Preview to deliver data derived from observations conducted by the Vera C. Rubin Observatory, as well as the data-access mechanisms and community-support services that accompany it. DP1 is based on the reprocessing of 1792 science-grade exposures acquired during the first on-sky commissioning campaign, conducted over 48 nights between 2024-10-24 and 2024-12-11. It covers a total area of approximately ~ 15 deg² distributed across seven distinct non-contiguous fields. The data products include raw and calibrated single-epoch images, coadded images, difference images, detection catalogs, and other derived data products. DP1 is about 3.5 TB in size and contains around 2.3 million distinct astronomical objects, detected in 2644 coadded images. Full DP1 release documentation is available at <https://dp1.lsst.io>. Despite Rubin Observatory still being in commissioning and not yet complete at the time the observations were acquired, Rubin DP1 provides an important first look at the data, showcasing its characteristics and capabilities.

The structure of this paper is as follows. In section 2 we describe the observatory system and overall construction and commissioning status at the time of data acquisition, the seven fields included in DP1, and the observing strategy used. Section 3 summarizes the contents of DP1 and the data products contained in the release. The data processing pipelines are described in section 4, followed by a description of the data validation and performance assessment in section 5. Section 6 describes the Rubin Science Platform (RSP), a cloud-based data science infrastructure that provides tools and services to Rubin data rights holders to access, visualize and analyze peta-scale data generated by the LSST. Section 7 presents the Rubin Observatory’s model for community support, which emphasizes self-help via documentation and tutorials, and employs an open platform for issue reporting that enables crowd-sourced solutions. Finally, a summary of the DP1 release and information on expected future releases of data is given in section 8. The appendix contains a useful glossary of terms used throughout this paper.

All magnitudes quoted are in the AB system (J. B. Oke & J. E. Gunn 1983), unless otherwise specified.

2. ON-SKY COMMISSIONING CAMPAIGN

The first Rubin on-sky commissioning campaign was conducted using the LSSTComCam. The campaign’s

⁸¹ Shared risk means early access with caveats: the community benefits from getting a head start on science, preparing analyses, and providing feedback, while also accepting that the system may not work as well as it will during full operations.

⁸² (

primary objective was to optically align the Simonyi Survey Telescope and verify its ability to deliver acceptable image quality using *LSSTComCam*. In addition, the campaign provided valuable operations experience to facilitate commissioning the full *LSSTCam* (T. Lange et al. 2024; A. Roodman et al. 2024). We note that commissioning *LSSTComCam* was not an objective of the campaign. Instead, *LSSTComCam* was used as a tool to support broader observatory commissioning, including early testing of the *Active Optics System* (AOS) and the LSST Science Pipelines. As a result, many artifacts present in the data are specific to *LSSTComCam* and will be addressed only if they persist with *LSSTCam*. Accordingly, the image quality achieved during this campaign, and in the *DP1* data, may not reflect the performance ultimately expected from *LSSTCam*.

Approximately 16,000 exposures⁸³ were collected during this campaign, the majority in support of AOS commissioning, system-level verification, and end-to-end testing of the telescope’s hardware and software. This included over 10000 exposures for AOS commissioning, more than 2000 bias and dark calibration frames, and over 2000 exposures dedicated to commissioning the LSST Science Pipelines. For *DP1*, we have selected a subset of 1792 science-grade exposures from this campaign that are most useful for the community to begin preparing for early science.

At the time of the campaign, the observatory was still under construction, with several key components, such as dome thermal control, full mirror control, and the final AOS configuration either incomplete or still undergoing commissioning. As a result, image quality varied widely throughout the campaign and exhibited a broader distribution than is expected with *LSSTCam*. Despite these limitations, the campaign successfully demonstrated system integration and established a functional observatory.

2.1. *Simonyi Survey Telescope*

The Simonyi Survey Telescope (B. Stalder et al. 2024) features a unique three-mirror design, including an 8.4-meter *Primary Mirror Tertiary Mirror* (M1M3) fabricated from a single substrate and a 3.5-meter *Secondary Mirror* (M2). This compact configuration supports a wide 3.5-degree field of view while enabling exceptional stability, allowing the telescope to slew and settle in under five seconds. To achieve the scientific goals of the

10-year *LSST*, the Observatory must maintain high image quality across its wide field of view (Ž. Ivezić et al. 2019b). This is accomplished through the AOS (B. Xin et al. 2015; G. Megias Homar et al. 2024), which corrects, between successive exposures, wavefront distortions caused by optical misalignments and mirror surface deformations, primarily due to the effect of gravitational and thermal loads.

The AOS, which comprises an open-loop component and a closed-loop component, optimizes image quality by aligning the camera and M2 relative to M1M3, as well as adjusting the shapes of all three mirrors to nanometer precision. The AOS open-loop component corrects for predictable distortions and misalignments, while the closed-loop component addresses unpredictable or slowly varying aberrations using feedback from the corner wavefront sensors. The closed-loop wavefront sensing technique is curvature wavefront sensing, which infers wavefront errors in the optical system by analyzing extra- and intra-focal star images (S. Thomas et al. 2023). Since *LSSTComCam* lacks dedicated wavefront sensors, wavefront errors were instead estimated by defocusing the telescope ± 1.5 mm on either side of focus and applying the curvature wavefront sensing pipeline to the resulting images. Each night began with an initial alignment correction using a laser tracker to position the system within the capture range of the closed-loop algorithm (G. Megias Homar et al. 2024). Once this coarse alignment was complete, the AOS refined the optical alignment and applied mirror surfaces corrections to optimize the image quality across the *LSSTComCam* field of view.

During *LSST Science Pipelines* commissioning (§2.4), observations were conducted using the AOS in open-loop mode only, without closed-loop corrections between exposures. Closed-loop operation, which requires additional intra- and extra-focal images with *LSSTComCam*, was not compatible with the continuous data acquisition needed by the pipelines. The image quality for these data was monitored by measuring the *Point Spread Function* (PSF) *Full Width at Half-Maximum* (FWHM), and closed-loop sequences were periodically run when image quality degradation was observed.

2.2. *The LSST Commissioning Camera*

LSSTComCam (B. Stalder et al. 2022, 2020; J. Howard et al. 2018; SLAC National Accelerator Laboratory & NSF-DOE Vera C. Rubin Observatory 2024) is a 144-megapixel version of the 3.2-gigapixel *LSSTCam*. It covers approximately 5% of the *LSSTCam* focal plane area, with a field of view of ~ 0.5 deg² ($40' \times 40'$), compared to *LSSTCam*’s 9.6 deg². It was developed to val-

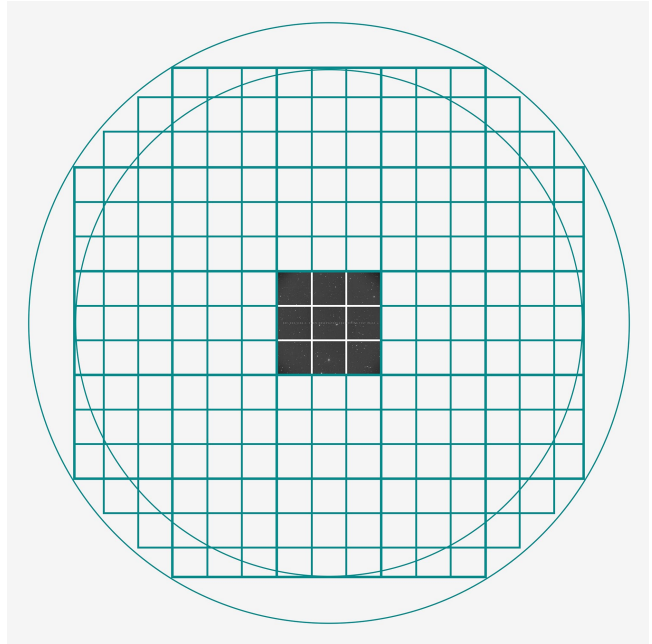
⁸³ We define an exposure as the process of exposing all *LSSTComCam* detectors. It is synonymous with visit in *DP1*. By contrast, an image is the output of a single *LSSTComCam* detector following an exposure.

428 idate camera interfaces with other observatory compo-
 429 nents and evaluate overall system performance prior to
 430 the start of **LSSTCam** commissioning. Although **LSST-**
 431 **ComCam** has a smaller imaging area, it shares the same
 432 plate scale of $0''.2$ per pixel and is housed in a support
 433 structure that replicates the mass, center of gravity, and
 434 physical dimensions of **LSSTCam**. All mechanical and
 435 utility interfaces to the telescope are implemented iden-
 436 tically, enabling full end-to-end testing of observatory
 437 systems, including readout electronics, image acquisi-
 438 tion, and data pipelines. Although the **LSSTComCam**
 439 cryostat employs a different cooling system (Cryotels) to
 440 that of **LSSTCam**, it included a refrigeration pathfinder
 441 to validate the cryogenic system intended for **LSSTCam**.

442 The **LSSTCam** focal plane comprises 25 modular rafts
 443 arranged in a 5×5 grid, of which 21 are science rafts de-
 444 dicated to imaging and 4 are corner rafts used for guid-
 445 ing and wavefront sensing. **LSSTCam** employs CCD
 446 sensors from two vendors: Imaging Technology Labora-
 447 tory, University of Arizona (UA) (ITL) and Teledyne
 448 (E2V). In contrast, **LSSTComCam** contains only a sin-
 449 gle science raft equipped exclusively with ITL sensors.
 450 Figure 1 presents a schematic of the **LSSTCam** focal
 451 plane, with the **LSSTComCam** raft positioned at the
 452 center, corresponding to the **LSSTCam** central science
 453 raft location. The perspective is from above, looking
 454 down through the **LSSTComCam** lenses onto the focal
 455 plane.

456 Each science raft is a self-contained unit compris-
 457 ing nine $4K \times 4K$ Charge-Coupled Device (CCD) (G. E.
 458 Smith 2010) sensors arranged in a 3×3 mosaic, complete
 459 with integrated readout electronics and cooling systems.
 460 Each sensor is subdivided into 16 segments arranged in
 461 a 2×8 layout, with each segment consisting of 512×2048
 462 pixels and read out in parallel using individual ampli-
 463 fiers. This design is identical across all science rafts.
 464 To maintain uniform performance and calibration, each
 465 raft is populated exclusively with sensors from a single
 466 vendor.

467 **LSSTComCam** consists of a single science raft, desig-
 468 nated Raft 22 (R22), equipped solely with ITL sensors.
 469 These sensors were selected from the best-performing re-
 470 maining ITL devices after the **LSSTCam** rafts were fully
 471 populated. Some exhibit known issues such as high read-
 472 out noise (e.g., Detector 8) and elevated Charge Transfer
 473 Inefficiency (CTI) (e.g., Detector 5). Consequently, cer-
 474 tain image artifacts present in the DP1 dataset may be
 475 specific to **LSSTComCam**. Figure 2 shows the **LSST-**
 476 **ComCam** R22 focal plane layout and the placement and
 477 numbering scheme of sensors (S) and amplifiers (C).
 478 This configuration is identical across all science rafts
 479 in **LSSTCam**. The **LSSTCam** and **LSSTComCam** focal



481 **Figure 1.** **LSSTComCam** focal plane layout illustrating the
 482 placement and numbering scheme of sensors (S) and ampli-
 483 fiers (C). The view is looking down from above the focal plane
 484 through the **LSSTComCam** lenses. Each sensor contains 16
 485 amplifiers, and a group of nine sensors comprises one raft.
 486 **LSSTComCam** is Raft 22 (R22). The detector number for
 487 each sensor is shown in parentheses.

488 planes are described in detail in A. A. Plazas Malagón
 489 et al. (2025).

490 2.2.1. Filter Complement

491 **LSSTComCam** supports imaging with six broadband
 492 filters *ugrizy* spanning 320–1050 nm, identical in de-
 493 sign to **LSSTCam**. However, its filter exchanger can
 494 hold only three filters at a time, compared to five with
 495 **LSSTCam**. The full-system throughput of the six **LSST-**
 496 **ComCam** filters, which encompasses contributions from
 497 a standard atmosphere at airmass 1.2, telescope optics,
 498 camera surfaces, and the mean ITL detector quantum
 499 efficiency is shown in Figure 3. The corresponding trans-
 500 mission curves are provided as a DP1 data product, see
 501 §3.6.1

502 2.2.2. Timing Calibration

503 The absolute time accuracy of data taken with **LSST-**
 504 **ComCam** relies on the Network Time Protocol (NTP)
 505 for clock synchronization, which should be accurate
 506 to approximately 1 millisecond. In order to evaluate
 the absolute timing accuracy of the entire system we
 observed the geosynchronous satellite EUTELSAT 117
 West B with a set of 10 usable 10-second exposures over
 two nights. EUTELSAT 117 West B is part the Global
 Positioning System (GPS) system and serves as one of

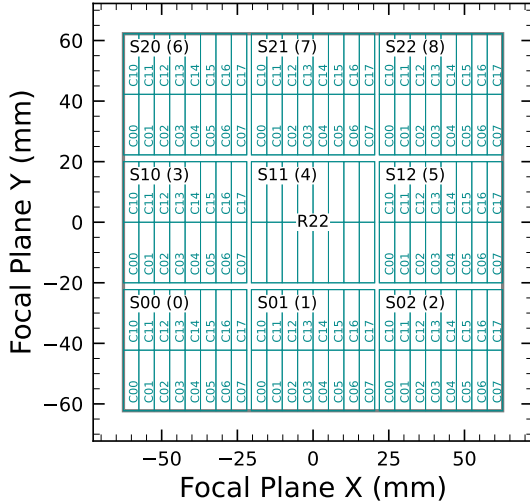


Figure 2. LSSTComCam focal plane layout, showing Raft 22 (R22) and the placement and numbering scheme of sensors (S) and amplifiers (C). The view is from above, looking through the LSSTComCam lenses onto the focal plane. Each sensor contains 16 amplifiers, and the raft is composed of a 3×3 array of sensors. The detector number for each sensor is indicated in parentheses.

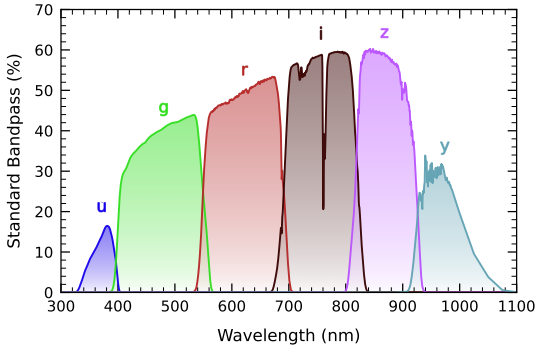


Figure 3. LSSTComCam standard bandpasses, illustrating full system throughput. The bandpasses include a standard atmosphere at airmass 1.2, telescope optics, camera surfaces, and mean ITL detector quantum efficiency. The corresponding transmission curves are provided as a DP1 data product.

the Wide Area Augmentation System (WAAS) satellites operated for the U.S. Federal Aviation Administration (FAA) and used to broadcast GPS corrections to air traffic.

As these satellites are part of the GPS system, their positions are tracked very precisely and the record of their locations is published after the fact and can be downloaded. Following the technique previously employed by other surveys, (J. L. Tonry et al. 2018), we observed the satellite while tracking the sky and then downloaded the data-files with its precise locations from

the National Satellite Test Bed web site⁸⁴. By comparing the measured and predicted locations of the start of the satellite track on the sky, we determined that (relative to the start of integration-time recorded in the Flexible Image Transport System (FITS) headers) our time was accurate to 53.6 ± 11.0 milliseconds.

This work continues to be an area of ongoing study, with the exact timing of when the shutter open command is issued, and the complete profile of the shutter movement not yet determined. However the open command is on average near 29 milliseconds later. Incorporating the delays into the fit reduces the offset to 24.8 ± 11.0 milliseconds.

The full shutter takes approximately 396 milliseconds to completely open. As the LSSTComCam sensors are centered in the aperture, the center of the focal plane should be exposed about half-way through the shutter open procedure, 198 milliseconds after the open command. There are uncertainties on the full motion profile, and the blade direction motions are currently not known, but the fraction of the shutter aperture subtended by the focal plane is 52%. This implies that that the shutter will pass any pixel between 198 ± 103 milliseconds. Subtracting this from the fitted delay of 24.8 milliseconds and adding the fitted error of 11.0 milliseconds in quadrature, results in a current conservative estimate of the delay of -173.2 ± 104.1 milliseconds, consistent with and smaller than the constraints on the timing offset determined using astrometric residuals from known asteroid associations presented in §5.10.2.

2.3. Flat Field System

During the on-sky campaign, key components of the Rubin calibration system (P. Ingraham et al. 2022), including the flat field screen, had not yet been installed. As a result, flat fielding for DP1 relied entirely on twilight flats. While twilight flats pose challenges such as non-uniform illumination and star print-through, they were the only available option during LSSTComCam commissioning and for DP1 processing. To mitigate these limitations, dithered, tracked exposures were taken over a broad range of azimuth and rotator angles to construct combined flat calibration frames. Exposure times were dynamically adjusted to reach target signal levels of between 10,000 and 20,000 electrons. Future campaigns with LSSTComCam will benefit from more stable and uniform flat fielding using the Rubin flat field system, described in P. Fagrelus & E. S. Rykoff (2025).

⁸⁴ <https://www.nstb.tc.faa.gov/nstbarchive.html>

2.4. LSST Science Pipelines Commissioning

Commissioning of the LSST Science Pipelines, (Rubin Observatory Science Pipelines Developers 2025), began once the telescope was able to routinely deliver sub-arcsecond image quality. The goals included testing the internal astrometric and photometric calibration across a range of observing conditions, validating the difference image analysis and Prompt Processing (K.-T. Lim 2023) framework, and accumulating over 200 visits per band to evaluate deep coadded images with integrated exposure times roughly equivalent to those of the planned LSST Wide-Fast-Deep (WFD) 10-year depth. To support these goals, seven target fields were selected that span a range of stellar densities, overlap with external reference datasets, and collectively span the full breadth of the four primary LSST science themes. These seven fields form the basis of the DP1 dataset. Figure 4 shows the locations of these seven fields on the sky, overlaid on the LSST baseline survey footprint (R. L. Jones et al. 2021; P. Yoachim 2022; Rubin’s Survey Cadence Optimization Committee et al. 2022, 2023, 2025), along with sky coverage of both the LSSTCam and LSSTComCam focal planes. Each of the seven target fields was observed repeatedly in multiple bands over many nights. A typical observing epoch on a given target field consisted of 5-20 visits in each of the three loaded filters. Only images taken as 1x30 second exposures have been included in DP1. All images were acquired using the Rubin Feature-Based Scheduler (FBS), version 3.0 (E. Naghib et al. 2019; P. Yoachim et al. 2024). Table 1 lists the seven DP1 fields and their pointing centers, and provides a summary of the band coverage in each.

Figure 5 shows the temporal sampling of observations by filter and by night. The figure indicates the dates on which each field was observed in a given band but does not convey the total number of observations obtained per filter on any individual night. Gaps in coverage across some bands arise from the fact that LSST-ComCam can only accommodate three filters at a time (see §2.2). As the campaign progressed, the temporal sampling became denser across all fields, reflecting improved efficiency and increased time allocated for science observations. The Extended Chandra Deep Field-South Survey (ECDFS) field received the most consistent and densest temporal sampling. It is important to note that the time sampling in the DP1 dataset differs significantly from what will be seen in the final LSST data. All fields except for the low ecliptic latitude field, Rubin_SV_38_7, used a small random dithering pattern. The random translational dithers of the telescope boresight were applied for each visit, with offsets of up to 0.2 degrees around the pointing center (Table 1). The

rotational dithers of the camera rotator were typically approximately 1 degree per visit, with larger random offsets at each filter change, which worked to keep operational efficiency high. The Rubin_SV_38_7 field used a different dither pattern to optimize coverage of Solar System Objects and test Solar System Object linking across multiple nights. These observations used a 2x2 grid of LSSTComCam pointings to cover an area of about 1.3 degreex1.3 degrees. The visits cycled between the grid’s four pointing centers, each separated by 0.65 degrees, and used small random translational dithers to fill chip gaps with the goal of acquiring 3-4 visits per pointing center per band in each observing epoch. The ra/dec vale giving in table 1 for this field is approximately the center of the 4 filed.

Figure 6 shows sky coverage maps showing the distribution of visits in each of the seven DP1 fields, color coded by band. The images clearly show the focal plane chip gaps and dithering pattern. DP1 Only the detectors for which single frame processing succeeded are included in the plots, which explains why the central region of 47_Tuc looks thinner than the other fields (see §5.11). Table 2 reports the 5 σ point source depths for coadded images per field and per band, where coverage in a band is non-zero, together with the expected 10-year LSST depths derived from the baseline simulated survey (F. B. Bianco et al. 2022).

2.5. Delivered Image Quality

The delivered image quality is influenced by contributions from both the observing system (i.e., dome, telescope and camera) and the atmosphere. During the campaign, the Rubin Differential Image Motion Monitor (DIMM) was not operational, so atmospheric seeing was estimated using live data from the Southern Astrophysical Research Telescope (SOAR) Ring-Image Next Generation Scintillation Sensor (RINGSS) seeing monitor, also located on Cerro Pachón. Although accelerometers mounted on the mirror cell and top-end assembly were available to track dynamic optics effects, such as mirror oscillations that can degrade optical alignment, this data was not used during the campaign. Mount encoder data were used to measure the mount jitter in every image, with a measured median contribution of 0.004 arcseconds to image degradation. As the pointing model was not fine tuned, tracking errors could range from 0.2 to 0.4 arcseconds per image, depending on RA and Dec. Dome and mirror-induced seeing were not measured during the campaign.

The DP1 median delivered image quality, quantified as the PSF at FWHM across all filters and target fields, is 1".14. The best images achieve a PSF FWHM of ap-

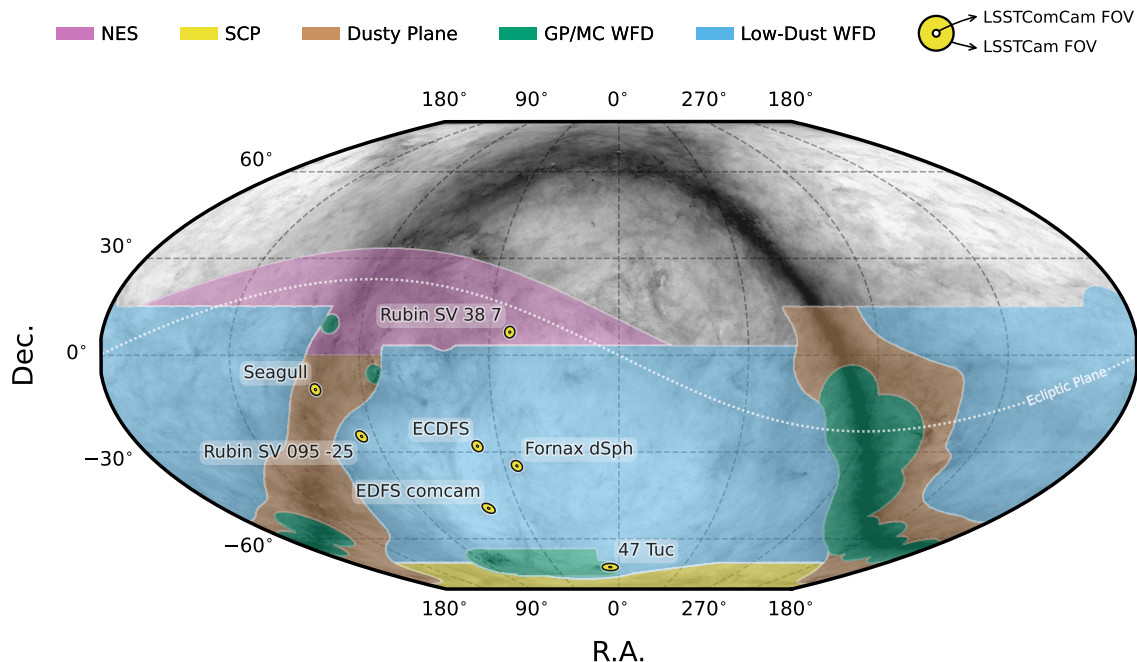


Figure 4. Locations of the seven DP1 fields overlaid on the LSST baseline survey footprint. NES: North Ecliptic Spur, SCP: South Celestial Pole, Low-Dust WFD: regions away from the Galactic Plane (GP) observed with a WFD cadence, GP/MC WFD: Galactic Plane and Magellanic Clouds regions observed with a WFD cadence. The field of view covered by the LSSTCam and LSSTComCam focal planes is shown as concentric yellow circles about the pointing center of each field.

Table 1. DP1 fields and pointing centers with the number of exposures in each band per field. ICRS coordinates are in units of decimal degrees, and are specified as J2000.

Field Code	Field Name	RA	DEC	Band						Total
				deg	deg	<i>u</i>	<i>g</i>	<i>r</i>	<i>i</i>	
47_Tuc	47 Tucanae Globular Cluster	6.128	-72.090	6	10	32	19	0	5	72
ECDFS	Extended Chandra Deep Field South	53.160	-28.100	43	230	237	162	153	30	855
EDFS_comcam	Rubin SV Euclid Deep Field South	59.150	-48.730	20	61	87	42	42	20	272
Fornax_dSph	Fornax Dwarf Spheroidal Galaxy	40.080	-34.450	0	5	25	12	0	0	42
Rubin_SV_095_-25	Rubin SV Low Galactic Latitude Field	95.040	-25.000	33	82	84	23	60	10	292
Rubin_SV_38_7	Rubin SV Low Ecliptic Latitude Field	37.980	7.015	0	44	40	55	20	0	159
Seagull	Seagull Nebula	106.300	-10.510	10	37	43	0	10	0	100
Total				112	469	548	313	285	65	1792

671 proximately $0''.58$. Both the per-sensor PSF FWHM and
 672 the overall median vary depending on the filter and the
 673 specific target field. The median delivered image quality
 674 per band and target field is provided in Table 3. Fig-
 675 ure 7 shows the distribution of PSF FWHM (in arcsec)
 676 over all 16071 individual sensors images. Ongoing efforts
 678 aim to quantify all sources of image degradation, includ-
 679 ing contributions from the camera system; static and
 680 dynamic optical components; telescope mount motion;

681 observatory-induced seeing from the dome and primary
 682 mirror; and atmospheric conditions. For the LSST, the
 683 design specification for the median delivered image qual-
 684 ity, referenced to the zenith and 550 nm, is $0''.7$. This
 685 value corresponds to the measured median atmospheric
 686 seeing at the Cerro Pachón site and a system contribu-
 687 tion to delivered image quality of $0''.35$ added in quadra-
 688 ture.

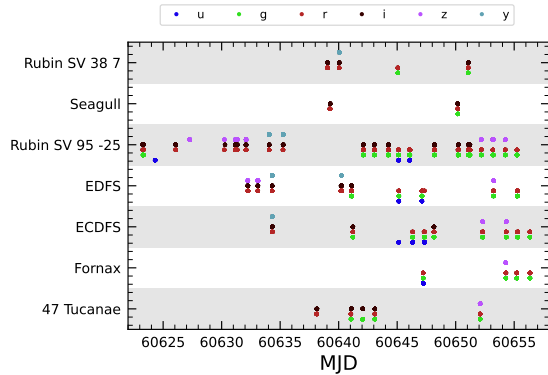


Figure 5. Temporal distribution of DP1 observations, grouped by field as a function of Modified Julian Date (MJD) and color-coded by filter. Each point indicates that a given field was observed at least once in the corresponding filter on that date.

Table 2. DP1 median 5σ coadded point-source detection limits per field and band, compared with the expected 10-year LSST values derived from the baseline simulated survey (F. B. Bianco et al. 2022).

Field Code	Band					
	<i>u</i>	<i>g</i>	<i>r</i>	<i>i</i>	<i>z</i>	<i>y</i>
47_Tuc	-	24.03	24.24	23.90	-	21.79
ECDFS	24.55	26.18	25.96	25.71	25.07	23.10
EDFS_comcam	23.42	25.77	25.72	25.17	24.47	23.14
Fornax_dSph	-	24.53	25.07	24.64	-	-
Rubin_SV_095_-25	24.29	25.46	24.95	24.86	24.32	22.68
Rubin_SV_38_7	-	25.46	25.15	24.86	23.52	-
Seagull	23.51	24.72	24.19	-	23.30	-
LSST 10-year	25.73	26.86	26.88	26.34	25.63	24.87

Table 3. DP1 Median image quality per field and per band quantified as the PSF at FWHM in arcseconds.

Field Code	Band						All
	<i>u</i>	<i>g</i>	<i>r</i>	<i>i</i>	<i>z</i>	<i>y</i>	
47_Tuc	-	1.27	1.25	1.11	-	1.33	1.22
ECDFS	1.40	1.14	1.08	1.00	1.00	1.07	1.08
EDFS_comcam	1.88	1.25	1.20	1.10	1.18	0.99	1.19
Fornax_dSph	-	1.16	0.82	0.93	-	-	0.85
Rubin_SV_095_-25	1.40	1.25	1.14	0.97	1.17	0.82	1.19
Rubin_SV_38_7	-	1.13	1.13	1.10	1.22	-	1.13
Seagull	1.50	1.34	1.19	-	1.19	-	1.25
All	1.48	1.17	1.12	1.03	1.11	1.01	1.13

vidual CCD images taken across 1792 exposures in the seven LSSTComCam commissioning fields (§2.4). To aid legibility, we have separated the descriptions of the data products from the description of the data release processing pipeline, a summary of which is provided in §4. Similarly, because most of the data products described here can be accessed via either the International Virtual Observatory Alliance (IVOA) Services (§6.2.1) or the Data Butler (§6.2.2), we describe them in a manner that is agnostic to the means of access.

The data products that comprise DP1 provide an early preview of future LSST data releases and are strongly dependent on the type and quality of the data that was collected during the LSSTComCam on-sky campaign (§2.4). Consequently not all anticipated LSST data products, as described in the Data Product Definition Document (DPDD) (M. Jurić et al. 2023), were produced for the DP1 dataset.

Rubin Observatory has adopted the convention by which single-epoch detections are referred to as Sources. By contrast, the astrophysical object associated with a given detection is referred to as an Object⁸⁶. As such, a given Object will likely have multiple associated Sources, since it will be observed in multiple epochs.

At the highest level, the DP1 data products fall into one of five types:

- **Images**, including single-epoch images, deep and template coadded images, and difference images (§3.1);

⁸⁶ We caution that this nomenclature is not universal; for example, some surveys call “detections” what we call “sources”, and use the term “sources” for what we call “objects”.

⁸⁵ The DP1 median delivered image quality across all bands is $1''.14$, as measured by the PSF FWHM.

3. OVERVIEW OF THE CONTENTS OF RUBIN DP1

Here we describe Rubin DP1 data products and provide summary statistics for each, but we also refer the reader to the DOI-registered DP1 release documentation available at <https://dp1.lsst.io> and the catalog schemas available at <https://sdm-schemas.lsst.io>.⁸⁵ The DP1 science data products are derived from the 15972 indi-

⁸⁵ Searchable catalog schemas are also available to Data Rights Holders via the Rubin Science Platform at <https://data.lsst.cloud>.

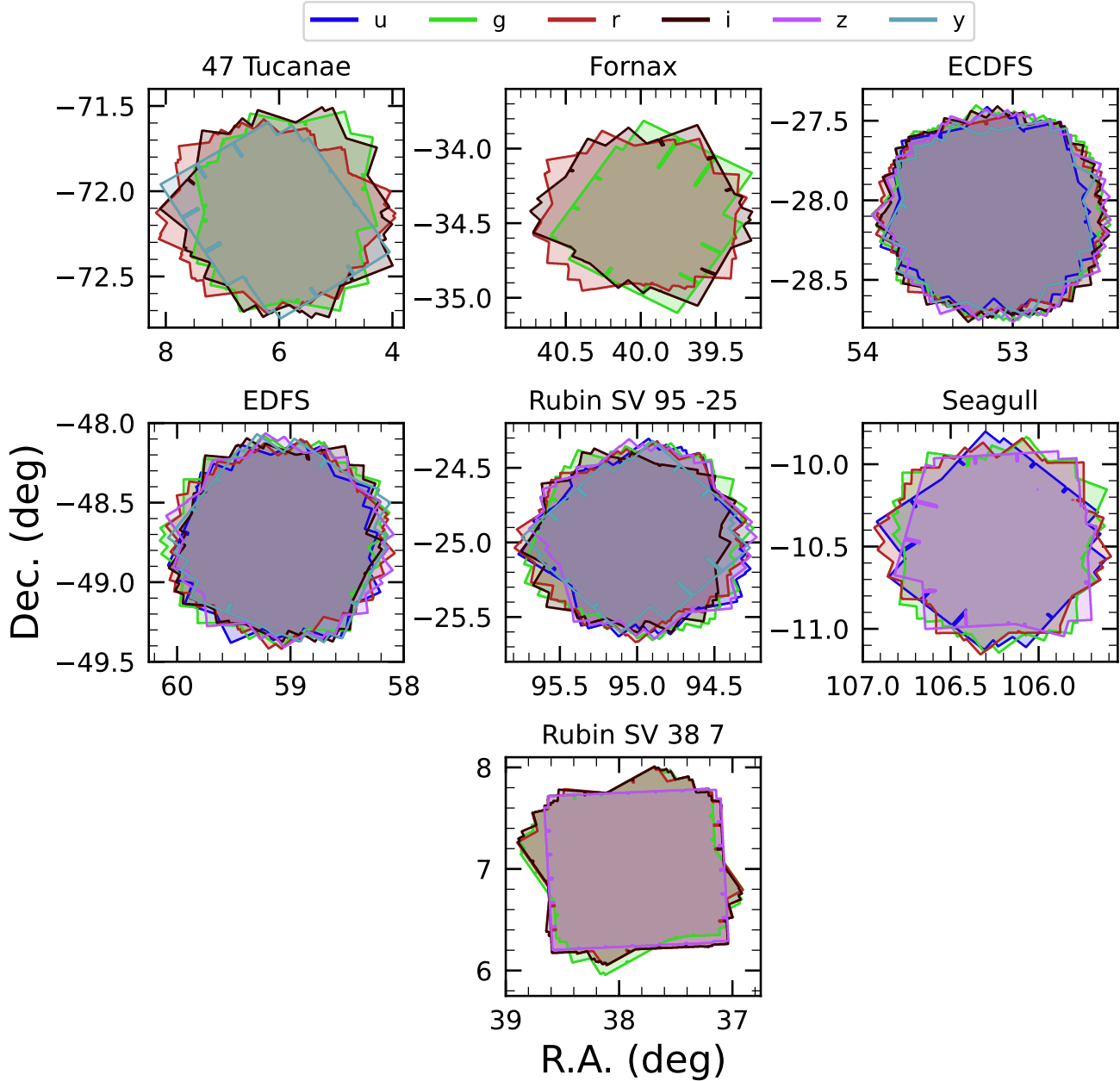


Figure 6. Sky coverage maps showing the distribution of visits in each field, color coded by band. The images clearly show the focal plane chip gaps and dithering pattern. Only the detectors for which single frame processing succeeded are included in the plots, which explains why the central region of 47_Tuc looks thinner than the other fields.

- 728 • **Catalogs** of astrophysical Sources and Objects detected and measured in the aforementioned images. We also provide the astrometric and photometric reference catalog generated from external sources that was used during processing to generate the DP1 data products (§3.2);

729

730

731

732

733

736 for example, zoomable multi-band images and coverage maps (§3.3);

737

738 • **Ancillary data products**, including, for example, the parameters used to configure the data processing pipelines, log and processing performance files, and calibration data products (§3.6);

739

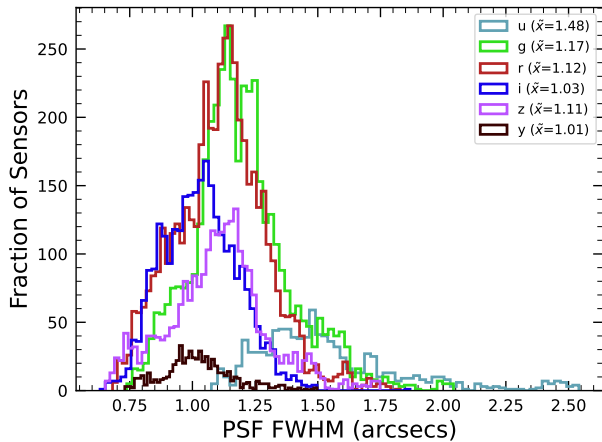
740

741
- 734 • **Maps**, which provide non-science-level visualizations of the data within the release. They include,

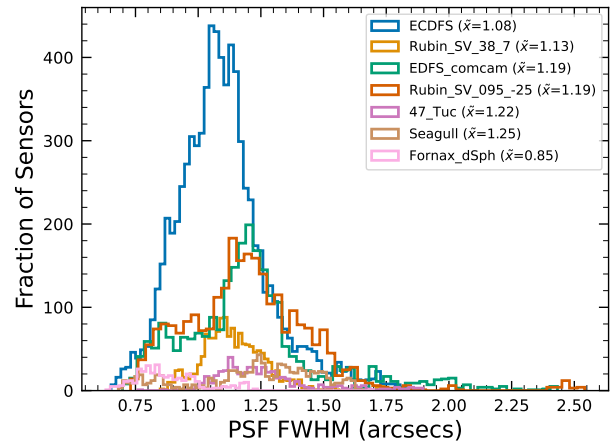
735

742

743 • **Metadata** in the form of tables containing information about each visit and processed image, such



(a) PSF FWHM (arcsecs) per passband across all DP1 target fields.



(b) PSF FWHM (arcsecs) per DP1 target field across all passbands

Figure 7. Histograms showing the distribution of delivered image quality for all 16071 single-epoch individual sensors in the DP1 dataset per passband (a) and per field (b). The median values are given in the legend.

744 as pointing, exposure time, and a range of image
745 quality summary statistics (§3.5).

746 While images and catalogs are expected to be the pri-
747 mary data products for scientific research, we also rec-
748 ognize the value of providing access to other data types
749 to support investigations and ensure transparency.

750 To facilitate processing, Rubin DP1 uses a single
751 skymap⁸⁷ that covers the entire sky area encompass-
752 ing the seven DP1 fields. The DP1 skymap divides the
753 entire celestial sphere into 18938 tracts, each covering
754 approximately 2.8 deg². The tracts are arranged in rings
755 of declination, ordered from south to north, then with
756 increasing right ascension within a ring. Each tract is
757 further subdivided into 10 × 10 equally-sized patches.
758 Both tracts and patches overlap with their neighboring
759 regions. The amount of overlap between tracts changes
760 with declination, with tracts nearest the poles having
761 the greatest degree of overlap; the minimum overlap be-
762 tween tracts is 1′.0. By contrast, the amount of overlap
763 between patches is constant, with each patch overlap-
764 ping each of its neighbouring patches by 80′.0. Each
765 patch covers 0.036 deg² which, due to the patch over-
766 lap, is slightly larger than the tract area divided by the
767 number of patches in a tract. The aerial coverage of
768 a patch is comparable to, but somewhat smaller than,
769 the 0.058 deg² field-of-view of a single LSSTComCam or
770 LSSTCam detector, meaning each detector image spans

771 multiple patches. The size of a tract is larger than the
772 LSSTComCam field of view. However, since each ob-
773 served field extends across more than one tract, each
774 field covers multiple tracts.

775 The skymap is integral to the production of co-added
776 images. To create a coadded image, the processing
777 pipeline selects all calibrated science images in a given
778 field that meet specific quality thresholds (§3.1 and
779 §4.5.1) for a given patch, warps them onto a single
780 consistent pixel grid for that patch, as defined by the
781 skymap, then coadds them. Each individual coadd im-
782 age therefore covers a single patch.

783 Throughout this section, the data product names are
784 indicated using monospace font. Data products are ac-
785 cessed via either the IVOA Services (§6.2.1) or the Data
786 Butler (§6.2.2).

787 3.1. Science Images

788 Science images are exposures of the night sky, as dis-
789 tinct from calibration images (§3.6.3). Although the re-
790 lease includes calibration images, thereby allowing users
791 to reprocess the raw images if needed, this is expected
792 to be necessary only in rare cases. Users are strongly
793 encouraged to start from the visit_image provided.
794 The data product names shown here are those used by
795 the Data Butler, but the names used in the IVOA Ser-
796 vices differ only slightly in that they are prepended by
797 “lsst.”.

- 798 • raw images (NSF-DOE Vera C. Rubin Observa-
799 tory 2025b) are unprocessed data received directly
800 from the camera. Each raw corresponds to a single
801 CCD from a single LSSTComCam exposure of
802 30 s duration. Each LSSTComCam exposure typ-

⁸⁷ A skymap is a tiling of the celestial sphere, organizing large-scale sky coverage into manageable sections for processing and analysis. While the skymap described here is specific to DP1, we do not anticipate major changes to the skymap in future data releases.

Table 4. Number of `raw` images per field and band. Each `raw` image corresponds to a single 30-second LSSTComCam exposure on one CCD. Most exposures produce nine `raw` images, one per sensor in the focal plane, however some yield fewer due to occasional hardware or readout issues.

Field Code	Band						Total
	<i>u</i>	<i>g</i>	<i>r</i>	<i>i</i>	<i>z</i>	<i>y</i>	
47_Tuc	54	90	288	171	0	45	648
ECDFS	387	2070	2133	1455	1377	270	7692
EDFS_comcam	180	549	783	378	378	180	2448
Fornax_dSph	0	45	225	108	0	0	378
Rubin_SV_095_-25	297	738	756	207	540	90	2628
Rubin_SV_38_7	0	396	360	495	180	0	1431
Seagull	90	333	387	0	90	0	900
Total	1008	4221	4932	2814	2565	585	16125

ically produces up to nine `raws`, one per sensor in the focal plane. However, a small number of exposures resulted in fewer than nine `raw` images due to temporary hardware issues or readout faults.

In total, DP1 includes 16125 `raw` images. Table 4 provides a summary by target and band. A `raw` contains 4608×4096 pixels, including prescan and overscan, and occupies around 18 MB of disk space.⁸⁸ The field of view of a single `raw`, excluding prescan and overscan regions, is roughly $0^{\circ}.23 \times 0^{\circ}.22 \approx 0.051 \text{ deg}^2$, corresponding to a plate scale of $0''.2$ per pixel.

- `visit_images` (NSF-DOE Vera C. Rubin Observatory 2025c) are fully-calibrated processed images. They have undergone instrument signature removal (§4.2.1) and all the single frame processing steps described in §4.2 which are, in summary: PSF modeling, background subtraction, and astrometric and photometric calibration. As with `raws`, a `visit_image` contains processed data from a single CCD resulting from a single 30 s LSSTComCam exposure. As a consequence, a single LSSTComCam exposure typically results in nine `visit_images`. The handful of exposures with fewer than nine `raw` images also have fewer than nine `visit_images`, but there are an additional 153 `raw` that failed processing and for which there

⁸⁸ Each amplifier image contains 3 and 64 columns of serial prescan and overscan pixels, respectively, and 48 rows of parallel overscan pixels, meaning a `raw` contains 4072×4000 exposed pixels.

is thus no corresponding `visit_image`. The majority of failures – 131 in total – were due to challenges with astrometric fits or PSF models in the 47_Tuc crowded field. The other failures were in the Rubin_SV_095_-25 (9 failures), ECDFS (8), Fornax_dSph (3), and EDFs_comcam (2) fields.

In total, there are 15972 `visit_images` in DP1. Each `visit_image` comprises three images: a calibrated science image, a variance image, and a pixel-level bitmask that flags issues such as saturation, cosmic rays, or other artifacts. Each `visit_image` also contains a position-dependent PSF model, World Coordinate System (WCS) information, and various metadata providing information about the observation and processing. The science and variance images and the pixel mask each contain 4072×4000 pixels. In total, a single `visit_image`, including all extensions and metadata, occupies around 110 MB of disk space. A plot showing the normalized cumulative histogram of the 5σ depths of all the `visit_images` in DP1 is shown in Figure 8.

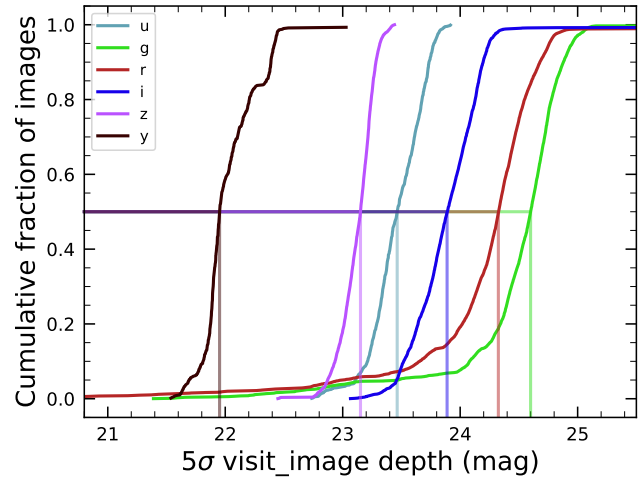


Figure 8. Normalized cumulative histograms of the 5σ depths of all `visit_images` in each band. The vertical lines indicate the 50th percentiles for each band (see legend).

- `deep_coadds` (NSF-DOE Vera C. Rubin Observatory 2025d) are the product of warping and co-adding multiple `visit_images` covering a given patch, as defined by the skymap. `deep_coadds` are created on a per-band basis, meaning only data from exposures taken with a common filter are coadded. As such, there are up to six `deep_coadds` covering each patch – one for each of the six LSSTComCam bands. The process of producing

`deep_coadds` is described in §4.5 but, to summarize, it involves the selection of suitable `visit_images` (both in terms of `patch` coverage, band, and image quality), the warping of those `visit_images` onto a common pixel grid, and the co-adding of the warped `visit_images`. To be included in a DP1 `deep_coadd`, a `visit_image` needed to have a PSF FWHM smaller than $1''.7$. Of the 15972 `visit_images`, 15375 satisfied this criterion and were therefore used to create `deep_coadds`.

There are a total of 2644 `deep_coadds` in DP1. As mentioned above, a single `deep_coadd` covers one `patch`, and includes a small amount of overlap with its neighboring `patch`. The skymap used for DP1 defines a `patch` as having an on-sky area of 0.028 deg^2 excluding overlap, and 0.036 deg^2 including overlap. A single `deep_coadd` – including overlap – contains 3400×3400 equal-sized pixels, corresponding to a platescale of $0''.2$ per pixel. Each `deep_coadd` contains the science image (i.e., the coadd), a variance image, and a pixel mask; all three contain the same number of pixels. Each `deep_coadd` also contains a position-dependent PSF model (which is the weighted sum of the PSF models of the input `visit_images`), WCS information, plus various `metadata`.

The number of `visit_images` that contributed to a given `deep_coadd` varies across the patch; the Survey Property Maps can be consulted to gain insights into the total exposure time at all locations covered by the survey. Similarly, since coadds always cover an entire `patch`, it is common for a `deep_coadd` to contain regions that were not covered by any of the selected `visit_images`, particularly if the `patch` is on the outskirts of a field and was thus not fully observed. By the nature of how coadds are produced, such regions may contain seemingly valid `flux` values (i.e., not necessarily zeros or NaNs), but will instead be flagged with the `NO_DATA` flag in the pixel mask. It is therefore crucial that the pixel mask be referred to when analyzing `deep_coadds`.

- `template_coadds` (NSF-DOE Vera C. Rubin Observatory 2025e) are those created to use as templates for difference imaging, i.e., the process of subtracting a template image from a `visit_image` to identify either variable or `transient` objects. It should be noted, however, that `template_coadds` are not themselves subtracted from `visit_images` but are, instead, warped to match the WCS of a `visit_image`. It is this warped

template that is subtracted from the `visit_image` to create a difference image.⁸⁹ As with `deep_coadds`, `template_coadds` are produced by warping and co-adding multiple `visit_images` covering a given skymap-defined `patch`. The process of building `template_coadds` is the same as that for `deep_coadds`, but the selection criteria differ between the two types of coadd. In the case of `template_coadds`, one third of `visit_images` covering the `patch` in question with the narrowest PSF FWHM are selected. If one third corresponds to fewer than twelve `visit_images` (i.e., there are fewer than 36 `visit_images` covering the `patch`), then the twelve `visit_images` with the narrowest PSF FWHM are selected. Finally, if there are fewer than twelve `visit_images` covering the `patch`, then all `visit_images` are selected. Of the 15972 `visit_images`, 13113 were used to create `template_coadds`. This selection strategy is designed to optimize for seeing when a `patch` is well-covered by `visit_images`, yet still enable the production of `template_coadds` for poorly-covered patches. As with `deep_coadds`, the number of `visit_images` that contributed to a `template_coadd` varies across the patch.

DP1 contains a total of 2730 `template_coadds`.⁹⁰ As with `deep_coadds`, a single `template_coadd` covers a single `patch`. Since the same skymap is used when creating both `deep_coadd` and `template_coadds`, the on-sky area and pixel count of `template_coadds` are the same as that of a `deep_coadd` (see above). Similarly, `template_coadds` contain the science image (i.e., the coadd), a variance image, and a pixel mask; all three contain the same number of pixels. Also included are the PSF model, WCS information, and `metadata`. As is the case for `deep_coadd`, those pixels within `template_coadds` that are not covered by any of the selected `visit_images` may still have seemingly valid values, but are indicated with the `NO_DATA` flag within the pixel mask.

- `difference_images` (NSF-DOE Vera C. Rubin Observatory 2025f) are generated by the subtraction of the warped, scaled, and PSF-matched `template_coadd` from the `visit_image` (see §4.6.1).

⁸⁹ For storage space reasons, warped templates are not retained for DP1, as they can be readily and reliably recreated from the `template_coadds`.

⁹⁰ The difference in the number of `deep_coadds` and `template_coadds` is due to the difference in the `visit_image` selection criteria for each coadd.

In principle, only those sources whose `flux` has changed relative to the `template_coadd` should be apparent (at a significant level) within a `difference_image`. In practice, however, there are numerous spurious sources present in `difference_images` due to unavoidably imperfect template matching.

In total, there are 15972 `difference_images` in `DP1`, one for each `visit_image`.

Like `visit_images`, `difference_images` contain the science (i.e., difference) image, a variance image, and a pixel mask; all three contain the same number of pixels, which is the same as that of the input `visit_image`. Also included is the `PSF` model, `WCS` information, and `metadata`.

- Background images contain the model `background` that has been generated and removed from a science image. `visit_images`, `deep_coadds` and `template_coadds` all have associated `background` images.⁹¹ Background images contain the same number of pixels as their respective science image, and there is one `background` image for each `visit_image`, `deep_coadd`, and `template_coadd`. Difference imaging analysis also measures and subtracts a `background` model, but the `difference_background` data product is not written out by default and is not part of `DP1`.

Background images are not available via the `IVOA` Service; they can only be accessed via the `Butler` Data Service.

3.2. Catalogs

Here we describe science-ready tables produced by the science pipelines. All but one of the catalogs described here contain data for detections in the images described in §3.1, the exception being the `Calibration` catalog, which contains reference data obtained from previous surveys. Observatory-produced `metadata` tables are described in §3.5. Each type of catalog contains measurements for either Sources detected in `visit_images` and `difference_images`, or Objects detected in `deep_coadds`.

While the `Source`, `Object`, `ForcedSource`, `DiaSource`, `DiaObject`, and `ForcedSourceOnDiaObject` catalogs described below each differ in terms of their specific columns, in general they each contain: one or more unique identification numbers, positional informa-

tion, one or more types of `flux` measurements (e.g., aperture fluxes, `PSF` fluxes, Gaussian fluxes, etc.), and a series of boolean flags (indicating, for example, whether the source/object is affected by saturated pixels, cosmic rays, etc.) for each source/object. The Solar System catalogs `SSObject` and `SSSource` deviate from this general structure in that they instead contain orbital parameters for all known asteroids. Where applicable, all measured properties are reported with their associated 1σ uncertainties.

Since `DP1` is a preview, it does not include all the catalogs expected in a full `LSST Data Release`. Additionally, the catalogs it does include may be missing some columns planned for future releases. Where this is known to be the case, we note what data are missing in the catalog descriptions that follow.

Catalog data are stored in the `Qserv` database (§6.5.1) and are accessible via `Table Access Protocol (IVOA standard) (IVOA)`, and an online `DP1` catalog schema is available at <https://sdm-schemas.lsst.io/dp1.html>. Catalog data are also accessible via the `Data Butler` (see §6.2.2).

- The `Source` catalog (`NSF-DOE Vera C. Rubin Observatory 2025g`) contains data on all sources which are, prior to deblending (§4.5.2), detected with a greater than 5σ significance in each individual visit. The detections reported in the `Source` catalog have undergone deblending; in the case of blended detections, only the deblended sources are included in the `Source` catalog. It is important to note that while the criterion for inclusion in a `Source` catalog is a $> 5\sigma$ detection in a `visit_image` prior to deblending, the positions and fluxes are reported post-deblending. Hence, it is possible for the `Source` catalog to contain sources whose `flux-to-error` ratios – potentially of all types (i.e., aperture `flux`, `PSF flux`, etc.) – are less than 5.

In addition to the general information mentioned above (i.e., IDs, positions, fluxes, flags), the `Source` catalog also includes basic `shape` and extendedness information.

The `Source` catalog contains data for 46 million sources in `DP1`.

A cumulative histogram showing the `PSF` magnitudes of all sources contained within the `Source` catalogue is presented in the top panel of [Figure 9](#)

- The `Object` catalog (`NSF-DOE Vera C. Rubin Observatory 2025h`) contains data on all objects detected with a greater than 5σ significance in the `deep_coadds`. With coadd images produced on a

⁹¹ In future data releases, `background` images may be included as part of their respective science image data product.

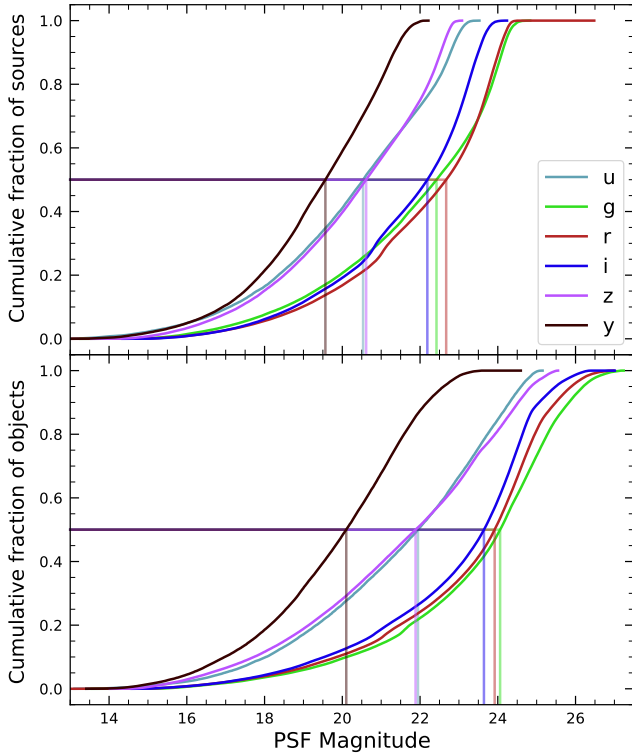


Figure 9. Normalized cumulative histograms of the PSF magnitudes of all $> 5\sigma$ -detected **sources** (top panel) and **objects** (bottom panel) contained in the **Source** and **Object** catalogs, respectively, separated according to band (see legend). The vertical lines indicate the 50th percentile for each band.

per-band basis, a $> 5\sigma$ detection in one or more of the bands will result in an object being included in the **Object** catalog. For cases where an object is detected at $> 5\sigma$ in more than one band, a cross-matching has been performed between bands to associate an object in one band with its counterpart(s) in the other bands. As such, unlike the **Source** catalog, the **Object** catalog contains data from multiple bands. The objects reported in the **Object** catalog have also undergone deblending; in the case of blended detections, only the deblended child objects are included in the catalog. As with the **Source** catalog, the criterion for inclusion in the **Object** catalog is a $> 5\sigma$ detection in one of the **deep_coadds** prior to deblending, yet the positions and fluxes of objects are reported post-deblending. Hence, it is possible for **Object** catalog to contain **objects** whose **flux**-to-error ratios — potentially of all types and in all bands — are less than 5.

In addition to the general information mentioned above (i.e., IDs, positions, fluxes, flags), the **Ob-**

ject catalog also includes basic **shape** and extendedness information. While they may be included in future data releases, no photometric redshifts, Petrosian magnitudes (V. Petrosian 1976), proper motions or periodicity information are included in the **DP1** object catalogs.

The **Object** catalog contains data for 2.3 million objects in **DP1**.

- The **ForcedSource** catalog (NSF-DOE Vera C. Rubin Observatory 2025i) contains forced PSF photometry measurements performed on both **difference_images** (i.e., the **psfDiffFlux** column) and **visit_images** (i.e., the **psfFlux** column) at the positions of all the objects in the **Object** catalog, to allow assessment of the time variability of the fluxes. We recommend using the **psfDiffFlux** column when generating light curves because this quantity is less sensitive to **flux** from neighboring sources than **psfFlux**. In addition to **forced photometry** PSF fluxes, a number of boolean flags are also included in the **ForcedSource** catalog.

The **ForcedSource** catalog contains a total of 269 million entries across 2.3 million unique objects.

- The **DiaSource** catalogs (NSF-DOE Vera C. Rubin Observatory 2025j) contains data on all the sources detected at $> 5\sigma$ significance — including those associated with known Solar System objects — in the **difference_images**. Unlike sources detected in **visit_images**, sources detected in difference images (hereafter, “**DiaSource**”) have gone through an association step in which an attempt has been made to associate them into underlying objects called “**DiaObject**”. The **DiaSource** catalog consolidates all this information across multiple visits and bands. The detections reported in the **DiaSource** catalog have not undergone deblending.

The **DiaSource** catalog contains data for 3.1 million **DiaSources** in **DP1**.

- The **DiaObject** catalog (NSF-DOE Vera C. Rubin Observatory 2025k) contains the astrophysical objects that **DiaSources** are associated with (i.e., the **DiaObjects**). The **DiaObject** catalog contains only non-Solar System Objects; Solar System Objects are, instead, recorded in the **SSObject** catalog. When a **DiaSource** is identified, the **DiaObject** and **SSObject** catalogs are searched for objects to associate it with. If no association is found, a new **DiaObject** is created and the **DiaSource** is

associated to it. Along similar lines, an attempt has been made to associate `DiaObject`s across multiple bands, meaning the `DiaObject` catalog, like the `Object` catalog, contains data from multiple bands. Since `DiaObject`s are typically [transient](#) or variable (by the nature of their means of detection), the `DiaObject` catalog contains summary statistics of their fluxes, such as the mean and standard deviation over multiple epochs; users must refer to the `ForcedSourceOnDiaObject` catalog (see below) or the `DiaSource` catalog for single [epoch flux](#) measurements of `DiaObject`s.

The `DIAObject` catalog contains data for 1.1 million `DiaObject`s in [DP1](#).

- The `ForcedSourceOnDiaObject` catalog ([NSF-DOE Vera C. Rubin Observatory 2025l](#)) is equivalent to the `ForcedSource` catalog, but contains [forced photometry](#) measurements obtained at the positions of all the `DiaObject`s in the `DiaObject` catalog.

The `ForcedSourceOnDiaObject` catalog contains a total of 197 million entries across 1.1 million unique `DiaObject`s.

- The `SSObject` catalog ([NSF-DOE Vera C. Rubin Observatory 2025m](#)), [Minor Planet Center Orbit database \(MPCORB\)](#) and `SSObject`, carry information about solar system objects. The [MPCORB](#) table provides the Minor Planet [Center](#)-computed orbital elements for all known asteroids, including those that Rubin discovered. For [DP1](#), the `SSObject` catalog serves primarily to provide the mapping between the [International Astronomical Union \(IAU\)](#) designation of an object (listed in [MPCORB](#)), and the internal `ssObjectId` identifier, which is used as a key to find solar system object observations in the `DiaSource` and `SSSource` tables. The `SSObject` catalog contains data for 431 `SSObject`s in [DP1](#).

- The `SSSource` catalog ([NSF-DOE Vera C. Rubin Observatory 2025n](#)) contains data on all `DiaSource`s that are either associated with previously-known Solar System Objects, or have been confirmed as newly-discovered Solar System Objects by confirmation of their orbital properties. As entries in the `SSSource` catalog stem from the `DiaSource` catalog, they have all been detected at $> 5\sigma$ significance in at least one band. The `SSSource` catalog contains data for 5988 Solar System Sources.

- The `CcdVisit` catalog ([NSF-DOE Vera C. Rubin Observatory 2025o](#)) contains data for each individual processed `visit_image`. In addition to technical information, such as the on-sky coordinates of the central pixel and measured pixel scale, the `CcdVisit` catalog contains a range of data quality measurements, such as whole-image summary statistics for the [PSF](#) size, zeropoint, sky [background](#), sky noise, and quality of astrometric solution. It provides an efficient method to access `visit_image` properties without needing to access the image data. When combined with the data contained in the `Visit` table described in [§3.5](#), it provides a full picture of the telescope pointing and sky conditions at the time of observation.

The `CcdVisit` catalog contains entries summarizing data for all 16071 `visit_image`s.

- The `Calibration` catalog is the reference catalog that was used to perform astrometric and photometric [calibration](#). It is a whole-sky catalog built specifically for [LSST](#), as no single prior reference catalog had both the depth and coverage needed to calibrate [LSST](#) data. It combines data from multiple previous reference catalogs and contains only stellar sources. Full details on how the [Calibration](#) catalog was built are provided in [P. S. Ferguson et al. \(2025\)](#)⁹². We provide a brief summary here.

For the *grizy* bands, the input catalogs were (in order of decreasing priority): [Dark Energy Survey \(DES\) Y6 Calibration Stars](#) ([E. S. Rykoff et al. 2023](#)); [Gaia-B or R Photometry \(Gaia\) \(XP\) Synthetic Magnitudes](#) ([Gaia Collaboration et al. 2023a](#)); the [Panoramic Survey Telescope and Rapid Response System \(Pan-STARRS\) 1 3PI Survey](#) ([K. C. Chambers et al. 2016](#)); [Data Release 2 of the SkyMapper survey](#) ([C. A. Onken et al. 2019](#)); and [Data Release 4 of the VLT Survey Telescope \(VST\) Asteroid Terrestrial-impact Last Alert System \(ATLAS\) survey](#) ([T. Shanks et al. 2015](#)). For the *u*-band, the input catalogs were (in order of decreasing priority): [Standard Stars from Sloan Digital Sky Survey \(SDSS\) Data Release 16](#) ([R. Ahumada et al. 2020](#)); [Gaia-XP Synthetic Magnitudes](#) ([Gaia Collaboration et al. 2023a](#)); and synthetic magnitudes generated using [Single Lens Reflex \(SLR\)](#), which estimates the

⁹² In [P. S. Ferguson et al. \(2025\)](#), the calibration reference catalog is referred to as “The Monster”. This terminology is also carried over to the [DP1 Butler](#).

u -band flux from the g -band flux and $g-r$ colors. This SLR estimates were used to boost the number of u -band reference sources, as otherwise the source density from the u -band input catalogs is too low to be useful for the LSST.

Only stellar sources were selected from each input catalog. Throughout, the Calibration catalog uses the DES bandpasses for the *grizy* bands and the SDSS bandpass for the u -band; color transformations derived from high quality sources were used to convert fluxes from the various input catalogs (some of which did not use the DES/SDSS bandpasses) to the respective bandpasses. All sources from the input catalogs are matched to *Gaia-Data Release 3 (DR3)* sources for robust astrometric information, selecting only isolated sources (i.e., no neighbors within $1''$).

After collating the input catalogs and transforming the fluxes to the standard DES/SDSS bandpasses, the catalog was used to identify sources within a specific region of the sky. This process generated a set of standard columns containing positional and flux information, along with their associated uncertainties.

3.2.1. Source and Object Designations

To refer to individual sources or objects from the DP1 catalogs, one should follow the LSST DP1 naming convention that has been registered with the International Astronomical Union. Because the Source, Object, DiaSource, DiaObject, and SSObject tables each have their own unique IDs, their designations should differ. In general, source designations should begin with the string “LSST-DP1” (denoting the Legacy Survey of Space and Time, Data Preview 1), followed by a string specifying the table from which the source was obtained. These strings should be “O” (for the Object table), “S” (Source), “DO” (DiaObject), “DS” (DiaSource), or “SSO” (SSObject). Following the table identifier, the designation should contain the full unique numeric identifier from the specified table (i.e., the objectId, sourceId, diaObjectId, diaSourceId, or ssObjectId). Each component of the identifier should be separated by dashes, resulting in a designation such as “LSST-DP1-TAB-123456789012345678”. In summary, source designations should adhere to the formats listed below:

- Object: LSST-DP1-O-609788942606161356 (for objectId 609788942606161356)
- Source: LSST-DP1-S-600408134082103129 (for sourceId 600408134082103129)

- DiaObject: LSST-DP1-DO-609788942606140532 (for diaObjectId 609788942606140532)
- DiaSource: LSST-DP1-DS-600359758253260853 (for diaSourceId 600359758253260853)
- SSObject: LSST-DP1-SSO-21163611375481943 (for ssObjectId 21163611375481943)

Tables that were not explicitly mentioned in the description above do not have their own unique IDs, but are instead linked to one of the five tables listed above via a unique ID. For example, the ForcedSource table is keyed on objectId, ForcedSourceOnDiaObject uses diaObjectId, SSSource is linked to diaSourceId and ssObjectId, and MPCORB uses ssObjectId.

3.3. Survey Property Maps

Maps are two-dimensional visualizations of survey data. In DP1, these fall into two categories: Survey Property Maps and Hierarchical Progressive Survey (HiPS) Maps (P. Fernique et al. 2015). Survey Property Maps (NSF-DOE Vera C. Rubin Observatory 2025p) summarize how properties such as observing conditions or exposure time vary across the observed sky. Each map provides the spatial distribution of a specific quantity at a defined sky position for each band by aggregating information from the images used to make the deep_coadd. Maps are initially created pertract and then combined to produce a final consolidated map. At each sky location, represented by a spatial pixel in the Hierarchical Equal-Area iso-Latitude Pixelisation (HEALPix)(K. M. Górski et al. 2005) grid, values are derived using statistical operations, such as minimum, maximum, mean, weighted mean, or sum, depending on the property.

DP1 contains 14 survey property maps. The available maps describe total exposure times, observation epochs (one each for the earliest, mean, and latest observation epoch), PSF size and shape (one for each of the e^1 and e^2 shape parameters; see §5.2), PSF magnitude limits, sky background and noise levels, as well as astrometric shifts (one each for right ascension and declination) and PSF distortions (one for each of the e^1 and e^2 shape parameters) due to wavelength-dependent atmospheric Differential Chromatic Refraction (DCR) effects. They all use the dataset type format deep_coadd_<PROPERTY>_consolidated_map_<STATISTIC>. For example, deep_coadd_exposure_time_consolidated_map_sum provides a spatial map of the total exposure time accumulated per sky position in

units of seconds. All maps are stored in `HealSparse`⁹³ format. Survey property maps are only available via the `Data Butler` (§6.2.2).

Figure 10 presents three survey property maps for exposure time, PSF magnitude limit, and sky noise, computed for representative tracts and bands. Because full consolidated maps cover widely separated tracts, we use clipped per-tract views here to make the spatial patterns more discernible.

3.4. HiPS Maps

HiPS Maps (P. Fernique et al. 2015), offer an interactive way to explore seamless, multi-band tiles of the sky regions covered by DP1, allowing for smooth panning and zooming. DP1 provides multi-band HiPS images created by combining data from individual bands of `deep_coadd` and `template_coadd` images, using an improved version (Lust et al. in prep) of the algorithm presented in R. Lupton et al. (2004). These images are false-color representations generated using various filter combinations for the red, green, and blue channels.

The available filter combinations include `gri`, `izy`, `riz`, and `ugr` for both `deep_coadd` and `template_coadd`. Additionally, for `deep_coadd` only, we provide color blends such as `uug` and `grz`. Post-DP1, we plan to also provide single-band HiPS images for all `ugrizy` bands in both `Portable Network Graphics` (PNG) and `FITS` formats.

HiPS maps are only accessible through the HiPS viewer in the `Rubin Science Platform` (RSP) Portal (§6.3) and cannot be accessed via the `Data Butler` (§6.2.2). All multi-band HiPS images are provided in PNG format.

3.5. Metadata

DP1 also includes `metadata` about the observations, which are stored in the `Visit` table. We distinguish it from a catalog as the data it contains was produced by the observatory directly, rather than the science pipelines. The `Visit` table contains technical data for each visit, such as telescope pointing, camera rotation, `airmass`, exposure start and end time, and total exposure time. Some of the information contained within the `Visit` table is also contained in the `CCDVisit` catalogue described in §3.2 (e.g., exposure time), although the latter also includes information produced by the processing pipelines at a per-detector level, such as the PSF size and limiting magnitudes of a given `visit_image`.

⁹³ A sparse `HEALPix` representation that efficiently encodes data values on the celestial sphere. <https://healsparse.readthedocs.io>

3.6. Ancillary Data Products

DP1 also includes several ancillary data products. While we do not expect most users to need these, we describe them here for completeness. All the Data Products described in this section can only be accessed via the `Data Butler` (§6.2.2).

3.6.1. Standard Bandpasses

Figure 3 shows the full-system throughput of the six `LSSTComCam` filters. The corresponding transmission curves are provided as a DP1 data product. These datasets tabulate the full-system transmission of the six `LSSTComCam` filters as a function of wavelength and were used as a reference for the `LSSTComCam` DP1 photometry. The `standard_passband` dataset is keyed by band and is stored in `Astropy Table` format.

3.6.2. Task configuration, log, and metadata

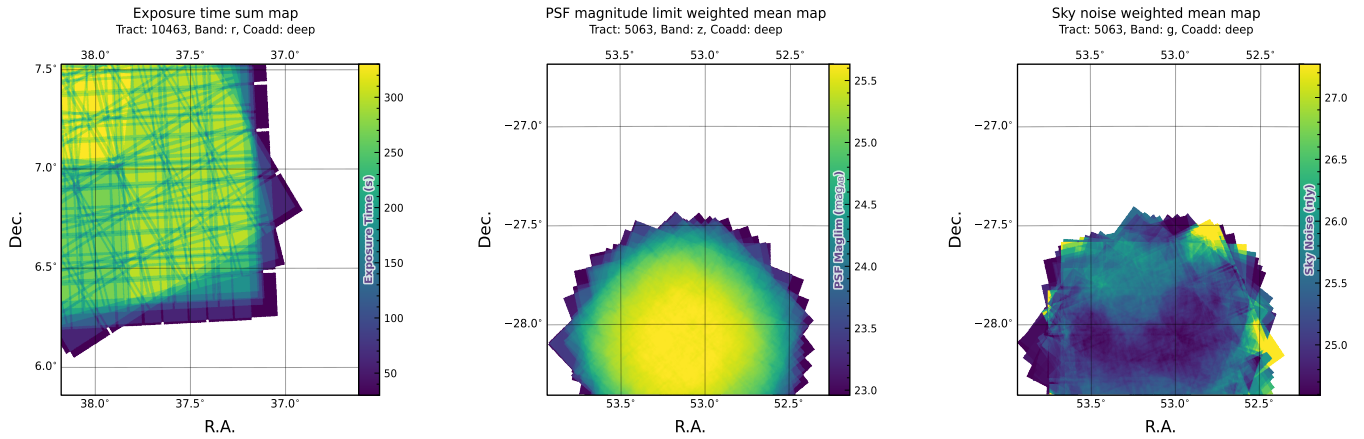
DP1 includes `provenance`-related data products such as task logs, `configuration` files, and task metadata. Configuration files record the parameters used in each processing task, while logs and `metadata` contain information output during processing. These products help users understand the processing setup and investigate potential processing failures.

3.6.3. Calibration Data Products

Calibration data products include a variety of images and models that are used to characterize and correct the performance of the camera and other system components. These include bias, dark, and flat-field images, `Photon Transfer Curve` (PTC) gains, brighter-fatter kernels (P. Antilogus et al. 2014), charge transfer inefficiency (CTI) models, linearizers, and illumination corrections. For flat-field corrections, DP1 processing used combined flats, which are averaged from multiple individual flat-field exposures to provide a stable `calibration`. These `calibration` products are essential inputs to `Instrument Signal Removal` (ISR) (§4.2.1). While these products are included in DP1 for transparency and completeness, users should not need to rerun ISR for their science and are advised to start with the processed `visit_image`.

4. DATA RELEASE PROCESSING

`Data Release Processing` (DRP) is the systematic processing of all Rubin Observatory data collected up to a certain date to produce the calibrated images, catalogs of detections, and derived data products described in Section 3. DP1 was processed entirely at the `United`



(a) Exposure time sum map for `deep_coadd tract 10463`, r-band in field `Rubin_SV_38_7`

(b) 5σ PSF magnitude limit weighted mean map for `deep_coadd tract 5063`, z-band in field ECDFS

(c) Sky noise weighted mean map for `deep_coadd tract 5063`, g-band in field ECDFS

Figure 10. Examples of survey property maps from Rubin DP1 across different bands, clipped to the boundary of a single tract for visual clarity.

1411 States Data Facility (USDF) at SLAC using 17,024 CPU 1436
1412 hours.⁹⁴ 1437

1413 This section describes the pipeline algorithms used to 1438
1414 produce DP1 and how they differ from those planned for 1439
1415 full-scale LSST data releases. Data Release Production 1440
1416 consists of four major stages: (1) single-frame processing, 1441
1417 (2) calibration, (3) coaddition, and (4) difference 1442
1418 image analysis (DIA). 1443

1419 4.1. LSST Science Pipelines Software

1420 The LSST Science Pipelines software (Rubin Observa- 1446
1421 tory Science Pipelines Developers 2025; J. D. Swinbank 1447
1422 et al. 2020) will be used to generate all Rubin Observa- 1448
1423 tory and LSST data products. It provides both the algo- 1449
1424 rithms and middleware frameworks necessary to process 1450
1425 raw data into science-ready products, enabling analysis 1451
1426 by the Rubin scientific community. Version v29.1 of the 1452
1427 pipelines was used to produce DP1⁹⁵. 1453

1428 4.2. Single Frame Processing

1429 4.2.1. Instrument Signature Removal

1430 The first step in processing LSSTComCam images is 1458
1431 to correct for the effects introduced by the telescope and 1459
1432 detector. Each sensor and its readout amplifiers can 1460
1433 vary slightly in performance, causing images of even a 1461
1434 uniformly illuminated focal plane to exhibit discontinu- 1462
1435 ities and shifts due to detector effects. The ISR pipeline 1463

1436 aims to recover the original astrophysical signal as best 1437
1438 as possible and produce science-ready single-epoch im- 1439
1440 ages for source detection and measurement. A detailed 1440
1441 description of the ISR procedures can be found in P. 1441
1442 Fagrelius & E. S. Rykoff (2025); A. A. Plazas Malagón 1442
1443 et al. (2025). Figure 11 illustrates the model of detector 1443
1444 components and readout electronics and their impact 1444
1445 on the signal, tracing the process from photons incident 1445
1446 on the detector surface to the final quantized values⁹⁶ 1446
1447 recorded in the image files. The ISR pipeline essentially 1447
1448 “works backward” through the signal chain, correct- 1448
1449 ing the integer analog-to-digital units (ADU) raw 1449
1450 camera output back to a floating-point number of pho- 1450
1451 toelectrons created in the silicon. The physical detector, 1451
1452 shown on the left in Figure 11, is the source of effects 1452
1453 that arise from the silicon itself, such as the dark current 1453
1454 and the brighter-fatter effect (A. A. Plazas et al. 2018; 1454
1455 A. Broughton et al. 2024). After the integration time 1455
1456 has elapsed, the charge is shifted to the serial register 1456
1457 and read out, which can introduce charge transfer inef- 1457
1458 ficiencies and a clock-injected offset level. The signals 1458
1459 for all amplifiers are transferred via cables to the Read- 1459
1460 out Electronics Board (REB), during which crosstalk 1460
1461 between the amplifiers may occur. The Analog Signal 1461
1462 Processing Integrated Circuit (ASPIC) on the REB con- 1462
1463 verts the analog signal from the detector into a digital 1463
1464 signal, adding both quantization and a bias level to the 1464
1465 image. Although the signal chain is designed to be stable 1465
1466 and linear, the presence of numerous sources of non- 1466
1467 linearity indicates otherwise. 1467

⁹⁴ For future Data Releases, data processing will be distributed across the USDF, the French (FrDF) and UK (UKDF) data facilities.

⁹⁵ Documentation for this version is available at: https://pipelines.lsst.io/v/v29_1_1

⁹⁶ The images written to disk by the camera have values that are integers that come from the ADC converting an analog voltage.

The *ISR* processing pipeline for *DP1* performs, in the following order: **Analogue-to-Digital Unit (ADU)** dithering to reduce quantization effects, serial overscan subtraction, saturation masking, gain normalization, crosstalk correction, parallel overscan subtraction, linearity correction, serial **CTI** correction, image assembly, bias subtraction, dark subtraction, brighter-fatter correction, defect masking and interpolation, variance plane construction, flat fielding, and amplifier offset (amp-offset) correction⁹⁷. Flat fielding for *DP1* was performed using combined flats produced from twilight flats acquired with sufficient rotational dithering to mitigate artifacts from print-through stars, as described in §2.3.

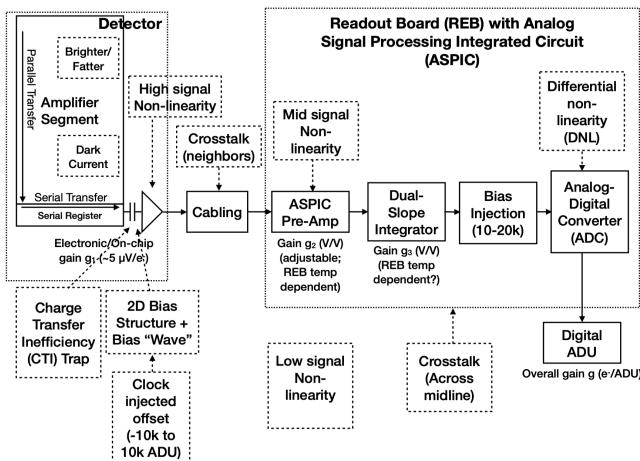


Figure 11. The model of the detector and REB components, labeled with the effects that they impart on signal.

4.2.2. Background Subtraction

The background subtraction algorithms in the LSST Science Pipelines estimate and remove large-scale background signals from science imaging. Such signals may include sky brightness from airglow, moonlight, scattered light instrumental effects, zodiacal light, and diffuse astrophysical emission. In so doing, true astrophysical sources are isolated to allow for accurate detection and measurement.

To generate a **background** model, each post-*ISR* image is divided into superpixels of 128×128 pixels. Pixels with a mask flag set that indicates that they contain no useful science data or that they contain **flux** from a preliminary source detection are masked. The iterative

⁹⁷ Amp-offset corrections are designed to address systematic discontinuities in background sky levels across amplifier boundaries. The implementation in the LSST Science Pipelines is based on the **Pan-STARRS** Pattern Continuity algorithm (C. Z. Waters et al. 2020).

3σ clipped mean of the remaining pixels is calculated for each superpixel, constructing a **background** statistics image. A sixth-order Chebyshev polynomial is fit to these values on the scale of a single detector to allow for an extrapolation back to the native pixel resolution of the post-*ISR* image.

4.3. Calibration

Stars are detected in each post-*ISR* image using a 5σ threshold. Detections of the same star across multiple images are then associated to identify a consistent set of isolated stars with repeated observations suitable for use in PSF modeling, photometric **calibration**, and astrometric **calibration**.

Initial astrometric and photometric solutions are derived using only the calibration reference catalogs (see §3.2), and an initial PSF model is fit using PSFEx (E. Bertin 2011). These preliminary solutions provide approximate source positions, fluxes, and PSF shapes that serve as essential inputs to the **calibration** process, enabling reliable source matching, selection of high-quality stars, and iterative refinement of the final astrometric, photometric, and PSF models. These preliminary solutions are subsequently replaced by more accurate fits, as described in the following sections.

4.3.1. PSF Modeling

PSF modeling in *DP1* uses the Piff (M. Jarvis et al. 2021) package. Our configuration of Piff utilizes its **PixelGrid** model with a fourth-order polynomial interpolation per **CCD**, except in the *u*-band, where star counts are insufficient to support a fourth-order fit. In this case, a second-order polynomial is used instead. Details on the choice of polynomial order, overall PSF modeling performance, and known issues are discussed in §5.2.

4.3.2. Astrometric Calibration

Starting from the astrometric solution calculated in single frame processing (§4.2), the final astrometric solution is computed using the ensemble of visits in a given band that overlap a given **tract**. This allows the astrometric solution to be further refined by using all of the isolated point sources of sufficient signal-to-noise ratio in an image, rather than only those that appear in the reference catalog, as is done in single frame processing. Using multiple whole visits rather than a single detector also allows us to account for effects that impact the full focal plane, and for the proper motion and parallax of the sources.

In order to perform the fit of the astrometric solution, isolated point sources are associated between overlapping visits and with the **Gaia DR3** (Gaia Collaboration et al. 2023b) reference catalog where possible. The

model used for DP1 consists of a static map from pixel space to an intermediate frame (the per-detector model), followed by a per-visit map from the intermediate frame to the plane tangent to the telescope boresight (the per-visit model), then finally a deterministic mapping from the tangent plane to the sky. The fit is done using the `gbdes` package (G. M. Bernstein et al. 2017), and a full description is given in C. Saunders (2024).

The per-detector model is intended to capture quasi-static characteristics of the telescope and camera. During *Rubin Operations*, the astrometric solution will allow for separate epochs with different per-detector models, to account for changes in the camera due to warming and cooling and other discrete events. However, for DP1, LSSTComCam was assumed to be stable enough that all visits use the same per-detector model. The model itself is a separate two-dimensional polynomial for each detector. For DP1, a degree 4 polynomial was used; the degree of the polynomial mapping is tuned for each instrument and may be different for LSSTCam. Further improvements may be made by including a pixel-based astrometric offset mapping, which would be fit from the ensemble of astrometric residuals, but this is not included in the DP1 processing.

The per-visit model attempts to account for the path of a photon from both atmospheric sources and those dependent on the telescope orientation. This model is also a polynomial mapping, in this case a degree 6 two-dimensional polynomial. Correction for DCR (§5.4) was not done for DP1, but will be included in LSSTCam processing during *Rubin Operations*. Future processing will also likely include a Gaussian Process fit to better account for atmospheric turbulence, as was demonstrated by W. F. Fortino et al. (2021) and P. F. Léget et al. (2021).

The final component of the astrometric calibration involves the positions of the isolated point sources included in the fit, which are described by five parameters: sky coordinates, proper motion, and parallax. While proper motions and parallaxes are not released for DP1, they are fitted for these sources in the astrometric solution to improve the astrometric calibration.

4.3.3. Photometric Calibration

Photometric calibration of the DP1 dataset is based on the Forward Global Calibration Method (FGCM) (FGCM D. L. Burke et al. 2018), adapted for the LSST Science Pipelines (H. Aihara et al. 2022; P. Fagrelus & E. S. Rykoff 2025). We used the FGCM to calibrate the full DP1 dataset with a forward model that uses a parameterized model of the atmosphere as a function of airmass along with a model of the instrument through-

put as a function of wavelength. The FGCM process typically begins with measurements of the instrumental throughput, including the mirrors, filters, and detectors. However, because full scans of the LSSTComCam as-built filters and individual detectors were not available, we instead used the nominal reference throughputs for the Simonyi Survey Telescope and LSSTCam.⁹⁸ These nominal throughputs were sufficient for the DP1 calibration, given the small and homogeneous focal plane consisting of only nine ITL detectors. The FGCM atmosphere model, provided by MODTRAN (A. Berk et al. 1999), was used to generate a look-up table for atmospheric throughput as a function of zenith distance at Cerro Pachón. This model accounts for absorption and scattering by molecular constituents of the atmosphere, including O_2 and O_3 ; absorption by water vapor; and Mie scattering by airborne aerosol particulates. Nightly variations in the atmosphere are modeled by minimizing the variance in repeated observations of stars with a Signal to Noise Ratio (SNR) greater than 10, measured using “compensated aperture fluxes”. These fluxes include a local background subtraction (see §4.2.2) to mitigate the impact of background offsets. The model fitting process incorporates all six bands (*ugrizy*) but does not include any gray (achromatic) terms, except for a linear assumption of mirror reflectance degradation, which is minimal over the short duration of the DP1 observation campaign. As an additional constraint on the fit, we use a subset of stars from the reference catalog (P. S. Ferguson et al. 2025), primarily to constrain the system’s overall throughput and establish the “absolute” calibration.

4.4. Visit Images and Source Catalogs

With the final PSF models, WCS solutions, and photometric calibrations in place, we reprocess each single-epoch image to produce a final set of calibrated visit images and source catalogs. Source detection is performed down to a 5σ threshold using the updated PSF models, followed by measurement of PSF and aperture fluxes. These catalogs represent the best single-epoch source characterization, but they are not intended for constructing light curves. For time-domain analysis, we recommend using the forced photometry tables described in §4.6.2.

4.5. Coaddition Processing

4.5.1. Coaddition

Only exposures with a seeing better than 1.7 arcseconds FWHM are included in the deep coadded images.

⁹⁸ Available at: <https://github.com/lstt/throughputs/tree/1.9>

For the template coadds, typically only the top third of visits with the best seeing are used (although see §3.1 for more details), resulting in an even tighter image quality cutoff for the template coadds. Exposures with poor PSF model quality, identified using internal diagnostics, are excluded to prevent contamination of the coadds with unreliable PSF estimates. The remaining exposures are combined using an inverse-variance weighted mean stacking algorithm.

To mitigate transient artifacts before coaddition, we apply the artifact rejection procedure described in Y. Al-Sayyad (2018) that identifies and masks features such as satellite trails, optical ghosts, and cosmic rays. It operates on a time series of PSF-matched images resampled onto a common pixel grid (“warps”) and leverages their temporal behavior to distinguish persistent astrophysical sources from transient artifacts.

Artifact rejection uses both direct (where no PSF-matching is performed) and PSF-matched warps, homogenized to a standard PSF of 1.8 arcseconds FWHM, broadly consistent with the 1.7 arcsecond FWHM seeing threshold used in data screening. A sigma-clipped mean of the PSF-matched warps serves as a static sky model, against which individual warps are differenced to identify significant positive and negative residuals. Candidate artifact regions are classified as transient if they appear in less than a small percentage of the total number of exposures, with the threshold based on the number of visits, N , as follows:

- $N = 1$ or 2 : threshold = 0 (no clipping).
- $N = 3$ or 4 : threshold = 1.
- $N = 5$: threshold = 2.
- $N > 5$: threshold = $2 + 0.03N$.

Identified transient regions are masked before coaddition, improving image quality and reducing contamination in derived catalogs.

4.5.2. Detection, Deblending and Measurement

After constructing coadded images, sources are detected in each band, merged across bands, deblended, and measured to generate the final object catalogs (§3.2). For each coadd in all six bands, we perform source detection at a 5σ detection threshold and then adjust the background with a per-patch constant (coadds are built from background-subtracted images, but the deeper detection on coadds redefines what is considered source versus background). Detections across bands are merged in a fixed priority order, *irzygu*, to form a union detection catalog, which serves as input to deblending.

Deblending is performed using the Scarlet Lite algorithm, which implements the same model as Scarlet (P. Melchior et al. 2018), but operates on a single pixel grid. This allows the use of analytic gradients, resulting in greater computational speed and memory efficiency.

Object measurement is then performed on the deblended detection footprints in each band. Measurements are conducted in three modes: independent per-band measurements, forced measurements in each band, and multiband measurements.

Most measurement algorithms operate through a single-band plugin system, largely as originally described in J. Bosch et al. (2018). The same plugins are run separately for each object on a deblended image, which uses the Scarlet model as a template to re-weight the original noisy coadded pixel values. This effectively preserves the original image in regions where objects are not blended, while dampening the noise elsewhere.

A reference band is chosen for each object based on detection significance and measurement quality using the same priority order as detection merging (*irzygu*) and a second round of measurements is performed in forced mode using the shape and position from the reference band to ensure consistent colors (J. Bosch et al. 2018).

Measurement algorithm outputs include object fluxes, centroids, and higher-order moments thereof like sizes and shapes. A variety of flux measurements are provided, from aperture fluxes and forward modeling algorithms.

Composite model (CModel) magnitudes (K. Abazajian et al. 2004; J. Bosch et al. 2018) are used to calculate the extendedness parameter, which functions as a star-galaxy classifier. Extendedness is a binary classifier that is set to 1 if the PSF model flux is less than 98.5% of the (free, not forced) CModel flux in a given band. Additionally, the extendedness in the reference band is provided as a separate column for convenience as a multiband star-galaxy classification, and is recommended generally but also specifically for objects with low signal-to-noise ratio in some bands.

Gaussian-Aperture-and-PSF (Gaussian Aperture and PSF (GAaP) K. Kuijken 2008; A. Kannawadi 2025) fluxes are provided to ensure consistent galaxy colors across bands. Sérsic model (J. L. Sérsic 1963; J. L. Sérsic 1968) fits are run on all available bands simultaneously (MultiProFit, D. S. Taranu 2025). The resulting Sérsic model fluxes are provided as an alternative to CModel and are intended to represent total galaxy fluxes. Like CModel, the Sérsic model is a Gaussian mixture approximation to a true Sérsic profile, convolved with a Gaussian mixture approximation to the PSF. Sérsic model fits also include a free centroid, with all other structural

1743 parameters shared across all bands. That is, the intrinsic
1744 model has no color gradients, but the convolved
1745 model may have color gradients if the PSF parameters
1746 vary significantly between bands.

1747 CModel measurements use a double “shapelet” (A.
1748 Refregier 2003) PSF model with a single shared shape.
1749 The Sérsic fits are intended to use a double Gaussian
1750 with independent shape parameters for each component.
1751 Due to a pipeline misconfiguration, the Sérsic fits actu-
1752 ally used the shapelet PSF parameters, with the higher-
1753 order terms ignored (since MultiProFit does not sup-
1754 port shapelet PSFs). This bug is not expected to im-
1755 pact the galaxy fluxes significantly, since the higher-
1756 order shapelet PSF parameters tend to be small, and
1757 the fix will be applied in future campaigns. Either way,
1758 the double Gaussian PSF parameters are included for
1759 each object.

1760 Further details on the performance of these algorithms
1761 are found in §5.7.

1762 4.6. Variability Measurement

1763 4.6.1. Difference Imaging Analysis

1764 Difference Image Analysis (DIA) uses the decorrelated
1765 Alard & Lupton image differencing algorithm (D. J.
1766 Reiss & R. H. Lupton 2016). We detected both posi-
1767 tive and negative DIASources at 5σ in the difference
1768 image. Sources with footprints containing both positive
1769 and negative peaks due to offsets from the template po-
1770 sition or blending were fit with a dipole centroid code,
1771 , which simultaneously fits offset positive and negative
1772 PSFs.

1773 We filter a subset of DIASources that have pixel
1774 flags characteristic of artifacts, non-astrophysical trail
1775 lengths, and unphysically negative direct fluxes. We
1776 performed a simple spatial association of DIASources
1777 into DIAObjects with a one arcsecond matching radius.

1778 The Machine Learning reliability model applied to
1779 DP1 was developed with the aim to meet the latency
1780 requirements for Rubin Alert Production when executed
1781 on CPUs. Accordingly we developed a relatively simple
1782 model: a Convolutional Neural Network with three con-
1783 volutional layers, and two fully connected layers. The
1784 convolutional layers have a 5×5 kernel size, with 16, 32,
1785 and 64 filters, respectively. A max-pooling layer of size 2
1786 is applied at the end of each convolutional layer, followed
1787 by a dropout layer of 0.4 to reduce overfitting. The last
1788 fully connected layers have sizes of 32 and 1. The ReLU
1789 activation function is used for the convolutional layers
1790 and the first fully connected layer, while a sigmoid func-
1791 tion is used for the output layer to provide a probabilistic
1792 interpretation. The cutouts are generated by extracting
1793 postage stamps of 51×51 pixels centered on the detected

1794 sources. The input data of the model consist of the tem-
1795 plate, science, and difference image stacked to have an
1796 array of shape (3, 51, 51). The model is implemented
1797 using PyTorch (J. Ansel et al. 2024). The Binary Cross
1798 Entropy loss function was used, along with the Adap-
1799 tive Moment Estimation (Adam) optimizer with a fixed
1800 learning rate of 1×10^{-4} , weight decay of 3.6×10^{-2} , and
1801 a batch size of 128. The final model uses the weights
1802 that achieved the best precision/purity for the test set.
1803 Training was done on the SLAC Shared Scientific Data
1804 Facility (S3DF) with an NVIDIA model L40S GPU.

1805 The model was initially trained using simulated data
1806 from the second DESC Data Challenge (DC2; (LSST
1807 Dark Energy Science Collaboration (LSST DESC) et al.
1808 2021)) plus randomly located injections of PSFs to in-
1809 crease the number of real sources, for a total of 89,066
1810 real sources. The same number of bogus sources were se-
1811 lected at random from non-injected DIASources. Once
1812 the LSSTComCam data were available, the model was
1813 fine-tuned on a subset of the data containing 183,046
1814 sources with PSF injections. On the LSSTComCam test
1815 set, the model achieved an accuracy of 98.06%, purity
1816 of 97.87%, and completeness of 98.27%. As discussed
1817 in §5.8, the injections used to train this model version
1818 do not capture all types of astrophysical variability, so
1819 performance on the test set will not be representative
1820 for variable stars, comets, and other types of variable
1821 objects.

1822 4.6.2. Light Curves

1823 To produce light curves, we perform multi-epoch
1824 forced photometry on both the direct visit images and
1825 the difference images. For light curves we recom-
1826 mend the forced photometry on the difference images
1827 (psDiffFlux on the ForcedSource Table), as it isolates
1828 the variable component of the flux and avoids contam-
1829 ination from static sources. In contrast, forced pho-
1830 tometry on direct images includes flux from nearby or
1831 blended static objects, and this contamination can vary
1832 with seeing. Centroids used in the multi-epoch forced
1833 photometry stage are taken either from object positions
1834 measured on the coadds or from the DIAObjects (the
1835 associated DIASources detected on difference images).

1836 4.6.3. Solar System Processing

1837 Solar system processing in DP1 consists of two key
1838 components: the association of observations (sources)
1839 with known solar system objects, and the discovery of
1840 previously unknown objects by linking sets of tracklets⁹⁹.

⁹⁹ A tracklet is defined as two or more detections of a moving object candidate taken in close succession in a single night.

To generate expected positions, ephemerides are computed for all objects found in the Minor Planet Center orbit catalog using the `Sorcha` survey simulation toolkit (Merritt et al., in press)¹⁰⁰. To enable fast lookup of objects potentially present in an observed visit, we use the `mpsky` package (M. Juric 2025). In each image, the closest DiaSource within 1 arcsecond of a known solar system object’s predicted position is associated to that object.

Solar system discovery uses the `heliolinc` package of asteroid identification and linking tools (A. Heinze et al. 2023). The suite consists of the following tasks:

- Tracklet creation with `make_tracklets`
- Multi-night `tracklet` linking with `heliolinc`
- Linkage post processing (orbit fitting, outlier rejection, and de-duplication) with `link_purify`

The inputs to the `heliolinc` suite included all sources detected in difference images produced by an early processing of the `LSSTComCam` commissioning data, including some that were later rejected as part of `DP1` processing and hence are not part of `DP1`.

About 10% of all commissioning visits targeted the near-ecliptic field `Rubin_SV_38_7` chosen to facilitate asteroid discovery. `Rubin_SV_38_7` produced the vast majority of asteroid discoveries in `DP1`, as expected, but a few were found in off-ecliptic fields as well.

Tracklet creation with `make_tracklets` used an upper limit angular velocity of 1.5 `deg/day`, faster than any main belt asteroid and in the range of many `Near-Earth Object (NEO)` discoveries. To minimize false tracklets from fields observed multiple times per night, the minimum `tracklet` length was set to three detections, and a minimum on-sky motion of five arcseconds was required for a valid `tracklet`.

The heart of the discovery pipeline is the `heliolinc` task, which connects (“links”) tracklets belonging to the same object over a series of nights. It employs the `HelioLinC3D` algorithm (S. Eggl et al. 2020; A. Heinze et al. 2022), a refinement of the original `HelioLinC` algorithm of M. J. Holman et al. (2018).

The `heliolinc` run tested each `tracklet` with 324 different hypotheses spanning heliocentric distances from 1.5 to 9.8 `astronomical unit (au)` and radial velocities spanning the full range of possible bound orbits (eccentricity 0.0 to nearly 1.0). This range of distance encompasses all main belt asteroids and Jupiter Trojans, as well as many comets and Mars-crossers and

some `NEOs`. Smaller heliocentric distances were not attempted here because nearby objects move rapidly across the sky and hence were not likely to remain long enough in an `LSSTComCam` field to be discovered. Candidate linkages, groups of tracklets whose propagated orbits cluster within a radius of 1.33×10^3 `au` at 1 `au`, are identified, then post-processed via `link_purify` to yield a final, non-overlapping set of high-confidence asteroid candidates, ranked by orbit-fit residuals and related metrics.

5. PERFORMANCE CHARACTERIZATION AND KNOWN ISSUES

In this section, we provide an assessment of the `DP1` data quality and known issues.

5.1. Sensor Anomalies and ISR

In addition to the known detector features identified before `LSSTComCam` commissioning, most of which are handled by the `ISR` processing (see §4.2.1), we discovered a number of new types of anomalies in the `DP1` data. Since no corrections are currently available for these anomalies, they are masked and excluded from downstream data products.

5.1.1. Vampire Pixels

“Vampire” pixels are visible on the images as a bright defect surrounded by a region of depressed flux, as though the defect is stealing charge from its neighboring pixels. Figure 12 shows an example of a vampire pixel near the center of `R22_S11` on an `r-band` flat.

From studies on evenly illuminated images, vampires appear to conserve charge. Unfortunately, no unique optimum way exists to redistribute this stolen flux so, following visual inspection, a defect mask was created to exclude them from processing. We have found some similar features on the `ITL` detectors on `LSSTCam`, and will use the same approach to exclude them.

5.1.2. Phosphorescence

Some regions of the `LSSTComCam` CCD raft were seen to contain large numbers of bright defects. An example is shown in Figure 13 in a `g-band` flat. On further investigation, it appears that on some detectors a layer of photoresist wax was incompletely removed from the detector surface during production. As this wax is now trapped below the surface coatings, there is no way to physically clean these surfaces. If this wax responded to all wavelengths equally, then it would likely result in quantum efficiency dips, which might be removable during flat correction. However, it appears that this wax is slightly phosphorescent, with a decay time on the order

¹⁰⁰ Available at <https://github.com/dirac-institute/sorcha>

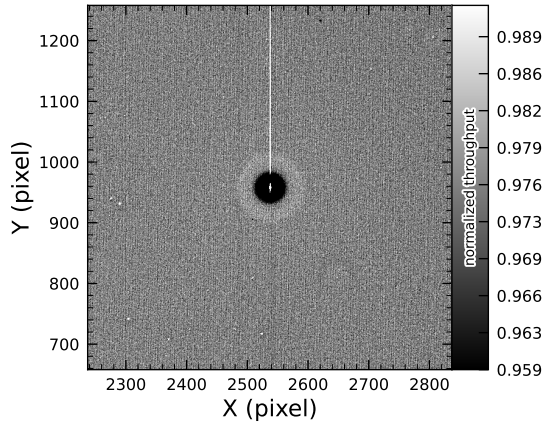


Figure 12. A large vampire pixel near the center of R22_S11, as seen on the r -band flat. This clearly shows the central hot "vampire" pixels, surrounded by a region of depressed signal, with a brighter ring surrounding that caused by the local electric field effects. The charge contained in the central pixels is incompletely shifted as the image is read, and that charge leaks out into subsequent rows as they are shifted through the remnant charge. The columns that contain the hot pixels are masked as defects in all processing, as this feature cannot be otherwise corrected.

1937 of minutes, resulting in the brightness of these defects
 1938 being dependent on the illumination of prior exposures.
 1939 The worst of these regions were excluded with manual
 1940 masks.

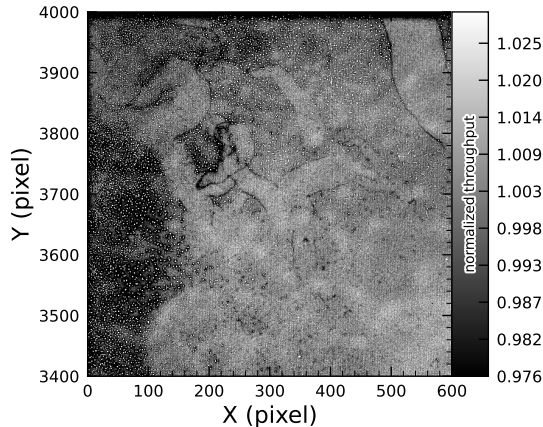


Figure 13. The top left corner of R22_S01 in the g -band flat, showing the many small defect features that are caused by the remnant photoresist wax. A single large defect box masks this region from further analysis to prevent these features from contaminating measurements.

1941

1942

5.1.3. Crosstalk

1943

1944 Crosstalk refers to unwanted signal interference be-
 1945 tween adjacent pixels or amplifiers. We use an aver-
 1946 age inter-amp crosstalk correction based on laboratory
 1947 measurements with LSSTCam. These average correc-
 1948 tions proved satisfactory, and so have been used as-is
 1949 for DP1 processing. There are, however, some residual
 1950 crosstalk features present post-correction, with a ten-
 1951 dency towards over-subtraction. Figure 14 shows an ex-
 1952 ample of a bright star with over-subtracted crosstalk
 1953 residuals visible on neighboring amplifiers to both sides
 1954 on exposure 2024120600239, detector R22_S02.

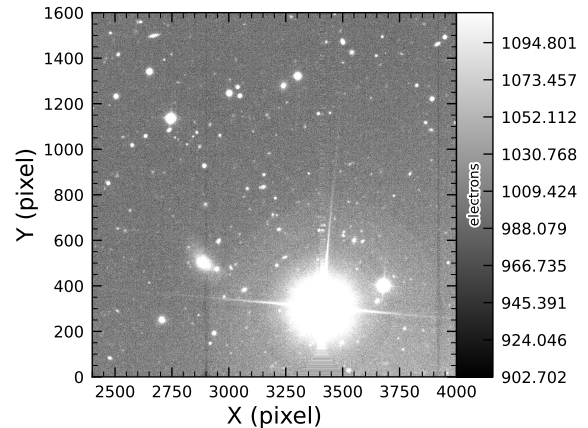


Figure 14. An example of a bright star with over-sub-
 1955 tracted crosstalk residuals visible on neighboring ampli-
 1956 fiers to both sides (exposure 2024120600239, detector R22_S02).
 1957 The horizontal banding stretching from the center of the star
 1958 shows the interpolation pattern covering the saturated core
 1959 and the ITL edge bleed near the serial register.

5.1.4. Bleed Trails

1955

1956

1957

1958 Bleed trails are produced when charge from saturated
 1959 pixels spills into adjacent pixels. Bleed trails were an-
 1960 ticipated on LSSTComCam sensors, but they appear in
 1961 more dramatic forms than had been expected. As a
 1962 bleed trail nears the serial register, it fans out into a
 1963 "trumpet" shaped feature. Although bright, these fea-
 1964 tures do not have consistently saturated pixels. In DP1
 1965 these "edge bleeds" were identified and masked.

1966

1967

1968

1969

1970

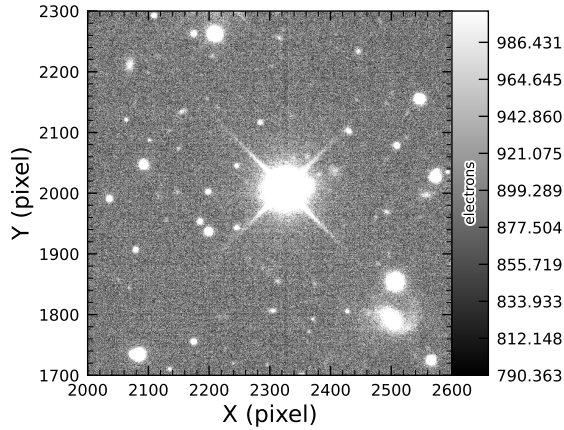
1971

1972

1973

Saturated sources can create a second type of bleed,
 where the central bleed drops below the background
 level. The depressed columns along these trails extend
 across the entire readout column of the detector, cross-
 ing the detector mid-line. We developed a model for
 these to identify which sources are sufficiently saturated
 to result in such a trail, which is then masked. As this
 kind of trail appears only on the ITL detectors, we've

1974 named these features “ITL dips”. Figure 15 shows an
 1975 example of a bright star exhibiting the “ITL dip” phe-
 1976 nomenon on exposure: 2024121000503, detector: R22_-
 1977 S21.



1978 **Figure 15.** A bright star showing the “ITL dip” phe-
 1979 nomenon, in which a dark trail extends out from the star
 1980 to the top and bottom edges of the detector (exposure:
 1981 2024121000503, detector: R22_S21).

1982 5.2. PSF Models

1983 To characterize PSF performance, we use adaptive
 1984 second moments (G. M. Bernstein & M. Jarvis 2002)
 1985 measured on PSF stars and on the PSF model using
 1986 the HSM implementation (C. Hirata & U. Seljak 2003;
 1987 R. Mandelbaum et al. 2005). All measurements are ex-
 1988 pressed in the pixel coordinate frame of each detector.
 1989 We characterize the performance of the PSF using the
 1990 classical trace of the second moment matrix T , along
 1991 with the ellipticity parameters e^1 and e^2 . Measure-
 1992 ments on the observed PSF stars are denoted as
 1993 T_{PSF} , e_{PSF}^1 , e_{PSF}^2 , while those from PSF models are
 denoted as T_{model} , e_{model}^1 , e_{model}^2 . We compare two PSF
 modeling approaches:

- 1994 • Piff with second-order polynomial interpolation
 1995 (Piff O2), the pipeline’s default, and
- 1996 • Piff with fourth-order polynomial interpolation
 1997 (Piff O4), which serves as the final DP1 PSF
 1998 model.

1999 Table 5 summarizes each model’s ability to reconstruct
 2000 the mean T , e^1 , and e^2 on LSSTComCam. Both models
 2001 exhibit a negative residual bias in the reconstructed PSF
 2002 size, with Piff O4 providing improved performance over
 2003 Piff O2.

2004 An alternative approach to evaluating the perfor-
 2005 mance of the PSF model is to examine the average $\delta T/T$,
 2006

Table 5. Observed mean values and comparison of model
 residuals, across all visits and filters

Quantity	Observed	Piff O2	Piff O4
		$\times 10^{-4}$	$\times 10^{-4}$
$\langle T \rangle$ (pixel ²)	11.366 ± 0.003		
$\langle e^1 \rangle$	$(-6.07 \pm 0.05) \times 10^{-3}$		
$\langle e^2 \rangle$	$(-4.57 \pm 0.05) \times 10^{-3}$		
$\langle e \rangle$	$(8.794 \pm 0.004) \times 10^{-2}$		
$\langle \delta T/T \rangle$		-4.0 ± 0.2	-5.0 ± 0.2
$\langle \delta e^1 \rangle$		0.6 ± 0.1	0.5 ± 0.1
$\langle \delta e^2 \rangle$		0.0 ± 0.1	0.0 ± 0.1

2007 where δT is $T_{\text{PSF}} - T_{\text{model}}$, across visits, projected onto
 2008 focal-plane coordinates, as shown in Figure 16. Piff re-
 2009 veals strong spatial correlations in the residuals, includ-
 2010 ing a systematic offset consistent with the results pre-
 2011 sented in Table 5. The presence of these spatial struc-
 2012 tures motivated the adoption of fourth-order polynomial
 2013 interpolation in all bands except u -band. Although not
 2014 shown in Figure 16, residual patterns persist even with
 2015 third-order interpolation, indicating that it is insuffi-
 2016 cient to capture the complexity of the PSF variation.
 2017 Increasing the interpolation order to five would nomi-
 2018 nally reduce the residuals further, but the limited num-
 2019 ber of stars available on some CCDs would not provide
 2020 adequate constraints for such a model, while the result-
 2021 ing improvement would likely be minimal. Preliminary
 2022 analysis of LSSTCam data in the laboratory at SLAC
 2023 National Accelerator Laboratory (SLAC) shows that the
 2024 ITL sensors exhibit the same pattern as ITL sensors on
 2025 LSSTComCam.

2026 Another way to look at the PSF modeling quality is
 2027 via whisker plots of the PSF second and fourth moments
 2028 and their modeling residuals projected on a part of the
 2029 sky. In addition to the second moment, the spin-2 fourth
 2030 moments, $e^{(4)}$, are defined as:

$$2031 e_1^{(4)} = M_{40} - M_{04}$$

$$2032 e_2^{(4)} = 2(M_{31} - M_{13}),$$

2033 where M_{pq} are the standardized higher moments as de-
 2034 fined in T. Zhang et al. (2023) measured on stars and
 2035 PSF models. Figure 17 shows the whisker plots of e ,
 2036 $e^{(4)}$ (top rows), and δe , $\delta e^{(4)}$ in the ECDFS field. The
 2037 direction of a whisker represents the orientation of the
 2038 shape, while the length represents the amplitude $|e|$ or
 2039 $|e^{(4)}|$. We observe coherent patterns in both the PSF
 2040 moments and the residuals, the latter of which warrants
 2041

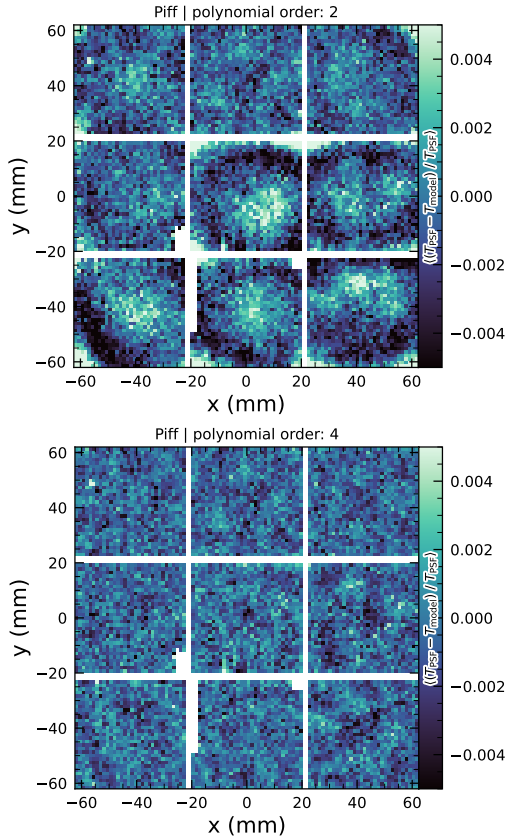


Figure 16. Average across all visits of $\delta T/T$ for Piff O2 and Piff O4 modeling on LSSTComCam. Averages are computed using a 120×120 binning.

2042 further investigation if it persists in future data releases.
 2043 >

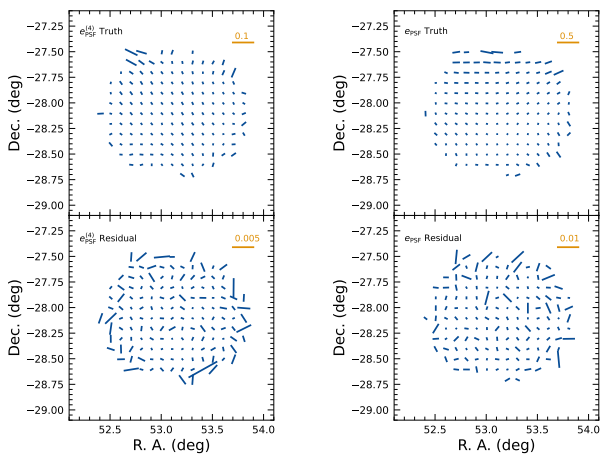


Figure 17. Whisker plots for the ECDFS field for e , $e^{(4)}$ and δe , $\delta e^{(4)}$.

2044
 2045

2046 **Figure 18** shows a plot of $\delta T/T$ versus stellar magni-
 2047 tude, which can reveal any dependencies between PSF
 2048 size and flux. We also repeat this analysis in color bins
 2049 to probe chromatic effects. Binning by color uncovers
 2050 a clear color dependence, as was also seen in DES (M.
 2051 Jarvis et al. 2021). The residual is consistent with Ta-
 2052 ble 5 and its cause is unknown. DP1 does not include the
 2053 color correction implemented in the DES Year 6 anal-
 2054 ysis, T. Schutt et al. (2025). This will be included in
 2055 processing of future data releases.

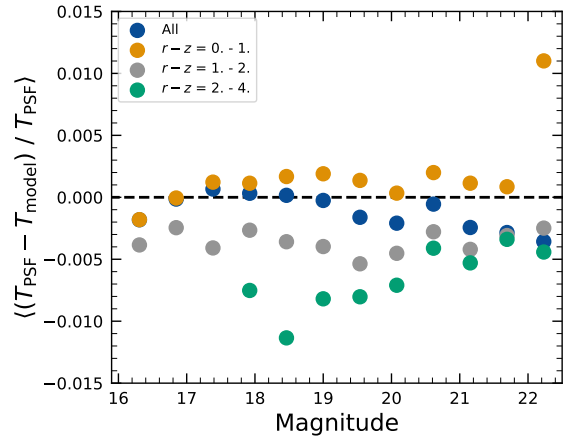


Figure 18. Binned $\delta T/T$ as a function of magnitude across all visits and filters and in bins of stellar colors.

2056
 2057
 2058
 2059
 2060
 2061
 2062
 2063
 2064
 2065

As noted in Rubin Observatory Science Pipelines De-
 velopers (2025), two key Piff features were not used in
 the DP1 processing. PSF color dependence was not im-
 plemented, and, while Rubin software allows Piff to work
 with sky coordinates (including WCS transformations),
 it does not yet correct for sensor-induced astrometric
 distortions such as tree rings (H. Y. Park et al. 2017).
 Both features are planned for upcoming releases.

5.3. Astrometry

2066
 2067
 2068
 2069
 2070
 2071
 2072
 2073
 2074
 2075
 2076
 2077
 2078
 2079
 2080

To characterize astrometric performance, we evaluate
 both internal consistency and agreement with an exter-
 nal reference. The primary measure of internal consis-
 tency is the repeatability of position measurements for
 the same object, defined as the RMS of the astrometric
 distance distribution for stellar pairs having a specified
 separation in arcminutes. We associate isolated point
 sources across visits and compute the rms of their fitted
 positions, rejecting any stars with another star within
 $2''$. **Figure 19** shows the median per-tract rms astro-
 metric error in RA for all isolated point sources, both
 after the initial calibration and after the final calibra-
 tion, which includes proper motion corrections. The re-
 sults indicate that the astrometric solution is already

2081 very good after the initial calibration. Global calibration
 2082 yields only modest improvement, likely due to the
 2083 short time span of DP1 and the minimal distortions
 2084 in the LSSTComCam. In the main survey, the longer
 2085 time baseline and greater distortions near the LSSTCam
 2086 field edges will make global calibration more impactful.
 2087 An additional measure of internal consistency is the re-

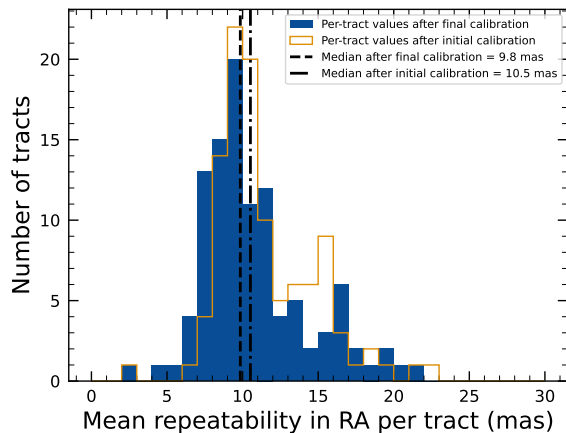


Figure 19. Mean per-tract astrometric repeatability of measurements of isolated point sources in RA in visits across all bands.

2088
 2089
 2090 peatability of separations between objects at a given distance. To compute this, we identify pairs of objects that are separated by a specified distance and measure their precise separation during each visit in which both objects are observed. The scatter in these separation measurements provides an indication of the internal consistency of the astrometric model. Figure 20 shows the median separation for pairs of objects separated by approximately 5 arcminutes, computed per tract after the final calibration. These values are already approaching the design requirement of 10 mas.

2100
 2102 To assess external consistency, we consider the median separation between sources not included in the astrometric fit and associated objects from a reference catalog. For this, we use the Gaia DR3 catalog, with the object positions shifted to the observation epoch using the Gaia proper motion parameters. Figure 21 shows the median separation for each visit in the r -band in tract 4849 in the ECDFS fields (Table 6). The calculated values are almost all within 5 mas, well below the design requirement of 50 mas for the main survey. By examining the astrometric residuals, we can assess whether there are distortions not accounted for by the astrometric model. In some cases, residuals from a single visit exhibit behavior consistent with atmospheric turbulence, as shown in Figure 22, which is characterized by a curl-free gradient

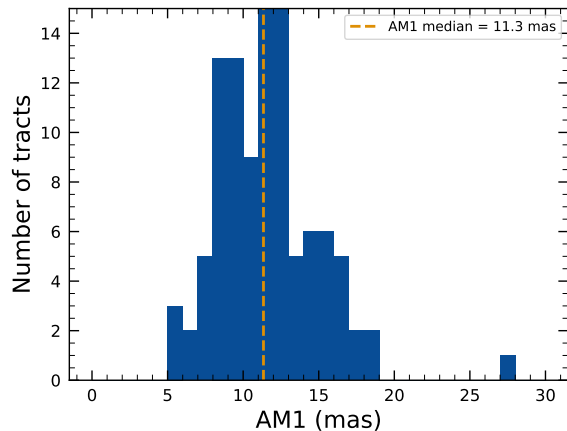


Figure 20. Median per-tract repeatability in separations between isolated point sources 5 arcmin apart in visits across all bands.

2118 field in the two-point correlation function of the residuals (E-mode), P. F. Léget et al. (2021) and W. F. Fortino et al. (2021). However, as seen in Figure 23, the residuals in many visits also have correlation functions with a non-negligible divergence-free B-mode, indicating that some of the remaining residuals are due to unmodeled instrumental effects, such as rotations between visits.

2122
 2123
 2124
 2125
 2126 We can see unmodeled camera distortions by stacking the astrometric residuals over many visits as a function of the focal plane position. Figure 24 shows the median residuals in x and y directions for 1792 visits. Spatial structures are evident at the CCD level, as well as at the mid-line break, the discontinuity between the two rows of amplifiers, in the y -direction residuals. Further stacking all the detectors makes certain effects particularly clear. Figure 25 shows distortions very similar to those measured for an LSSTCam ITL sensor in a laboratory setting in J. H. Esteves et al. (2023).

2140 5.4. Differential Chromatic Refraction

2141
 2142
 2143
 2144
 2145
 2146
 2147
 2148
 2149
 2150
 2151
 2152
 2153 Differential Chromatic Refraction (DCR) occurs when light passes through Earth’s atmosphere, refracting more for shorter wavelengths, which causes blue light to appear shifted closer to the zenith. This wavelength-dependent effect results in the smearing of point sources along the zenith direction, specifically parallel to the parallactic angle. The DCR effect is observable in LSSTComCam data, particularly in the angular offset versus $g-i$ band magnitude difference plots, as shown in Figure 26. These plots contain 228 visits chosen to maximize the range of observed airmass. When looking at data perpendicular to the parallactic angle, sources exhibit no discernible DCR effect, which is expected, and

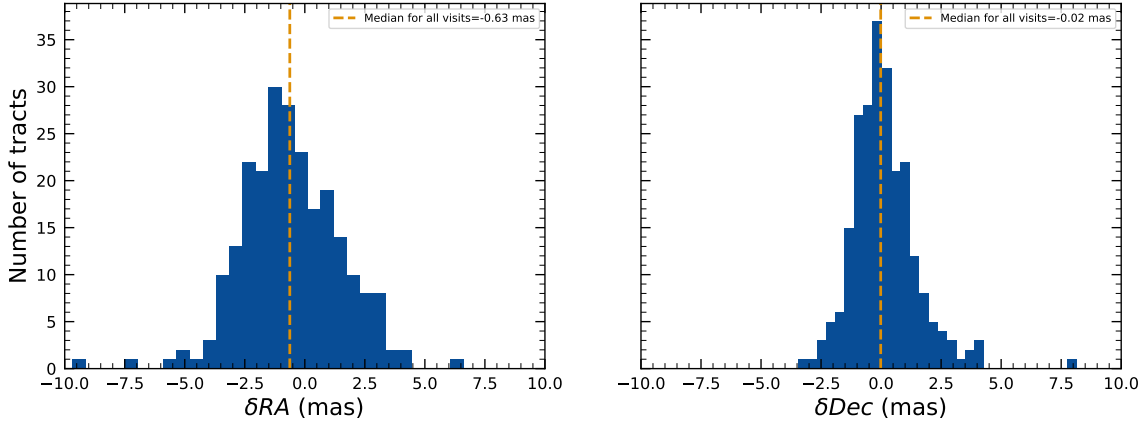


Figure 21. Median absolute offset for all visits in r -band in [tract 4849](#) in the ECDFS field. The offset is the difference between the positions of isolated point sources that were reserved from the astrometric fit and matched objects from the Gaia DR3 catalog.

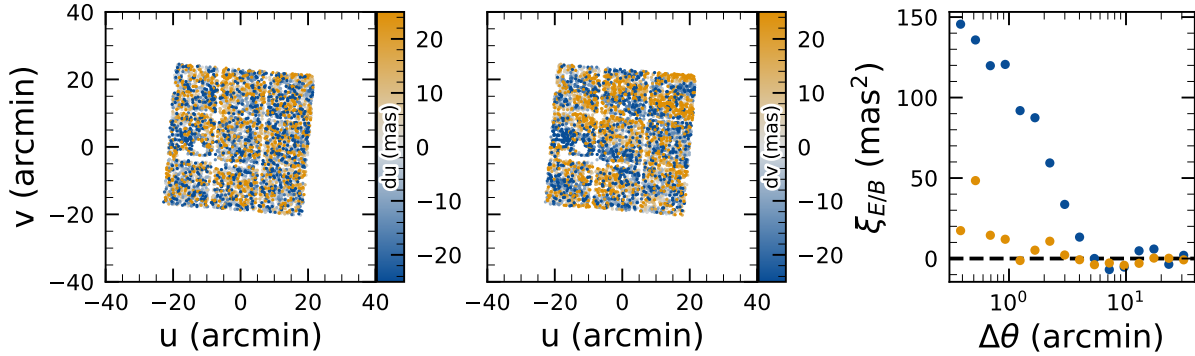


Figure 22. Astrometric residuals in u (left panel) and v (center panel) directions with the E (blue) and B (orange) modes of the two-point correlation function (right panel) seen in visit 2024120200359 in [tract 2393](#) in u band. The residuals show a wave-like pattern characteristic of atmospheric turbulence, and there is significant E-mode and negligible B-mode in the correlation function.

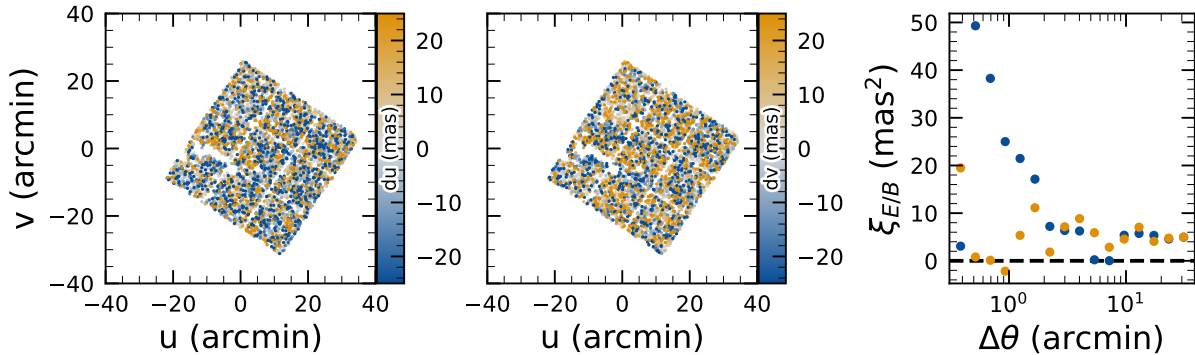


Figure 23. Astrometric residuals in u (left panel) and v (center panel) directions, with the E (blue) and B (orange) modes of the two-point correlation function (right panel) seen in visit 2024120700527 in [tract 2393](#) in u band. There are coherent residuals, but without the wave-like pattern seen in [Figure 22](#), and the correlation function has significant values for both E and B-modes.

2154 form a clear vertical distribution on the two-dimensional 2156
 2155 density plots in [Figure 26](#).

In contrast, sources aligned with the parallactic angle 2156
 2157 exhibit a tilted, linear distribution, clearly demonstrat-

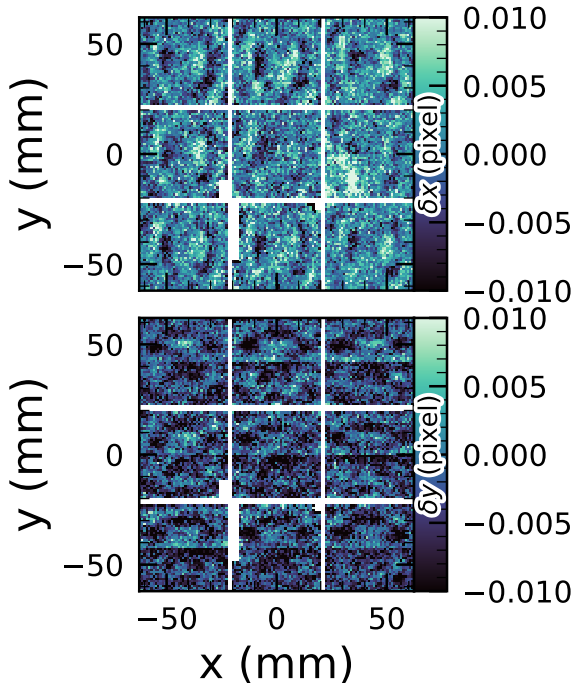


Figure 24. Median astrometric residuals as a function of focal plane position, shown in the left panel for the x direction and in the right panel for the y direction, for all nine *LSSTComCam* CCDs independently. The range of the color scale is ± 0.01 pixels, corresponding to 2 mas, showing that the effect is small.

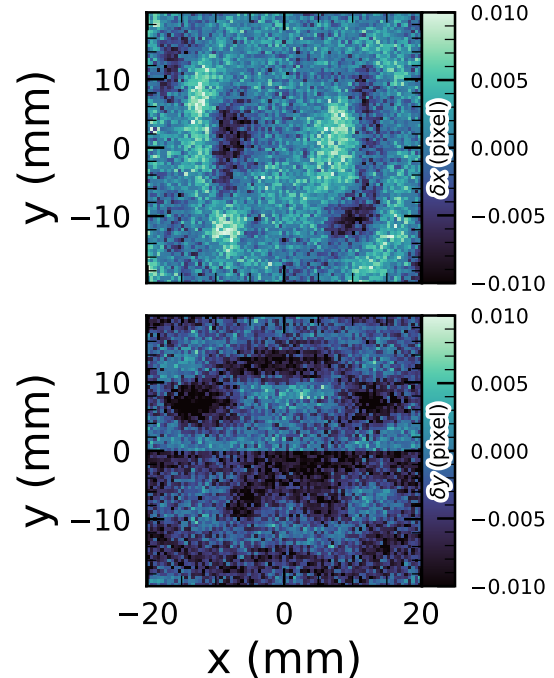


Figure 25. Median residuals as a function of pixel position, shown in the left panel for the x direction and in the right panel for the y direction. These residuals are aggregated across all nine CCDs that comprise the central *LSSTComCam* raft. The range of the color scale is ± 0.01 pixels, corresponding to 2 mas, showing that the effect is small.

2158 ing that the relationship between angular offset and the
 2159 $g-i$ band magnitude difference, thereby providing a visual
 2160 indication of the DCR effect. The DCR effect will
 2161 be addressed in future releases.

2162 5.5. Stellar Photometry

2163 The photometric repeatability for isolated bright un-
 2164 resolved sources following the FGCM fits was excellent.
 2165 For the 10% of unresolved sources withheld from the fit
 2166 and having signal-to-noise ratios greater than 100, the
 2167 photometric repeatability after applying chromatic cor-
 2168 rection was 7.1, 5.4, 5.4, 5.1, 5.9, and 6.5 mmag in the
 2169 $ugrizy$ bands respectively, across all fields. After ac-
 2170 counting for photometric noise, the intrinsic photomet-
 2171 ric repeatability was approximately 4.8, 2.7, 1.7, 1.0, 2.0,
 2172 and 1.1 mmag in $ugrizy$. The DP1 processing does not
 2173 yet include chromatic corrections in the final photomet-
 2174 ry. In this case the delivered photometric repeatability
 2175 was 3–8 mmag for grizy.

2176 In Figure 27, we show the stellar loci for $ugriz$ for un-
 2177 resolved sources in the DP1 Object table (§3.2). These
 2178 unresolved sources were selected using the extendedness
 2179 parameter (§3.2) in the Object catalog. This param-

2180 eter is assigned a value of 0 (unresolved) or 1 (resolved)
 2181 in each band based on the difference between the PSF
 2182 and CModel magnitudes. The extendedness is set to 1
 2183 when this magnitude difference exceeds 0.016 mag, as
 2184 the PSF flux for extended sources is biased low relative
 2185 to the CModel flux. This method has been previously
 2186 employed by the SDSS pipelines, and its statistical prop-
 2187 erties, including the optimal combination of information
 2188 from different bands and repeated measurements, are
 2189 discussed in C. T. Slater et al. (2020).

2190 Figure 28 illustrates the behavior of the extendness
 2191 parameter. Its behavior in the g and r bands is simi-
 2192 lar, with unresolved sources scattered around the ver-
 2193 tical line centered on zero. The width of the distri-
 2194 bution increases towards fainter magnitudes. Resolved
 2195 sources are found to the right and the dashed lines in the
 2196 top panels show the adopted “star-galaxy” separation
 2197 boundary. The morphology of the two color-magnitude
 2198 diagrams in the bottom panels suggest that the un-
 2199 resolved sample suffers from increasing contamination by
 2200 galaxies for $r > 24$. This behavior is consistent with
 2201 simulation-based predictions from C. T. Slater et al.
 2202 (2020).

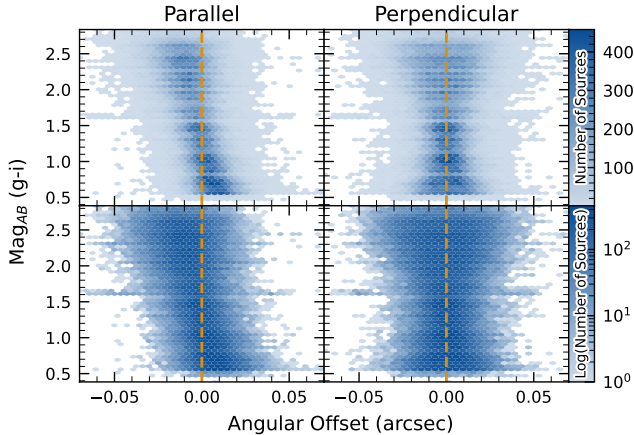


Figure 26. Visualization of [Differential Chromatic Refraction \(DCR\)](#) observed in the [LSSTComCam](#) commissioning campaign. The $g - i$ color is computed for every source in the reference catalog that is matched to a direct source in the science image, and the binned density for the full survey is plotted against the angular offset between the reference and detected positions. The angular offset is projected along coordinates parallel and perpendicular to the parallactic angle of the observation, and shows a characteristic correlation along the parallel axis with no correlation along the perpendicular axis. The orange vertical dashed line indicates the expected $g - i$ magnitude distribution at zero angular offset.

5.6. Detection Completeness on Coadds

We characterize completeness by injecting synthetic sources into coadded images, and by comparing source detections to external catalogs. In both cases, we use a greedy, probabilistic matching algorithm that matches reference objects, in order of descending brightness, to the most likely target within a $0.5''$ radius.

We inject sources in 12 of the patches of the [ECDFS](#) region with the deepest coverage. The input catalog contains stars and galaxies from part of the [Data Challenge 2 \(DC2\)](#) simulations ([LSST Dark Energy Science Collaboration \(LSST DESC\) et al. 2021](#)), where the galaxies consist of an exponential disk and de Vaucouleurs ([G. de Vaucouleurs 1948, 1953](#)) bulge. To avoid deblender failures from excessive increases in object density, stars with a total flux (i.e., summed across all six bands) brighter than 17.5 mag are excluded, as are galaxies whose total flux is brighter than 15 mag or fainter than 26.5 mag. Half of the remaining objects are selected for injection. Afterwards, individual bulge and disk components fainter than 29 mag are also excluded, both for computational expediency and because their structural properties are less likely to be representative of real galaxies.

[Figure 29](#) shows completeness as a function of magnitude for these injected objects in the [ECDFS](#) field. These completeness estimates are comparable to results from matching external catalogs. Matching to the Hubble Legacy Field catalog ([G. Illingworth et al. 2016; K. E. Whitaker et al. 2019](#)) reaches 50% completeness at $F775W = 26.13$, or about $i = 25.83$ from differences in matched object magnitudes. Similarly, completeness drops below 90% at $VIS = 23.80$ from matching to Euclid Q1 ([Euclid Collaboration et al. 2025](#)) objects, equivalent to roughly $i = 23.5$. The Euclid imaging is of comparable or shallower depth, so magnitude limits at lower completeness percentages than 90% are unreliable, whereas the HST images cover too small and irregular of an area to accurately characterize 80-90% completeness limits.

At the 80% completeness limit, nearly 20% of objects, primarily injected galaxies, are incorrectly classified as stars based on their reference band extendedness. Similarly, the fraction of correctly classified injected stars drops to about 50% at $i = 23.8$ (corresponding to 90% completeness).

This analysis has several caveats. The selection of objects for matching in any catalog is not trivial. Some fraction of the detections are spurious, particularly close to bright stars and their diffraction spikes. Additionally, some objects lie in masked regions of one survey but not another, which has not been accounted for. For injected source matching, the reference catalog does not include real on-sky objects. Based on prior analyses of the [DC2](#) simulations, purity is generally greater than completeness at any given magnitude. Similarly, for bright ($i < 23$) objects classified as stars by reference band extendedness, $< 5\%$ are either unmatched to a Euclid or HST object, or misclassified - that is, selecting on extendedness alone yields a fairly pure but incomplete sample of stars. We expect to remedy some of these shortcomings in future releases.

5.7. Model Flux and Shape Measurement

[Figure 30](#) shows i -band magnitude residuals for CModel and Sérsic measurements using the matched injected galaxies described in [§5.6](#). Similar behavior is seen in other bands. Sérsic fluxes show reduced scatter for galaxies with $i < 22.5$, though CModel fluxes are less biased, with median residuals closer to zero and less magnitude-dependent. For fainter objects, Sérsic fluxes are more biased and less accurate. The magnitude of this bias is considerably larger than previously seen in simulated data. Subsequent testing indicates that this bias can be (roughly) halved by fitting an exponential model first, and then using those parameters to initialize

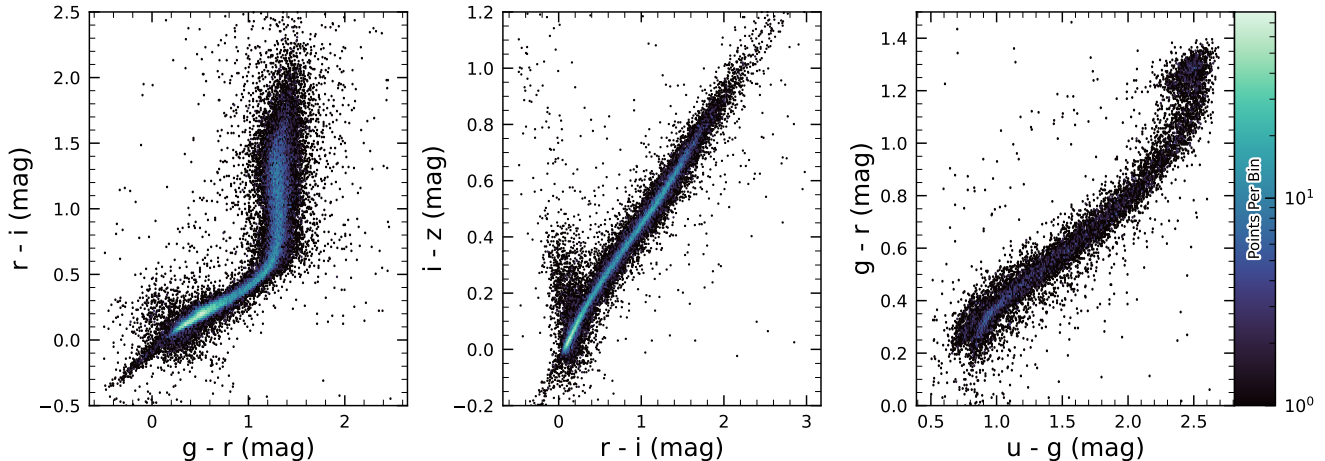


Figure 27. Examples of stellar loci for unresolved sources from the DP1 dataset. From left to right: gri stellar locus containing 63,236 stars with signal-to-noise ratio > 200 in the i band; riz stellar locus containing 46,760 stars with signal-to-noise ratio > 200 in the i band; ugr stellar locus containing 12,779 stars with signal-to-noise ratio > 50 in the u band.

a free Sérsic fit. This approach will be adopted in future releases. Aperture fluxes - including Kron and GAaP - are not shown as they are not corrected to yield total fluxes. The correction for Kron fluxes can be derived from the Sérsic index (A. W. Graham & S. P. Driver 2005), but this correction is not provided in object tables.

Figure 31 shows $g - i$ color residuals versus r -band magnitude for the same sample of galaxies as Figure 30. For this and most other colors, GAaP (with a $1''$ aperture) and Sérsic colors both yield lower scatter; however, the CModel colors have the smallest bias. Curiously, the GAaP bias appears to be magnitude-dependent, whereas the Sérsic bias remains stable from $19 < r < 26$. Any of these color measurements are suitable for use for deriving quantities like photometric redshifts, stellar population parameters, etc.

In addition to photometry, some algorithms include measurements of structural parameters like size, ellipticity, and Sérsic index. One particular known issue is that many (truly) faint objects have significantly overestimated sizes and fluxes. This was also seen in the Dark Energy Survey (K. Bechtol et al. 2025), who dubbed such objects “super-spreaders”. These super-spreaders contribute significantly to overestimated fluxes at the faint end (see e.g. Figure 30), and are particularly problematic for the Kron algorithm (R. G. Kron 1980), which should only be used with caution.

As mentioned in §4.5, the Sérsic fits include a free centroid, which is initialized from the fiducial centroid of the object. Preliminary analyses of matched injected objects suggest that the Sérsic model galaxy astrometry residuals are somewhat smaller than for the stan-

dard centroids used in other measurements, and so users of the Sérsic photometry should also use these centroid values. One caveat is that for faint objects and/or in crowded regions with unreliable deblending, free centroids can drift significantly and potentially towards other objects, so objects with large differences between the fiducial and Sérsic astrometry should be discarded or used with caution.

Sérsic model parameter uncertainties are estimated by computing and inverting the Hessian matrix with the best-fit parameter values, after replacing the pixel data (but not uncertainties) by the best-fit model values. Currently, only the on-diagonal dispersion term (square root of the variance) is provided as an error estimate for each parameter. Future releases may provide more off-diagonal terms of the covariance matrix - particularly for the structural parameters, which are known to be correlated.

A major outstanding issue is that many parameter uncertainties - including but not limited to those for fluxes - are underestimated. This is at least partly (but not wholly) due to the fact that coaddition introduces covariance between pixels, which is not captured in per-pixel variances.

The degree to which uncertainties are underestimated can depend on the parameter in question and on the brightness of the object. In plots of uncertainty-scaled residuals, the ideal behavior is for the median (i.e. the bias) to lie close to zero, and for the $\pm 1\sigma$ lines to lie at ± 1 , without any dependence on magnitude. Figure 32 shows that flux and color uncertainties for PSF model magnitudes of injected stars are both underestimated, but by a factor of approximately $1.7 - 2$ that is not very

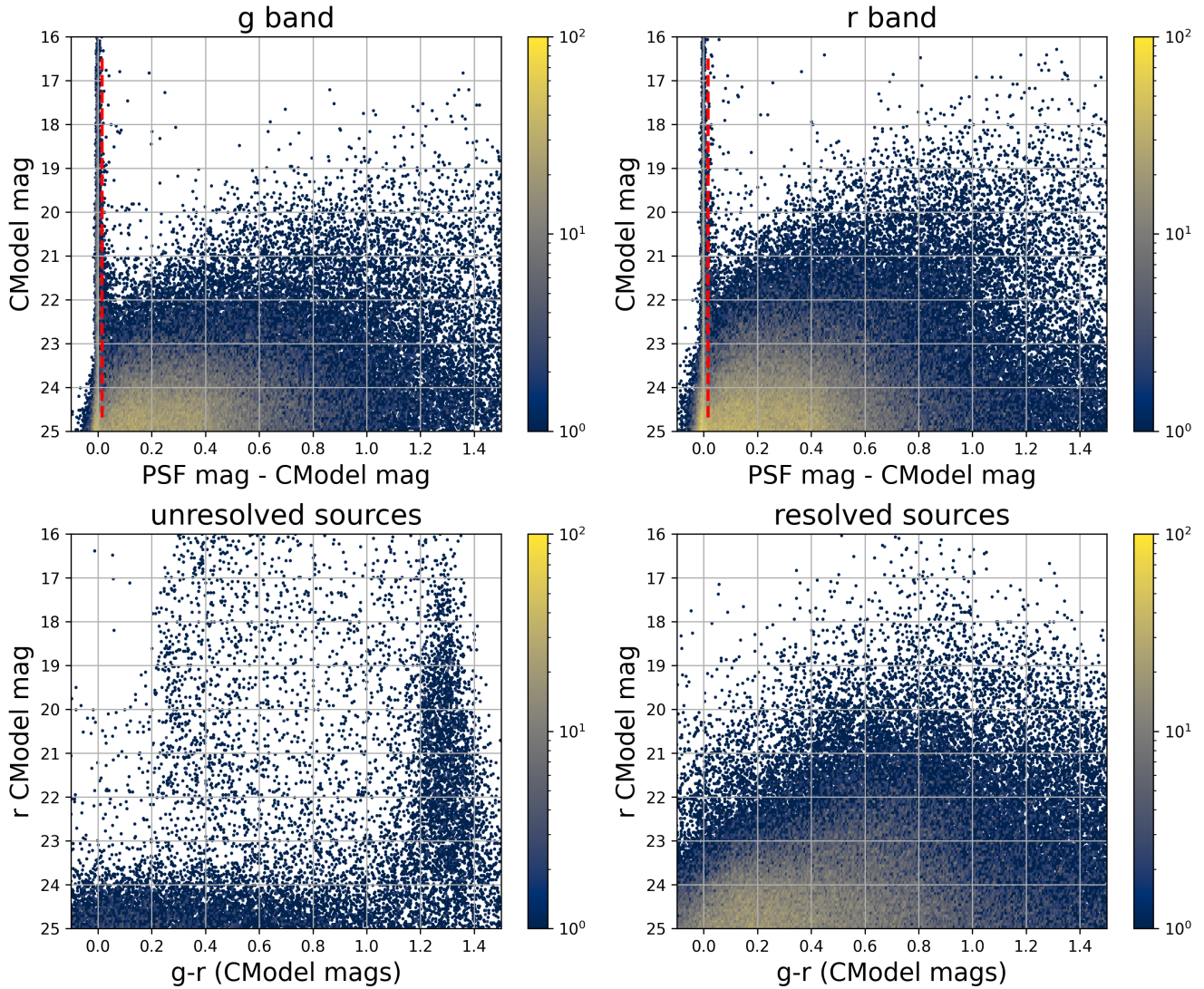


Figure 28. The top two panels shows the difference between the PSF and CModel magnitudes as a function of CModel magnitude in the g and r bands for 178,547 sources with $CModel_r < 25$ from the ECDFS field. The vertical dashed line in each panel marks the minimum value (0.016 mag) for setting the extendedness parameter to 1. The bottom two panels show the r vs. $g - r$ color-magnitude diagrams for 14,701 unresolved (left) and 163,666 resolved (right) sources. Note the unresolved sample suffers from increasing contamination by galaxies for $r > 24$.

2346 sensitive to SNR. This holds for astrometric/centroid
2347 parameters as well.

2348 In turn, Figure 33 shows that CModel color uncertain-
2349 ties of galaxies are underestimated by a similar factor at
2350 the faint end, but with appreciable scaling with mag-
2351 nitude (and thereby SNR). Flux error underestimation
2352 is both larger than for colors and scales more strongly
2353 with SNR. This indicates that systematic effects domi-
2354 nate the errors in fluxes, particularly for bright galaxies.
2355 This is also at least partly but not wholly due to so-
2356 called model inadequacy - that is, the fact that galaxy
2357 models, parametric or otherwise, are insufficiently com-
2358 plex to capture the structure of real galaxies.

2359 Figure 34 shows that Sérsic model fluxes and colors
2360 have similar behavior as CModel, but with a greater
2361 degree of overestimation. This may be partly due to the
2362 fact that Sérsic parameter uncertainties are estimated
2363 along with the free centroid and structural (shape and
2364 Sérsic index) parameters, whereas the forced CModel
2365 fluxes and errors are derived from linear flux fits with a
2366 fixed shape and centroid.

2367 Efforts are underway to investigate and quantify the
2368 origin of uncertainty underestimates and future releases
2369 will, at the least, provide recommendations for mitiga-
2370 tions.

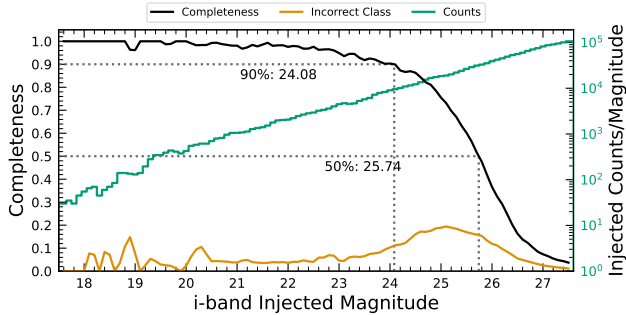


Figure 29. Completeness and incorrect classification fraction as a function of i -band CModel magnitude (Reference Magnitude) for DC2-based injected objects into a portion of the ECDFS field. The “Incorrect Class” line shows the proportion of objects that are matched but classified incorrectly by their reference-band extendedness, i.e. stars with extendedness of 1 or galaxies with extendedness of 0 in the reference band.

5.8. Difference Imaging Purity

We assessed the performance of image differencing using human vetting and source injection (§5.9). Members of the DP1 team labeled more than 9500 DIASource image triplets consisting of cutouts from the science, template, and difference images. We classified these into various real and artifact categories. The raw artifact to real ratio without filtering was roughly 9:1. Bright stars are the main source of artifacts. Correlated noise, primarily in u and g bands, also leads to spurious detections near the flux threshold. We expect to be able to mitigate these effects for LSSTCam.

Applying a reliability threshold improves the purity of transients but not variable stars; technical limitations at the time of model training prevented injection of variable stars into the synthetic training set. Reliability models, described in §4.6.1, for LSSTCam data will be trained on a wider range of input data.

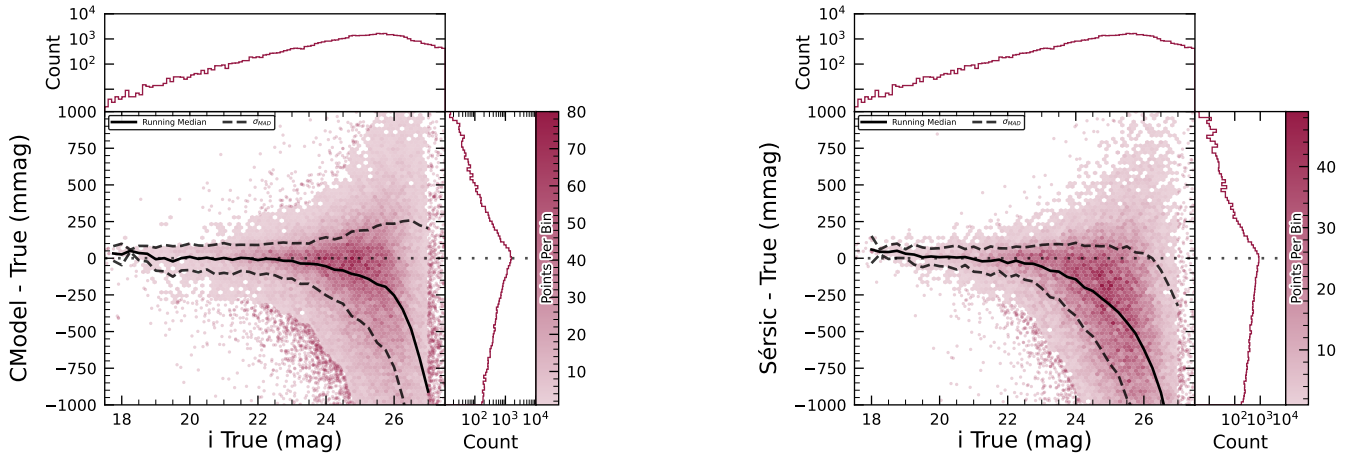
5.9. Difference Imaging Detection Completeness

We assess the performance of our difference imaging pipeline using synthetic source injection on the science images prior to differencing. We construct a catalog of injected sources by joining two different samples of point sources, a set of hosted sources to emulate transients in galaxies and second set of hostless sources. The hosts are selected from the pipeline source catalog that is produced upstream by imposing a cut on their extendedness measurement and selecting $N_{\text{src}} = \min(100, N \times 0.05)$ of the N available sources per detector. For each host we pick a random position angle and radius using its light profile shape to decide where to place the source, and also a random value of brightness for the injected source, with magnitudes higher than the host source.

The hostless sources instead have random positions in the CCD focal plane, and magnitudes chosen from a random uniform distribution with $20 \geq m \geq m_{\text{lim}} + 1$, where m_{lim} is the limiting magnitude of the image. We used the LSST source_injection package¹⁰¹ to include these sources in our test images. We performed a coordinate cross-match task, with a threshold of $0''.5$ to find which of these sources were detected and which were lost, enabling the calculation of a set of performance metrics.

In Figure 35 we show the detection completeness as a function of the SNR, for sources in the ECDFS field, for filters $griz$. We observe a completeness $> 95\%$ for sources with $\text{SNR} > 6$, with mean completeness $\simeq 99\%$ and standard deviation of $\simeq 0.7\%$. In Figure 36 we show the distribution of the residuals of the recovered sky coordinates for the detected synthetic sources. The marginal distributions are both centered at zero, and for sources of $\text{SNR} > 20$ the residuals are compatible with normal distributions $\mathcal{N}(\mu = 0, \sigma^2 = (0''.02)^2)$. In Figure 37 we show photometry results for our detected synthetic sources in the i filter, using PSF photometry on the difference images. We include both the magnitude residuals as well as the flux pulls, defined as $f_{\text{PSF}} - f_{\text{True}} / \sigma_{f_{\text{PSF}}}$ for PSF flux f_{PSF} and error $\sigma_{f_{\text{PSF}}}$, as a function of the true magnitude of the synthetic sources, including the running median and median absolute deviation (MAD) for the whole brightness range. We also include the true magnitude distribution as well as the detection completeness on the top panel, and for reference the 90% and 50% completeness magnitude values in vertical lines. On the right panels we include the marginal distribution for sources brighter than $\text{mag} < 22.5$, splitting the data into hosted and hostless, as well as the robust mean and standard deviation. From this figure we can see that our flux measurements are accurate within a wide range of magnitudes, for both hosted and hostless synthetic sources. We find that the median offset is below 0.002 mag for true magnitudes below 21, and with a maximum σ_{MAD} scatter of about 0.02 mag in this range. For true $m_i < 22.5$, the robust running median PSF magnitude residuals are < 0.02 mag, and when splitting into hosted and hostless both robust median are well below 0.01, and robust σ , i.e. σ_{MAD} are also well below 0.05. For all sources with $m_i < 21.5$ the running median is always $|\langle \delta \rangle| < 0.1$, and $\text{MAD } \sigma_\delta < 1$. Extending to sources with $m_i < 22.5$ then hostless sources have a robust mean pull below 0.02, with a robust standard deviation < 1.15 , while these

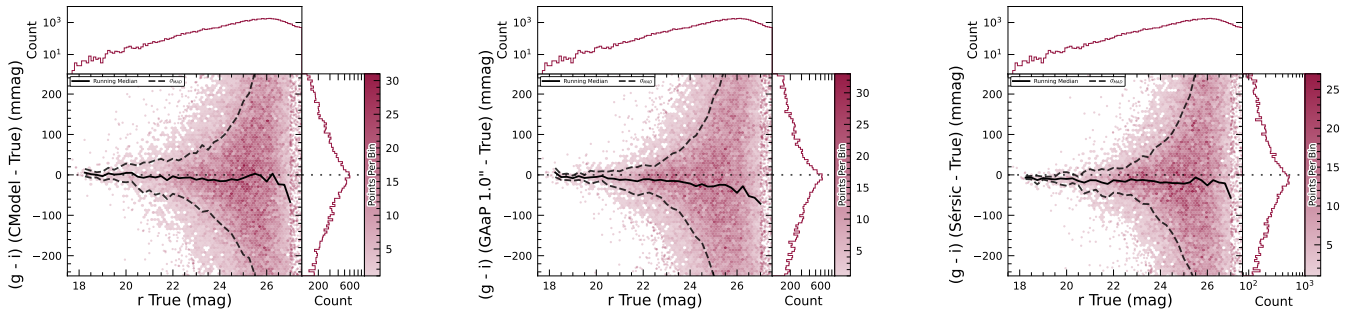
¹⁰¹ <https://pipelines.lsst.io/modules/lsst.source.injection/index.html>



(a) i -band magnitude residuals for CModel measurements of injected galaxies.

(b) i -band magnitude residuals for Sérsic model measurements of injected galaxies.

Figure 30. i -band magnitude residuals for matched injected DC2 galaxies with the CModel and Sérsic algorithms in a portion of the ECDFS region, including the median and scatter thereof. The black line is the median.



(a) $g-i$ color residuals for CModel measurements of injected galaxies.

(b) $g-i$ color residuals for GAaP measurements of injected galaxies.

(c) $g-i$ color residuals for Sérsic model measurements of injected galaxies.

Figure 31. $g-i$ color residuals versus true r -band magnitude for matched injected DC2 galaxies with the CModel, GAaP and Sérsic algorithms in a portion of the ECDFS region.

2455 parameters increase to 0.2 and 1.2 for hosted sources, 2473
 2456 suggesting that we might have contamination from host 2474
 2457 background sources potentially biasing our fluxes. 2475

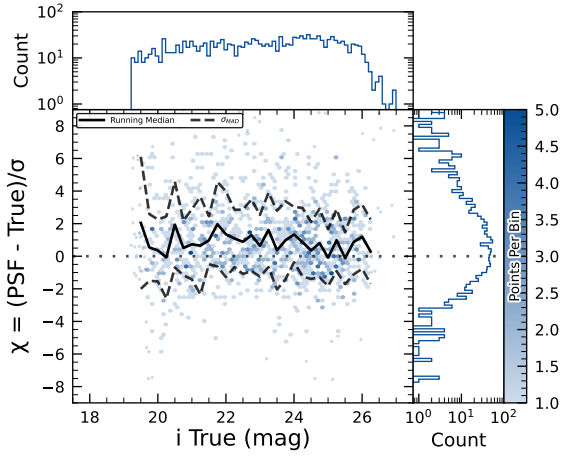
2459 5.10. Solar System

2460 5.10.1. Asteroid Linking Performance

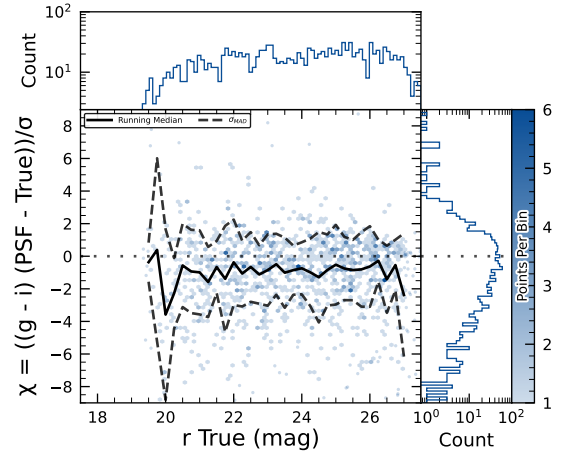
2461 The evaluation of asteroid linking performance in DP1 2476
 2462 focused on demonstrating discovery capability. The solar 2477
 2463 system discovery pipeline produced 269,581 tracklets, 5,691 2478
 2464 linkages, and 281 post-processed candidates. 2479

2465 As described in §4.6.3, post-processing of the heli- 2480
 2466 olinc output with link_purify produced a final set of 281 2481
 2467 candidate linkages, ranked with the most promising 2482
 2468 first. We then used find_orb (B. Gray 2025) to derive 2483
 2469 orbit fits for each candidate, sorting the resulting list by 2484
 2470 χ^2_{dof} , a measure of fit quality. A conservative manual 2485
 2471 investigation of these candidates yielded a curated 2486
 2472 list of 93 probable new asteroid discoveries. Manual 2487
 2488
 2489
 2490

inspection of the linkages indicated that those ranked 2473
 0–137 corresponded to unique real asteroids; ranks 138– 2474
 200 contained additional real objects intermixed with 2475
 some spurious linkages; and ranks higher than 200 were 2476
 essentially all spurious. This analysis indicates that it 2477
 will be possible to identify cuts on quality metrics such 2478
 as χ^2 to define discovery candidate samples with high 2479
 purity; determining the exact quantitative cut values re- 2480
 quires more data with LSSTCam. We next removed all 2481
 observations matched to known asteroids (using Minor 2482
 Planet Center (MPC)’s MPCChecker service), reducing 2483
 the number of candidates to 97. Of these, four had 2484
 strong astrometric and/or photometric outliers, likely 2485
 due to self-subtraction in difference images due to the 2486
 unavoidable limitations of template generation from the 2487
 limited quantity of data available from LSSTComCam. 2488
 We suspect these four linkages do correspond to real ob- 2489
 jects, but have chosen to discard them out of an abun- 2490

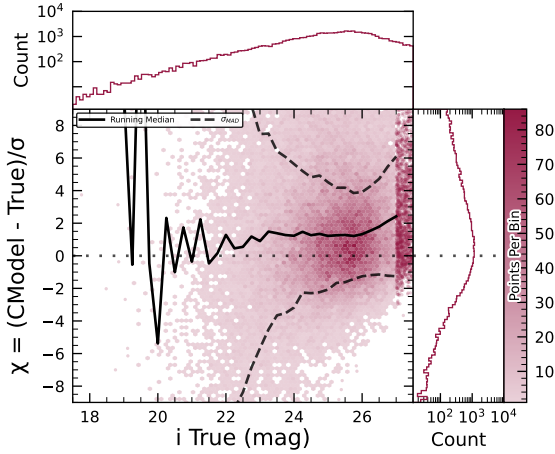


(a) i -band flux uncertainty-scaled residuals for PSF model measurements of injected stars.

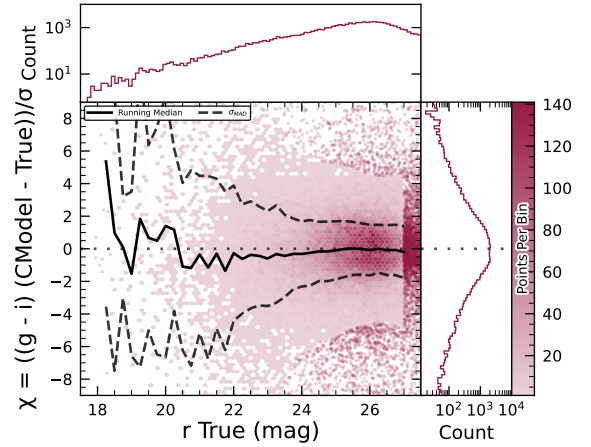


(b) $g - i$ color uncertainty-scaled residuals for PSF model measurements of injected stars.

Figure 32. Color and flux uncertainty-scaled residuals for matched injected DC2 stars' PSF model measurements in a portion of the ECDFS region.



(a) i -band flux uncertainty-scaled residuals for CModel measurements of injected galaxies.



(b) $g - i$ color uncertainty-scaled residuals for CModel measurements of injected galaxies.

Figure 33. Color and flux uncertainty-scaled residuals for matched injected DC2 galaxies' CModel measurements in a portion of the ECDFS region.

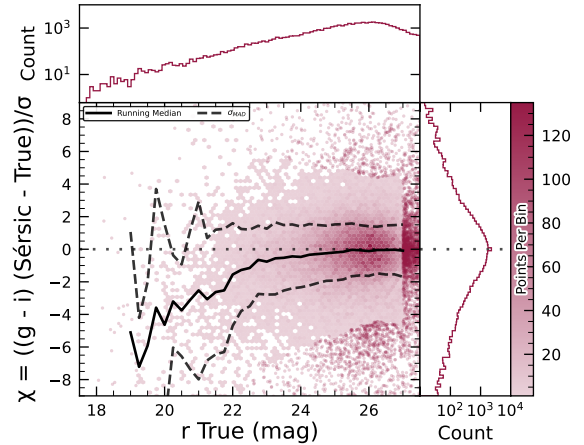
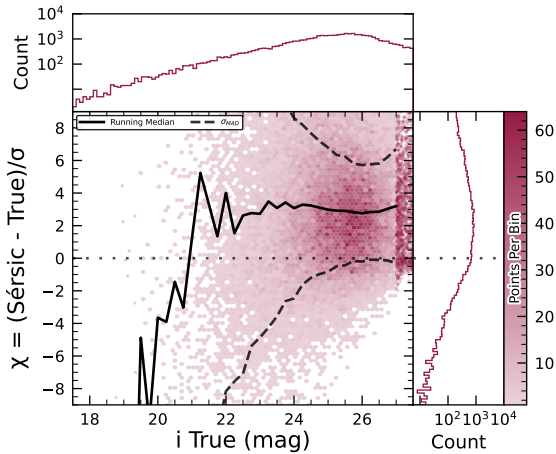
2491 dance of caution. The remaining 93 were submitted to
 2492 the Minor Planet Center and accepted as discoveries,
 2493 demonstrating the LSST pipelines are able to success-
 2494 fully discover new solar system objects.

2495 5.10.2. Asteroid Association Performance

2496 During the Solar System association step, 5988 *Dia-*
 2497 *sources* were linked to 431 unique Solar System ob-
 2498 jects. These include 3,934 *DiaSources* with 338 pre-
 2499 viously known objects cataloged by the MPC, and 2,054
 2500 *DiaSources* with the 93 newly-discovered objects. An
 2501 additional 143 detections of these newly discovered ob-
 2502 jects were also recovered. These detections were not
 2503 initially identified by the discovery pipelines, as they

2504 did not meet the required criteria for tracklet formation,
 2505 specifically the minimum number of detections and/or
 2506 the maximum allowed time span between observations.

2507 The astrometric residuals of known asteroid associa-
 2508 tions are shown in Figure 38. The astrometric precision
 2509 for solar system sources is excellent, with the majority
 2510 of objects detected within $0''.1$ of their expected po-
 2511 sitions. Taking the signed median residuals to search for
 2512 biases, we find that previously-known objects have mean
 2513 residuals of $0''.001$ and $-0''.016$ in the RA and Dec direc-
 2514 tions respectively, while newly-discovered objects have
 2515 mean residuals of $-0''.035$ and $-0''.010$ in the RA and
 2516 Dec directions, respectively. These mean residuals are
 2517 small enough to eliminate the possibility of a timing off-



(a) *i*-band flux uncertainty-scaled residuals for Sérsic model measurements of injected galaxies.

(b) *g*–*i* color uncertainty-scaled residuals for Sérsic model measurements of injected galaxies.

Figure 34. Color and flux uncertainty-scaled residuals for matched injected DC2 galaxies’ Sérsic measurements in a portion of the ECDFS region.

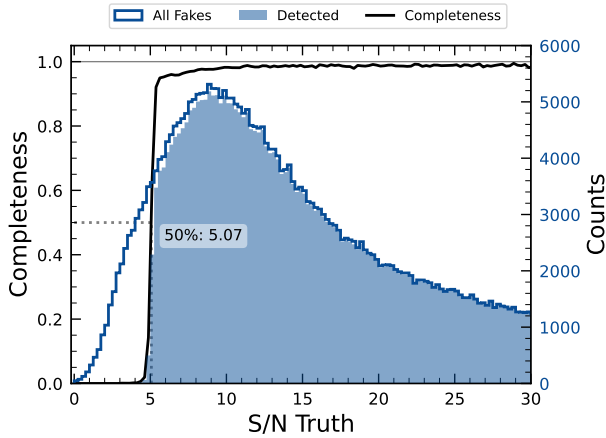


Figure 35. The difference image detection completeness for injected sources in the ECDFS field, for filters *griz*, as a function of the estimated signal to noise ratio SNR. This completeness is the ratio between the found fake sources (shaded histogram) and all the sources (solid line). The horizontal dashed line represents where the 50% completeness level is reached, at approximately SNR \simeq 5.07.

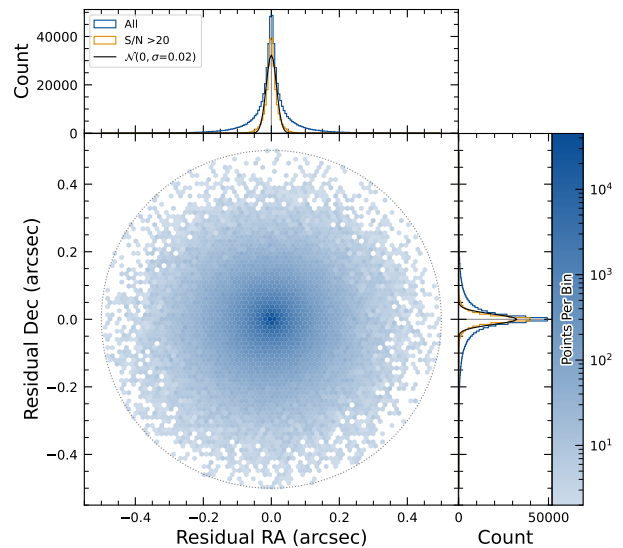


Figure 36. Coordinate residuals for detected synthetic sources in difference images, between recovered and true position of the sources in the ECDFS field. In the top and right panels we include the distribution of these offsets, for all sources as well as for sources with SNR > 20. These high SNR sources show gaussian coordinate residual distributions with $\sigma = 0''.02$ (black solid lines). The circle reflects the matching radius of $0''.5$.

2518 set greater than the second-scale shutter motion, which
 2519 is consistent with the timing studies presented in Section 2.2.2.
 2520

2521 *5.11. Crowded Fields*

2522 Among the seven Rubin DP1 target fields, two stand
 2523 out for their severe stellar crowding: the globular cluster
 2524 47 Tucanae (47_Tuc) and the Fornax dwarf spheroidal
 2525 galaxy (Fornax dSph). These fields were selected in part
 2526 to stress-test the LSST Science Pipelines under high-
 2527 density conditions. While both exhibit high stellar den-

2528 sities, the nature and spatial extent of the crowding differ
 2529 significantly.

2530 47 Tuc presents extreme crowding across much of the
 2531 field, encompassing its dense core and the eastern regions
 2532 influenced by the Small Magellanic Cloud (SMC).

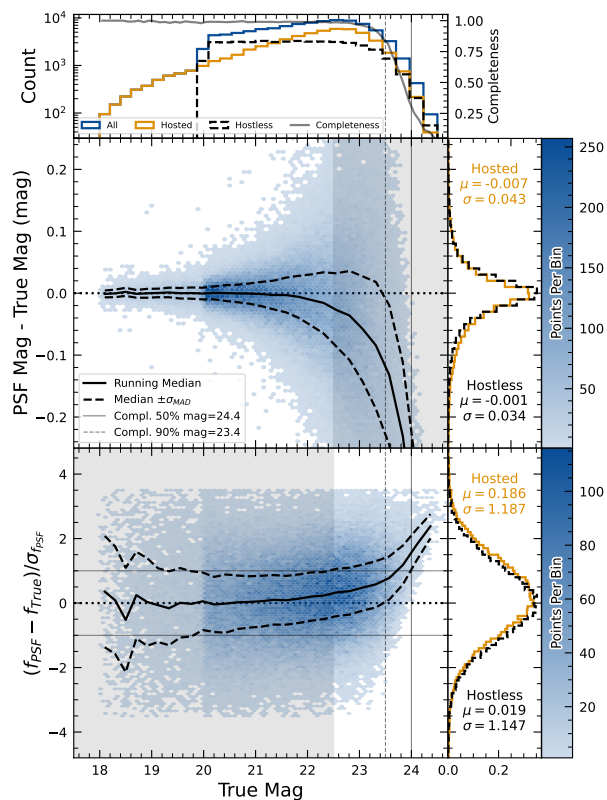


Figure 37. Magnitude residuals and flux pulls for i -band PSF photometry on difference images for ECDFS field in i for detected injected sources. Top panel: Distribution of true magnitudes for injected sources (blue), and split into hostless (black dash) and hosted (orange) sources, with detection completeness as a function of true magnitude (gray line). Vertical dashed lines indicate the 90% and 50% completeness limits. Center left panel: 2D hexbin plot of PSF magnitude residuals (measured minus true) versus true magnitude for detected sources, with running median (solid black) and σ_{MAD} (dashed black) overlaid. Center right panel: Marginalized distributions of PSF magnitude residuals for hostless (blue) and hosted (orange) sources with true magnitude $m_i < 22.5$, annotated with robust mean and standard deviation. Bottom left panel: 2D hexbin plot of PSF flux pulls versus true magnitude for detected sources, with running median (solid black) and σ_{MAD} (dashed black) overlaid. Bottom right panel: Marginalized distributions of PSF flux pulls for hostless (blue) and hosted (orange) sources with true magnitude $m_i < 22.5$, annotated with robust mean and standard deviation.

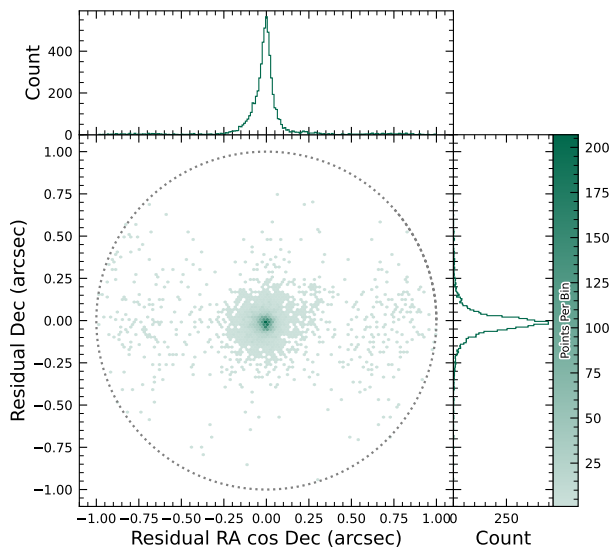


Figure 38. Astrometric residuals between expected and observed positions of Solar System Objects in DP1. The median residuals are $0''.001$ and $-0''.016$ in R.A./Dec direction, with standard deviations of $0''.19$ and $0''.10$, respectively. No detectable systematic offset from zero indicates there are no major errors in either timing or astrometry delivered by the Rubin system. The wider scatter in the RA direction is due to objects whose measured orbital elements are less well constrained, translating to larger along-track positional errors in the predicted positions.

This pervasive crowding leads to persistent challenges for deblending and reliable source detection, exposing field-wide limitations in the current pipeline performance (Y. Choi et al. 2025). In contrast, Fornax dSph shows significant crowding only in its central region, with outer areas remaining well resolved and easier to process.

In both 47Tuc and Fornax, extreme crowding led to the deblending step being skipped frequently when memory or runtime limits were exceeded, typically due to an excessive number of peaks, or large parent footprints. However, the impact of these limitations differed: in 47Tuc, deblending was often skipped across the entire field, resulting in large gaps and substantially reduced completeness. In Fornax, these issues were largely confined to the central region, with much better recovery in the outskirts. This contrast highlights how the pipeline's limitations depend on the spatial extent of high-density regions: 47Tuc exposed systematic, field-wide challenges, whereas Fornax revealed more localized, density-driven limits.

2554 T. M. Wainer et al. (2025) explored the Rubin DP1
 2555 DiaObject catalog (§3.2) in the 47 Tuc field, which con-
 2556 tains sources detected in difference images. Because
 2557 forced photometry is performed at these positions across
 2558 all single-epoch images, this dataset bypasses the coadd-
 2559 based detection and deblending stages that often fail
 2560 in crowded regions. By computing the median of the
 2561 forced photometry for each DiaObject across available
 2562 visits, they recovered approximately three times more
 2563 candidate cluster members than found in the standard
 2564 Object table (Y. Choi et al. 2025). This result un-
 2565 derlines the value of difference-imaging-based catalogs
 2566 for probing dense stellar regions inaccessible to standard
 2567 coadd processing in DP1.

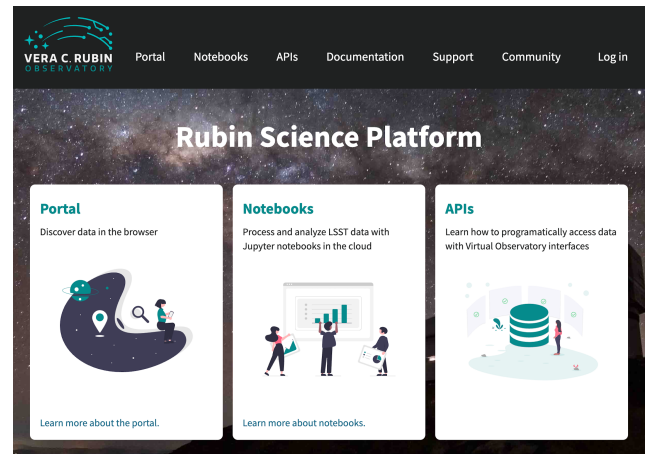
2568 Although the DP1 pipeline was not optimized for
 2569 crowded-field photometry, these early studies of 47 Tuc
 2570 and Fornax provide critical benchmarks. They highlight
 2571 both the limitations and opportunities for science with
 2572 Rubin data in crowded environments, and they inform
 2573 future pipeline development aimed at robust source re-
 2574 covery in complex stellar fields.

2575 6. RUBIN SCIENCE PLATFORM

2576 The RSP (M. Jurić et al. 2019) is a powerful, cloud-
 2577 based environment for scientific research and analysis
 2578 of petascale-scale astronomical survey data. It serves
 2579 as the primary interface for scientists to access, visual-
 2580 ize, and conduct next-to-the-data analysis of Rubin and
 2581 LSST data. The RSP is designed around a “bring the
 2582 compute to the data” principle, eliminating the need for
 2583 users to download massive datasets. Although DP1 is
 2584 much smaller in size (3.5 TB) than many current sur-
 2585 vey datasets, future LSST datasets will be far larger and
 2586 more complex, making it crucial to co-locate data and
 2587 analysis for effective scientific discovery.

2588 The RSP provides users with access to data and
 2589 services through three distinct user-facing Aspects: a
 2590 Portal, which facilitates interactive exploration of the
 2591 data; a JupyterLab-based Notebook environment for
 2592 data analysis using Python; and an extensive set of
 2593 Application Programming Interfaces (APIs) that enable
 2594 programmatic access to both data and services. The
 2595 three Aspects are designed to be fully integrated, en-
 2596 abling seamless workflows across the RSP. The data
 2597 products described in §3 are accessible via all three
 2598 Aspects, and the system facilitates operations such as
 2599 starting a query in one Aspect and retrieving its results
 2600 in another. Figure 39 shows the Rubin Science Platform
 2602 landing page in the Google cloud.

2603 The RSP is supported by a number of back-end ser-
 2604 vices, including databases, files, and batch comput-



2605 **Figure 39.** The Rubin Science Platform landing page at
 2606 <https://data.lsst.cloud/> showing the three user-facing As-
 2607 pects as well as links to documentation and support infor-
 2608 mation.

2609 ing. Support for collaborative work through shared
 2610 workspaces is also included in the RSP.

2611 A preview of the RSP was launched on Google Cloud
 2612 in 2022, operating under a shared-risk model to support
 2613 Data Preview 0 (W. O’Mullane et al. 2024a). This al-
 2614 lowed the community to test the platform, begin prepa-
 2615 rations for science, and provide valuable feedback to in-
 2616 form ongoing development. It was the first time an as-
 2617 tronomical research environment was hosted in a cloud
 2618 environment. The DP1 release brings major updates to
 2619 RSP services, enhancing scientific analysis capabilities.
 2620 The RSP remains under active development, with incre-
 2621 mental improvements being rolled out as they mature.
 2622 During the Rubin Early Science Phase, the RSP will
 2623 continue to operate under a shared-risk model. This
 2624 section outlines the RSP functionality available at the
 2625 time of the DP1 release and provides an overview of
 2626 planned future capabilities.

2627 6.1. Rubin Data Access Center

2628 The Rubin US Data Access Center (US DAC) utilizes
 2629 a novel hybrid on-premises-cloud architecture, which
 2630 combines on-premises infrastructure at the USDF at
 2631 SLAC with flexible and scalable resources in the Google
 2632 cloud. This architecture has been deployed and tested
 2633 using the larger simulated data set of DP0.2 (W.
 2634 O’Mullane et al. 2024b).

2635 In this hybrid model, user-facing services are deployed
 2636 in the cloud to support dynamic scaling in response to
 2637 user demand and to simplify the provisioning and man-
 2638 agement of large numbers of science user accounts. The
 2639 majority of the static data products described in §3 are
 2640 stored on-premises at the USDF to benefit from cost-
 2641 effective mass storage and close integration with Ru-

bin data processing infrastructure, also located at the USDF. For imaging data, the Data Butler (§6.2.2) provides the interface between the cloud-based users and data services, and the on-premises data. For catalog data, a cloud-based TAP client (§6.2.1) submits queries to the on-premises Qserv database cluster (§6.5) and retrieves the results. In the initial DP1 deployment, catalog data is hosted at the USDF while image data is stored in the cloud. The full hybrid model will be rolled out and further tested following the release of DP1. The RSP features a single-sign-on authentication and authorization system to provide secure access for Rubin data rights holders (R. Blum & the Rubin Operations Team 2020).

6.2. API Aspect

The API Aspect provides a comprehensive set of user-facing interfaces for programmatic access to the DP1 data products, through both IVOA-compliant services and the Rubin Data Butler. IVOA services enable standard queries and integration with existing tools, while the Butler facilitates advanced data processing within the LSST Science Pipelines.

At the time of the DP1 release, some IVOA services are unavailable, and certain data products are only accessible via the Butler. This section provides an overview of the available IVOA services and Butler access.

6.2.1. IVOA Services

Rubin has adopted a Virtual Observatory (VO)-first design philosophy, prioritizing compliance with IVOA standard interfaces to foster interoperability, standardization, and collaboration. In cases where standardized protocols have yet to be established, additional services have been introduced to complement these efforts. This approach ensures that the RSP can be seamlessly integrated with community-standard tools such as Tool for Operations on Catalogues And Tables (TOPCAT) (M. Taylor 2011) and Aladin (F. Bonnarel et al. 2000; T. Boch & P. Fernique 2014; M. Baumann et al. 2022), as well as libraries such as PyVO (M. Graham et al. 2014).

The user-facing APIs are also used internally within the RSP, creating a unified design that ensures consistent and reproducible workflows across all three Aspects. This reduces code duplication, simplifies maintenance, and ensures all users, both internal and external, access data in the same way. For example, an Astronomical Data Query Language (IVOA standard) (ADQL) query on the Object catalog via TAP yields identical results whether run from the Portal, Notebook, or an external client.

The following IVOA services are available at the time of the DP1 release:

- **Table Access Protocol (TAP) Service:** A TAP service (P. Dowler et al. 2019) enables queries of catalog data via the IVOA-standard ADQL, a dialect of SQL92 with spherical geometry extensions. The main TAP service for DP1 runs on the Rubin-developed Qserv database (§ 6.5), which hosts the core science tables described in §3.2, as well as the Visit database. It also provides image metadata in the IVOA ObsCore format via the standard `ivoa.ObsCore` table, making it an “ObsTAP” service (ObsTAP; M. Louys et al. 2017). The TAP service is based on the Canadian Astronomy Data Centre (CADC)’s open-source Java TAP implementation¹⁰², modified for the exact query language accepted by Qserv. It currently supports a large subset of ADQL, with limitations documented in the data release materials (see §7.1) and exposed via the TAP **capabilities** endpoint where possible.

The TAP service provides metadata annotations consistent with the standard, including table and column descriptions, indications of foreign-key relationships between tables, and column metadata such as units and IVOA Unified Content Descriptors (UCDs).

- **Image Access Services:** Rubin image access services are compliant with IVOA SIAv2 (Simple Image Access Protocol, version 2; T. Jenness et al. 2024; P. Dowler et al. 2015) for discovering and accessing astronomical images based on metadata. SIAv2 is a REpresentational State Transfer (REST)-based protocol designed for the discovery and retrieval of image data. It allows, for instance, querying all images in a given band over a defined sky region and time period.

Users identify an image or observation of interest and query the service. The result set includes metadata about the image, such as the sky position, time, or band, and a data access URL, which includes an IVOA Identifier uniquely identifying the dataset (T. Jenness & G. P. Dubois-Felsmann 2025), allowing the dataset to be retrieved or a cutout requested via Server-side Operations for Data Access (IVOA standard) (SODA).

¹⁰² <https://github.com/opencadc/tap>

- **Image Cutout Service:** The Rubin Cutout Service (R. Allbery 2023, 2024) is based on the IVOA SODA standard (F. Bonnarel et al. 2017). Users submit requests specifying sky coordinates and the cutout size as the radius from the coordinates, and the service performs the operation on the full image and returns a result set. For DP1, the cutout service is a single cutout service only where N cutout requests will require N independent synchronous calls. We expect some form of bulk cutout service by mid 2026.
- **HiPS Data Service:** An authenticated HiPS (P. Fernique et al. 2017) data service for seamless pan-and-zoom access to large-scale co-adds. It supports fast interactive progressive image exploration at a range of resolutions.
- **WebDAV:** A Web Distributed Authoring and Versioning (WebDav) service is provided to enable users to remotely manage, edit, and organize files and directories on the RSP as if they were local files on their own computer. This is especially useful for local development.

6.2.2. Data Butler

The Rubin Data Butler (T. Jenness et al. 2022; N. B. Lust et al. 2023), is a high-level interface designed to facilitate seamless access to data for both users and software systems. This includes managing storage formats, physical locations, data staging, and database mappings. A Butler repository contains two components:

- the *Data Store*: A physical storage system for datasets, e.g., a Portable Operating System Interface (POSIX) file system or S3 object store; and
- the *Registry*: An Structured Query Language (SQL)-compatible database that stores metadata about the datasets in the data store.

For DP1, the Butler repository is hosted in the Google Cloud, using an (Amazon) Simple Storage Service (S3)-compatible store for datasets and AlloyDB, a PostgreSQL-compatible database, for the registry.

In the context of the Butler, a *dataset* refers to a unique data product, such as an image, catalog or map, generated by the observatory or processing pipelines. Datasets belong to one of the various types of data products, described in §3. The Butler ensures that each dataset is uniquely identifiable by a combination of three pieces of information: a data coordinate, a dataset type, and a run collection. For example,

Table 6. Tract coverage of each DP1 field. The size of a tract is larger than the LSSTComCam field of view; however, since each observed field extends across more than one tract, each field covers multiple tracts.

Field Code	Tract ID
47_Tuc	453, 454
ECDFS	4848, 4849, 5062, 5063, 5064
EDFS_comcam	2234, 2235, 2393, 2394
Fornax_dSph	4016, 4017, 4217, 4218
Rubin_SV_095_-25	5305, 5306, 5525, 5526
Rubin_SV_38_7	10221, 10222, 10463, 10464, 10704, 10705
Seagull	7610, 7611, 7849, 7850

a dataset that represents a single raw image in the i band taken on the night starting 2024-11-11 with exposure ID 2024111100074 would be represented as `dataId='exposure':2024111100074, 'band':'i', 'instrument':'LSSTComCam'` and is associated with the `raw` DatasetType. For a deep coadd on a patch of sky in the Seagull field, there would be no exposure dimensions and instead the tract, patch and band would be specified as `dataId='tract':7850, 'patch':6, 'band':'g', 'instrument':'LSSTComCam', skymap='lsst_cells_v1'` and is associated with the `deep_coadd` DatasetType. The tract identification numbers and corresponding target names for these tracts are listed in Table 6.

The data coordinate is used to locate a dataset in multi-dimensional space, where dimensions are defined in terms of scientifically meaningful concepts, such as instrument, visit, detector or band. For example, a calibrated single-visit image (§3.1) has dimensions including band, instrument, and detector. In contrast, the visit table (§3.2), a catalog of all calibrated single-epoch visits in DP1, has only the instrument dimension. The main dimensions used in DP1 are listed, together with a brief description, in Table 7. To determine which dimensions are relevant for a specific dataset, the Butler defines dataset types, which associate each dataset with its specific set of relevant dimensions, as well as the associated Python type representing the dataset. The dataset type defines the kind of data a dataset represents, such as a raw image (`raw`), a processed catalog (`object_forced_source`), or a sky map (`skyMap`). Table 8 lists all the dataset types available via the Butler in DP1, together with the dimensions needed to uniquely identify a specific dataset and the number of unique datasets of each type.

Table 7. Descriptions of and valid values for the key data dimensions in DP1. YYYYMMDD signifies date and # signifies a single 0–9 digit.

Dimension	Format/Valid values	Description
day_obs	YYYYMMDD	A day and night of observations that rolls over during daylight hours.
visit	YYYYMMDD####	A sequence of observations processed together; synonymous with “exposure” in DP1.
exposure	YYYYMMDD####	A single exposure of all nine ComCam detectors.
instrument	LSSTComCam	The instrument name.
detector	0–8	A ComCam detector.
skymap	lsst_cells_v1	A set of tracts and patches that subdivide the sky into rectangular regions with simple projections and intentional overlaps.
tract	See Table 6	A large rectangular region of the sky.
patch	0–99	A rectangular region within a tract.
physical_filter	u_02, g_01, i_06, r_03, z_03, y_04	A physical filter.
band	u, g, r, i, z, y	An conceptual astronomical passband.

It is important to highlight a key difference between accessing catalog data via the [TAP](#) service versus the [Butler](#). While the [TAP](#) service contains entire catalogs, many of the same catalogs in the [Butler](#) are split into multiple separate catalogs. This is partly due to how these catalogs are generated, but also because of the way data is stored within and retrieved from the [Butler](#) repository – it is inefficient to retrieve the entire `Source` catalog, for example, from the file system. Instead, because the `Source` catalog contains data for sources detected in the `visit_images`, there is one `Source` catalog in the [Butler](#) for each `visit_image`. Similarly, there is one `Object` catalog for each `deep_coadd`. All the catalogs described in §3.2, aside from the `CcdVisit`, `SSObject`, `SSSource`, and `Calibration` catalogs, are split within the [Butler](#).

A dataset is associated with one or more *Collections*; logical groupings of datasets within the [Butler](#) system that were created or processed together by the same batch operation. Collections allow multiple datasets with the same data coordinate to coexist without conflict. Collections support flexible, parallel processing by enabling repeated analyses of the same input data using different configurations. The [DP1](#) [Butler](#) is read-only; a writeable [Butler](#) is expected by mid-2026.

6.2.3. Remote Programmatic Access

The [Rubin RSP API](#) can be accessed from a local system by data rights holders outside of the [RSP](#), by creating a user security token. This token can then be used as a bearer token for [API](#) calls to the [RSP](#) [TAP](#) service. This capability is especially useful for remote data analysis using tools such as [TOPCAT](#), as well as enabling

third-party systems, e.g., [Community Alert Brokers](#), to access [Rubin](#) data. Additionally, it supports remote development, allowing for more flexible workflows and integration with external systems.

6.3. Portal Aspect

The [Portal Aspect](#) provides an interactive web-based environment for exploratory data discovery, filtering, querying, and visualization of both image and catalog data, without requiring programming expertise. It enables users to access and analyze large datasets via tools for catalog queries, image browsing, time-series inspection, and cross-matching.

The [Portal](#) is built on [Firefly](#) ([X. Wu et al. 2019](#)), a web application framework developed by the [Infrared Processing and Analysis Center \(IPAC\)](#). [Firefly](#) provides interactive capabilities such as customizable table views, image overlays, multi-panel visualizations, and synchronized displays linking catalog and image data.

Designed to support both exploratory data access and detailed scientific investigation, the [Portal](#) delivers an intuitive user experience, allowing users to visually analyze data while retaining access to underlying metadata and query controls.

6.4. Notebook Aspect

The [Notebook Aspect](#) provides an interactive, web-based environment built on [Jupyter Notebooks](#), enabling users to write and execute [Python](#) code directly on [Rubin](#) and [LSST](#) data without downloading it locally. It offers programmatic access to [Rubin](#) and [LSST](#) data products, allowing users to query and retrieve datasets, manipulate and display images, compute derived prop-

Table 8. The name and number of each type of data product in the Butler and the dimensions required to identify a specific dataset.

Data Product	Name in Butler	Required Dimensions	Number in DP1
Image Data Products			
raw	raw	instrument, detector, exposure	16125
visit_image	visit_image	instrument, detector, visit	15972
deep_coadd	deep_coadd	band, skymap, tract, patch	2644
template_coadd	template_coadd	band, skymap, tract, patch	2730
difference_image	difference_image	instrument, detector, visit	15972
Catalog Data Products			
Source	source	instrument, visit	1786
Object	object	skymap, tract	29
ForcedSource	object_forced_source	skymap, tract, patch	636
DiaSource	dia_source	skymap, tract	25
DiaObject	dia_object	skymap, tract	25
ForcedSourceOnDiaObject	dia_object_forced_source	skymap, tract, patch	597
SSSource	ss_source	–	1
SSObject	ss_object	–	1
Visit	visit_table	instrument	1
CCDVisit	visit_detector_table	instrument	1

2881 erities, plot results, and reprocess data using the LSST
 2882 Science Pipelines (§4.1). The environment comes pre-
 2883 installed with the pipelines and a broad set of widely
 2884 used astronomical software tools, supporting immediate
 2885 and flexible data analysis.

2886 6.5. Databases

2887 The user-facing Aspects of the RSP are supported by
 2888 several backend databases that store catalog data prod-
 2889 ucts, image metadata, and other derived datasets. The
 2890 schema for DP1 and other Rubin databases are available
 2891 online at <https://sdm-schemas.lsst.io>.

2892 6.5.1. Qserv

2893 The final 10-year LSST catalog is expected to reach
 2894 15 PB and contain measurements for billions of stars
 2895 and galaxies across trillions of detections. To support
 2896 efficient storage, querying, and analysis of this dataset,
 2897 Rubin Observatory developed Qserv (D. L. Wang et al.
 2898 2011; F. Mueller et al. 2023) – a scalable, parallel, dis-
 2899 tributed SQL database system. Qserv partitions data
 2900 over approximately equal-area regions of the celestial
 2901 sphere, replicates data to ensure resilience and high
 2902 availability, and uses shared scanning to reduce overall
 2903 I/O load. It also supports a package of scientific user-
 2904 defined functions (SciSQL: [https://smonkewitz.github.
 2905 io/scisql/](https://smonkewitz.github.io/scisql/)) simplifying complex queries involving spher-
 2906 ical geometry, statistics, and photometry. Qserv is

2907 built on robust production-quality components, includ-
 2908 ing MariaDB (<https://www.mariadb.org/>) and XRootD
 2909 (<https://xrootd.org/>). Qserv runs at the USDF and user
 2910 access to catalog data is via the TAP service (§6.2.1).
 2911 This enables catalog-based analysis through both the
 2912 RSP Portal and Notebook Aspects.

2913 Although the small DP1 dataset does not require
 2914 Qserv’s full capabilities, we nevertheless chose to use
 2915 it for DP1 to accurately reflect the future data access
 2916 environment and to gain experience with scientifically-
 2917 motivated queries ahead of full-scale deployment. Qserv
 2918 is open-source and available on GitHub: [https://github.
 2919 com/lsst/qserv](https://github.com/lsst/qserv).

2920 7. SUPPORT FOR COMMUNITY SCIENCE

2921 The Rubin Observatory has a science community that
 2922 encompasses thousands of individuals worldwide, with
 2923 a broad range of experience and expertise in astronomy
 2924 in general, and in the analysis of optical imaging data
 2925 specifically.

2926 Rubin’s model to support this diverse community to
 2927 access and analyze DP1 emphasizes self-help via docu-
 2928 mentation and tutorials, and employs an open platform
 2929 for asynchronous issue reporting that enables crowd-
 2930 sourced solutions. These two aspects of community sup-
 2931 port are augmented by virtual engagement activities. In
 2932 addition, Rubin supports its Users Committee to advo-

cate on behalf of the science community, and supports the eight LSST Science Collaborations (§7.6).

All of the resources for scientists that are discussed in this section are discoverable by browsing the For Scientists pages of the Rubin Observatory website¹⁰³.

7.1. Documentation

The data release documentation for DP1¹⁰⁴ provides an overview of the LSSTComCam observations, detailed descriptions of the data products, and a high-level summary of the processing pipelines. Although much of its content overlaps significantly with this paper, the documentation is presented as a searchable, web-based resource built using Sphinx¹⁰⁵, with a focus on enabling scientific use of the data products.

7.2. Tutorials

A suite of tutorials (NSF-DOE Vera C. Rubin Observatory 2021) that demonstrate how to access and analyze DP1 using the RSP accompanies the DP1 release¹⁰⁶. Jupyter Notebook tutorials are available via the “Tutorials” drop-down menu within the Notebook aspect of the RSP. Tutorials for the Portal and API aspects of the RSP can be found in the data release documentation.

These tutorials are designed to be inclusive, accessible, clear, focused, and consistent. Their format and contents follow a set of guidelines (M. L. Graham et al. 2025) that are informed by modern standards in technical writing.

7.3. Community Forum

The venue for all user support is the Rubin Community Forum¹⁰⁷.

Questions about any and all aspects of the Rubin data products, pipelines, and services – including DP1 – should be posted as new topics in the Support category. This includes beginner-level and “how-to” questions, advanced scientific analysis questions, technical bug reports, account and data access issues, and everything in between. The Support category of the Forum is monitored by Rubin staff, who follow an established internal workflow for following-up and resolving all reported issues.

The Rubin Community Forum is built on the open-source Discourse platform. It was chosen because, for

a worldwide community of ten thousand Rubin users, a traditional (i.e., closed) help desk represents a risk to Rubin science (e.g., many users with the same question having to wait for responses). The open nature of the Forum enables self-help by letting users search for similar issues, and enables crowd-sourced problem solving (and avoids knowledge bottlenecks) by letting users help users.

The Rubin Community Forum, and the internal staff workflows for user support, were set up, tested, and refined with /glsDP0 so that it was ready for use with DP1.

7.4. Engagement Activities

A variety of live virtual and in-person workshops and seminars offer learning opportunities to scientists and students working with the Rubin data products, services, and tools.

- Rubin Science Assemblies (weekly, virtual, 1 hour): alternates between hands-on tutorials based on the most recent data release and open drop-in “office hours” with Rubin staff.
- Rubin Data Academy (annual, virtual, 3-4 days): an intense set of hands-on tutorials based on the most recent data release, along with co-working and networking sessions.
- Rubin Community Workshop (annual, virtual, 5 days), a science-focused conference of contributed posters, talks, and sessions led by members of the Rubin science community and Rubin staff.

Following the release of DP1, all of these engagement activities focused on use of DP1 by the science community. In particular, the 2025 Rubin Data Academy was run the week of the DP1 release, in order to immediately facilitate community access. The 2025 Rubin Community Workshop had several sessions to introduce people to the DP1 dataset and demonstrate how to access and analyze it with the RSP.

For schedules, connection information, zoom recordings, and associated materials, visit the For Scientists pages of the Rubin Observatory website¹⁰⁸. Requests for custom tutorials and presentations for research groups are also accommodated.

7.5. Users Committee

This committee is charged with soliciting feedback from the science community, advocating on their behalf,

¹⁰³ <https://rubinobservatory.org/for-scientists>

¹⁰⁴ <https://dp1.lsst.io>

¹⁰⁵ <https://www.sphinx-doc.org/>

¹⁰⁶ <https://dp1.lsst.io/tutorials>

¹⁰⁷ <https://community.lsst.org/>

¹⁰⁸ <https://rubinobservatory.org/for-scientists/events-deadlines>

and recommending science-driven improvements to the LSST data products and the Rubin Science Platform tools and services. Community members are encouraged to attend their virtual meetings and raise issues to their attention, so they can be included in the committee’s twice-yearly reports to the Rubin Observatory Director.

Like the Forum, the Users Committee was established and began its work with DP0, and that feedback was implemented for DP1. The community’s response to DP1 will be especially valuable input to DP2 and Data Release 1 (DR1), and the Users Committee encourages all users to interact with them. For a list of members and contact information, visit the For Scientists pages of the Rubin Observatory website.

7.6. Science Collaborations

The eight LSST Science Collaborations are independent, worldwide communities of scientists, self-organized into collaborations based on their research interests and expertise. Members work together to apply for funding, build software infrastructure and analysis algorithms, and incorporate external data sets into their LSST-based research.

The Science Collaborations also provide valuable advice to Rubin Observatory on the operational strategies and data products to accomplish specific science goals, and Rubin Observatory supports the collaborations via staff liaisons and regular virtual meetings with Rubin operations leadership.

The Science Collaborations have been functioning for many years, and their engagement and feedback on DP0 was implemented into the community science model for DP1, as it will for future data releases.

8. SUMMARY AND FUTURE RELEASES

Rubin Data Preview 1 offers an initial look at the first on-sky data products and access services from the Vera C. Rubin Observatory. DP1 forms part of Rubin’s Early Science Program, and provides the scientific community with an early opportunity to familiarize themselves with the data formats and access infrastructure for the forthcoming Legacy Survey of Space and Time. This early release has a proprietary period of two years, during which time it is available to Rubin data rights holders only via the cloud-based RSP.

In this paper we have described the completion status of the observatory at the time of data acquisition, the commissioning campaign that forms the basis of DP1, and the processing pipelines used to produce early versions of data products. We provide details on the data products, their characteristics and known issues, and

describe the Rubin Science Platform for access to and analysis of DP1.

The data products described in this paper derive from observations obtained by LSSTComCam. LSSTComCam contains only around 5% the number of CCDs as the full LSST Science Camera (LSSTCam), yet the DP1 dataset that it has produced will already enable a very broad range of science. At 3.5 TB in size, DP1 covers a total area of ~ 15 deg² and contains 1792 single-epoch images, 2644 deep coadded images and 2.3 million distinct astrophysical objects, including 93 new asteroid discoveries.

While some data products anticipated from the LSST are not yet available, e.g., cell-based coadds, DP1 includes several products that will not be provided in future releases. Notably, difference images are included in DP1 as pre-generated products; in future releases, these will instead be generated on demand via dedicated services. The inclusion of pre-generated difference images in DP1 is feasible due to the relatively small size of the dataset, an approach that will not scale to the significantly larger data volumes expected in subsequent releases.

The RSP is continually under development, and new functionality will continue to be deployed incrementally as it becomes available, and independent of the future data release schedule. User query history capabilities, context-aware documentation and a bulk cutout services are just a few of the services currently under development.

Coincident with the release of DP1, Rubin Observatory begins its Science Validation Surveys with the LSST Science Camera. This final commissioning phase will produce a dataset that will form the foundation for the second Rubin Data Preview, DP2. Full operations, marking the start of the LSST, are expected to commence in 2026.

ACKNOWLEDGMENTS

. This material is based upon work supported in part by the National Science Foundation through Cooperative Agreements AST-1258333 and AST-2241526 and Cooperative Support Agreements AST-1202910 and AST-2211468 managed by the Association of Universities for Research in Astronomy (AURA), and the Department of Energy under Contract No. DE-AC02-76SF00515 with the SLAC National Accelerator Laboratory managed by Stanford University. Additional Rubin Observatory funding comes from private donations, grants to universities, and in-kind support from LSST-DA Institutional Members.

3121 This work has been supported by the French Na-
3122 tional Institute of Nuclear and Particle Physics (IN2P3)
3123 through dedicated funding provided by the National
3124 Center for Scientific Research (CNRS).

3125 This work has been supported by STFC fund-
3126 ing for UK participation in LSST, through grant
3127 ST/Y00292X/1.

3128 *Facilities:* Rubin:Simonyi (LSSTComCam), Ru-
3129 bin:USDAC

3130 *Software:* Rubin Data Butler (T. Jenness et al.
3131 2022), LSST Science Pipelines (Rubin Observatory Sci-
3132 ence Pipelines Developers 2025), LSST Feature Based
3133 Scheduler v3.0 (P. Yoachim et al. 2024; E. Naghib et al.
3134 2019) Astropy (Astropy Collaboration et al. 2013, 2018,
3135 2022) PIFF (M. Jarvis et al. 2021), GBDES (G. M.
3136 Bernstein 2022), Qserv (D. L. Wang et al. 2011; F.
3137 Mueller et al. 2023), Slurm, HTCondor, CVMFS, FTS3,
3138 ESNNet

3139

APPENDIX

REFERENCES

- 3140 Abazajian, K., Adelman-McCarthy, J. K., Agüeros, M. A.,
3141 et al. 2004, *AJ*, 128, 502, doi: [10.1086/421365](https://doi.org/10.1086/421365)
- 3142 Ahumada, R., Allende Prieto, C., Almeida, A., et al. 2020,
3143 *ApJS*, 249, 3, doi: [10.3847/1538-4365/ab929e](https://doi.org/10.3847/1538-4365/ab929e)
- 3144 Aihara, H., AlSayyad, Y., Ando, M., et al. 2022, *PASJ*, 74,
3145 247, doi: [10.1093/pasj/psab122](https://doi.org/10.1093/pasj/psab122)
- 3146 Allbery, R. 2023, IVOA SODA implementation experience,
3147 SQuaRE Technical Note SQR-063, NSF-DOE Vera C.
3148 Rubin Observatory. <https://sqr-063.lsst.io/>
- 3149 Allbery, R. 2024, Draft IVOA SODA web service
3150 specification, SQuaRE Technical Note SQR-093,
3151 NSF-DOE Vera C. Rubin Observatory.
3152 <https://sqr-093.lsst.io/>
- 3153 AlSayyad, Y. 2018, Coaddition Artifact Rejection and
3154 CompareWarp, Data Management Technical Note
3155 DMTN-080, NSF-DOE Vera C. Rubin Observatory,
3156 doi: [10.71929/rubin/2583441](https://doi.org/10.71929/rubin/2583441)
- 3157 Ansel, J., Yang, E., He, H., et al. 2024, in 29th ACM
3158 International Conference on Architectural Support for
3159 Programming Languages and Operating Systems, Volume
3160 2 (ASPLOS '24) (ACM), doi: [10.1145/3620665.3640366](https://doi.org/10.1145/3620665.3640366)
- 3161 Antilogus, P., Astier, P., Doherty, P., Guyonnet, A., &
3162 Regnault, N. 2014, *Journal of Instrumentation*, 9,
3163 C03048, doi: [10.1088/1748-0221/9/03/C03048](https://doi.org/10.1088/1748-0221/9/03/C03048)
- 3164 Astropy Collaboration, Robitaille, T. P., Tollerud, E. J.,
3165 et al. 2013, *A&A*, 558, A33,
3166 doi: [10.1051/0004-6361/201322068](https://doi.org/10.1051/0004-6361/201322068)
- 3167 Astropy Collaboration, Price-Whelan, A. M., Sipőcz, B. M.,
3168 et al. 2018, *AJ*, 156, 123, doi: [10.3847/1538-3881/aabc4f](https://doi.org/10.3847/1538-3881/aabc4f)
- 3169 Astropy Collaboration, Price-Whelan, A. M., Lim, P. L.,
3170 et al. 2022, *ApJ*, 935, 167, doi: [10.3847/1538-4357/ac7c74](https://doi.org/10.3847/1538-4357/ac7c74)
- 3171 Baumann, M., Boch, T., Pineau, F.-X., et al. 2022, in
3172 *Astronomical Society of the Pacific Conference Series*,
3173 Vol. 532, *Astronomical Data Analysis Software and*
3174 *Systems XXX*, ed. J. E. Ruiz, F. Pierfederici, &
3175 P. Teuben, 7
- 3176 Bechtol, K., Sevilla-Noarbe, I., Drlica-Wagner, A., et al.
3177 2025, arXiv e-prints, arXiv:2501.05739,
3178 doi: [10.48550/arXiv.2501.05739](https://doi.org/10.48550/arXiv.2501.05739)
- 3179 Berk, A., Anderson, G. P., Bernstein, L. S., et al. 1999, in
3180 *Society of Photo-Optical Instrumentation Engineers*
3181 *(SPIE) Conference Series*, Vol. 3756, *Optical*
3182 *Spectroscopic Techniques and Instrumentation for*
3183 *Atmospheric and Space Research III*, ed. A. M. Larar,
3184 348–353, doi: [10.1117/12.366388](https://doi.org/10.1117/12.366388)
- 3185 Bernstein, G. M. 2022, gbdes: DECam instrumental
3186 signature fitting and processing programs,, *Astrophysics*
3187 *Source Code Library*, record ascl:2210.011
3188 <http://ascl.net/2210.011>
- 3189 Bernstein, G. M., & Jarvis, M. 2002, *AJ*, 123, 583,
3190 doi: [10.1086/338085](https://doi.org/10.1086/338085)
- 3191 Bernstein, G. M., Armstrong, R., Plazas, A. A., et al. 2017,
3192 *PASP*, 129, 074503, doi: [10.1088/1538-3873/aa6c55](https://doi.org/10.1088/1538-3873/aa6c55)
- 3193 Bertin, E. 2011, in *Astronomical Society of the Pacific*
3194 *Conference Series*, Vol. 442, *Astronomical Data Analysis*
3195 *Software and Systems XX*, ed. I. N. Evans,
3196 A. Accomazzi, D. J. Mink, & A. H. Rots, 435
- 3197 Bianco, F. B., Ivezić, Ž., Jones, R. L., et al. 2022, *ApJS*,
3198 258, 1, doi: [10.3847/1538-4365/ac3e72](https://doi.org/10.3847/1538-4365/ac3e72)
- 3199 Blum, R., & the Rubin Operations Team. 2020, Vera C.
3200 Rubin Observatory Data Policy, Data Management
3201 Operations Controlled Document RDO-013, NSF-DOE
3202 Vera C. Rubin Observatory. <https://ls.st/RDO-013>

- 3203 Boch, T., & Fernique, P. 2014, in *Astronomical Society of*
3204 *the Pacific Conference Series*, Vol. 485, *Astronomical*
3205 *Data Analysis Software and Systems XXIII*, ed.
3206 N. Manset & P. Forshay, 277
- 3207 Bonnarel, F., Dowler, P., Demleitner, M., Tody, D., &
3208 Dempsey, J. 2017, *IVOA Server-side Operations for Data*
3209 *Access Version 1.0*, *IVOA Recommendation 17 May 2017*
3210 doi: [10.5479/ADS/bib/2017ivoa.spec.0517B](https://doi.org/10.5479/ADS/bib/2017ivoa.spec.0517B)
- 3211 Bonnarel, F., Fernique, P., Bienaymé, O., et al. 2000,
3212 *A&AS*, 143, 33, doi: [10.1051/aas:2000331](https://doi.org/10.1051/aas:2000331)
- 3213 Bosch, J., Armstrong, R., Bickerton, S., et al. 2018, *PASJ*,
3214 70, S5, doi: [10.1093/pasj/psx080](https://doi.org/10.1093/pasj/psx080)
- 3215 Broughton, A., Utsumi, Y., Plazas Malagón, A. A., et al.
3216 2024, *PASP*, 136, 045003, doi: [10.1088/1538-3873/ad3aa2](https://doi.org/10.1088/1538-3873/ad3aa2)
- 3217 Burke, D. L., Rykoff, E. S., Allam, S., et al. 2018, *AJ*, 155,
3218 41, doi: [10.3847/1538-3881/aa9f22](https://doi.org/10.3847/1538-3881/aa9f22)
- 3219 Chambers, K. C., Magnier, E. A., Metcalfe, N., et al. 2016,
3220 *arXiv e-prints*, arXiv:1612.05560,
3221 doi: [10.48550/arXiv.1612.05560](https://doi.org/10.48550/arXiv.1612.05560)
- 3222 Choi, Y., Olsen, K. A. G., Carlin, J. L., et al. 2025, *arXiv*
3223 *e-prints*, arXiv:2507.01343,
3224 doi: [10.48550/arXiv.2507.01343](https://doi.org/10.48550/arXiv.2507.01343)
- 3225 de Vaucouleurs, G. 1948, *Annales d’Astrophysique*, 11, 247
- 3226 de Vaucouleurs, G. 1953, *MNRAS*, 113, 134,
3227 doi: [10.1093/mnras/113.2.134](https://doi.org/10.1093/mnras/113.2.134)
- 3228 Dowler, P., Bonnarel, F., & Tody, D. 2015, *IVOA Simple*
3229 *Image Access Version 2.0*, *IVOA Recommendation 23*
3230 *December 2015*
3231 doi: [10.5479/ADS/bib/2015ivoa.spec.1223D](https://doi.org/10.5479/ADS/bib/2015ivoa.spec.1223D)
- 3232 Dowler, P., Rixon, G., Tody, D., & Demleitner, M. 2019,
3233 *Table Access Protocol Version 1.1*, *IVOA*
3234 *Recommendation 27 September 2019*
3235 doi: [10.5479/ADS/bib/2019ivoa.spec.0927D](https://doi.org/10.5479/ADS/bib/2019ivoa.spec.0927D)
- 3236 Eggl, S., Juric, M., Moeyens, J., & Jones, L. 2020, in
3237 *AAS/Division for Planetary Sciences Meeting Abstracts*,
3238 *Vol. 52, AAS/Division for Planetary Sciences Meeting*
3239 *Abstracts*, 211.01
- 3240 Esteves, J. H., Utsumi, Y., Snyder, A., et al. 2023, *PASP*,
3241 135, 115003, doi: [10.1088/1538-3873/ad0a73](https://doi.org/10.1088/1538-3873/ad0a73)
- 3242 Euclid Collaboration, Romelli, E., Kümmel, M., et al. 2025,
3243 *arXiv e-prints*, arXiv:2503.15305,
3244 doi: [10.48550/arXiv.2503.15305](https://doi.org/10.48550/arXiv.2503.15305)
- 3245 Fagrelis, P., & Rykoff, E. S. 2025, *Rubin Observatory*
3246 *Baseline Calibration Plan, Commissioning Technical*
3247 *Note SITCOMTN-086, NSF-DOE Vera C. Rubin*
3248 *Observatory*, doi: [10.71929/rubin/2583850](https://doi.org/10.71929/rubin/2583850)
- 3249 Ferguson, P. S., Rykoff, E. S., Carlin, J. L., Saunders, C., &
3250 Parejko, J. K. 2025, *The Monster: A reference catalog*
3251 *with synthetic ugrizy-band fluxes for the Vera C. Rubin*
3252 *observatory, Data Management Technical Note*
3253 *DMTN-277, NSF-DOE Vera C. Rubin Observatory*,
3254 doi: [10.71929/rubin/2583688](https://doi.org/10.71929/rubin/2583688)
- 3255 Fernique, P., Allen, M. G., Boch, T., et al. 2015, *A&A*, 578,
3256 A114, doi: [10.1051/0004-6361/201526075](https://doi.org/10.1051/0004-6361/201526075)
- 3257 Fernique, P., Allen, M., Boch, T., et al. 2017, *HiPS -*
3258 *Hierarchical Progressive Survey Version 1.0*, *IVOA*
3259 *Recommendation 19 May 2017*
3260 doi: [10.5479/ADS/bib/2017ivoa.spec.0519F](https://doi.org/10.5479/ADS/bib/2017ivoa.spec.0519F)
- 3261 Fortino, W. F., Bernstein, G. M., Bernardinelli, P. H., et al.
3262 2021, *AJ*, 162, 106, doi: [10.3847/1538-3881/ac0722](https://doi.org/10.3847/1538-3881/ac0722)
- 3263 Gaia Collaboration, Montegriffo, P., Bellazzini, M., et al.
3264 2023a, *A&A*, 674, A33,
3265 doi: [10.1051/0004-6361/202243709](https://doi.org/10.1051/0004-6361/202243709)
- 3266 Gaia Collaboration, Vallenari, A., Brown, A. G. A., et al.
3267 2023b, *A&A*, 674, A1, doi: [10.1051/0004-6361/202243940](https://doi.org/10.1051/0004-6361/202243940)
- 3268 Górski, K. M., Hivon, E., Banday, A. J., et al. 2005, *ApJ*,
3269 622, 759, doi: [10.1086/427976](https://doi.org/10.1086/427976)
- 3270 Graham, A. W., & Driver, S. P. 2005, *PASA*, 22, 118,
3271 doi: [10.1071/AS05001](https://doi.org/10.1071/AS05001)
- 3272 Graham, M., Plante, R., Tody, D., & Fitzpatrick, M. 2014,
3273 *PyVO: Python access to the Virtual Observatory*,,
3274 *Astrophysics Source Code Library*, record ascl:1402.004
- 3275 Graham, M. L., Carlin, J. L., Adair, C. L., et al. 2025,
3276 *Guidelines for User Tutorials, Technical Note RTN-045*,
3277 *NSF-DOE Vera C. Rubin Observatory*,
3278 doi: [10.71929/rubin/2584020](https://doi.org/10.71929/rubin/2584020)
- 3279 Gray, B. 2025, *find_orb: Orbit determination from*
3280 *observations*, https://github.com/Bill-Gray/find_orb
- 3281 Guy, L. P., Bechtol, K., Bellm, E., et al. 2026, *Rubin*
3282 *Observatory Plans for an Early Science Program*,
3283 *Technical Note RTN-011, NSF-DOE Vera C. Rubin*
3284 *Observatory*, doi: [10.71929/rubin/2584021](https://doi.org/10.71929/rubin/2584021)
- 3285 Heinze, A., Eggl, S., Juric, M., et al. 2022, in *AAS/Division*
3286 *for Planetary Sciences Meeting Abstracts, Vol. 54*,
3287 *AAS/Division for Planetary Sciences Meeting Abstracts*,
3288 504.04
- 3289 Heinze, A., Juric, M., & Kurlander, J. 2023, *heliolinx: Open*
3290 *Source Solar System Discovery Software*,
3291 <https://github.com/heliolinx/heliolinx>
- 3292 Hirata, C., & Seljak, U. 2003, *MNRAS*, 343, 459,
3293 doi: [10.1046/j.1365-8711.2003.06683.x](https://doi.org/10.1046/j.1365-8711.2003.06683.x)
- 3294 Holman, M. J., Payne, M. J., Blankley, P., Janssen, R., &
3295 Kuindersma, S. 2018, *AJ*, 156, 135,
3296 doi: [10.3847/1538-3881/aad69a](https://doi.org/10.3847/1538-3881/aad69a)

- 3297 Howard, J., Reil, K., Claver, C., et al. 2018, in Society of
3298 Photo-Optical Instrumentation Engineers (SPIE)
3299 Conference Series, Vol. 10700, Ground-based and
3300 Airborne Telescopes VII, ed. H. K. Marshall &
3301 J. Spyromilio, 107003D, doi: [10.1117/12.2312684](https://doi.org/10.1117/12.2312684)
- 3302 Illingworth, G., Magee, D., Bouwens, R., et al. 2016, arXiv
3303 e-prints, arXiv:1606.00841,
3304 doi: [10.48550/arXiv.1606.00841](https://doi.org/10.48550/arXiv.1606.00841)
- 3305 Ingraham, P., Fagrelus, P., Stubbs, C. W., et al. 2022, in
3306 Society of Photo-Optical Instrumentation Engineers
3307 (SPIE) Conference Series, Vol. 12182, Ground-based and
3308 Airborne Telescopes IX, ed. H. K. Marshall,
3309 J. Spyromilio, & T. Usuda, 121820R,
3310 doi: [10.1117/12.2630185](https://doi.org/10.1117/12.2630185)
- 3311 Ivezić, Ž., Kahn, S. M., Tyson, J. A., et al. 2019a, ApJ,
3312 873, 111, doi: [10.3847/1538-4357/ab042c](https://doi.org/10.3847/1538-4357/ab042c)
- 3313 Ivezić, Ž., Kahn, S. M., Tyson, J. A., et al. 2019b, ApJ,
3314 873, 111, doi: [10.3847/1538-4357/ab042c](https://doi.org/10.3847/1538-4357/ab042c)
- 3315 Jarvis, M., et al. 2021, Mon. Not. Roy. Astron. Soc., 501,
3316 1282, doi: [10.1093/mnras/staa3679](https://doi.org/10.1093/mnras/staa3679)
- 3317 Jenness, T., & Dubois-Felsmann, G. P. 2025, IVOA
3318 Identifier Usage at the Rubin Observatory, Data
3319 Management Technical Note DMTN-302, NSF-DOE Vera
3320 C. Rubin Observatory, doi: [10.71929/rubin/2583848](https://doi.org/10.71929/rubin/2583848)
- 3321 Jenness, T., Voutsinas, S., Dubois-Felsmann, G. P., &
3322 Salnikov, A. 2024, arXiv e-prints, arXiv:2501.00544,
3323 doi: [10.48550/arXiv.2501.00544](https://doi.org/10.48550/arXiv.2501.00544)
- 3324 Jenness, T., Bosch, J. F., Salnikov, A., et al. 2022, in
3325 Society of Photo-Optical Instrumentation Engineers
3326 (SPIE) Conference Series, Vol. 12189, Software and
3327 Cyberinfrastructure for Astronomy VII, 1218911,
3328 doi: [10.1117/12.2629569](https://doi.org/10.1117/12.2629569)
- 3329 Jones, R. L., Yoachim, P., Ivezić, Ž., Neilsen Jr., E. H., &
3330 Ribeiro, T. 2021, Survey Strategy and Cadence Choices
3331 for the Vera C. Rubin Observatory Legacy Survey of
3332 Space and Time (LSST), Project Science Technical Note
3333 PSTN-051, NSF-DOE Vera C. Rubin Observatory,
3334 doi: [10.71929/rubin/2584084](https://doi.org/10.71929/rubin/2584084)
- 3335 Juric, M. 2025, mpsky: Multi-purpose sky catalog
3336 cross-matching, <https://github.com/mjuric/mpsky>
- 3337 Jurić, M., Ciardi, D., Dubois-Felsmann, G., & Guy, L.
3338 2019, LSST Science Platform Vision Document, Systems
3339 Engineering Controlled Document LSE-319, NSF-DOE
3340 Vera C. Rubin Observatory, doi: [10.71929/rubin/2587242](https://doi.org/10.71929/rubin/2587242)
- 3341 Jurić, M., Axelrod, T. S., Becker, A. C., et al. 2023, Data
3342 Products Definition Document, Systems Engineering
3343 Controlled Document LSE-163, NSF-DOE Vera C. Rubin
3344 Observatory, doi: [10.71929/rubin/2587118](https://doi.org/10.71929/rubin/2587118)
- 3345 Kannawadi, A. 2025, Consistent galaxy colors with
3346 Gaussian-Aperture and PSF photometry, Data
3347 Management Technical Note DMTN-190, NSF-DOE Vera
3348 C. Rubin Observatory, doi: [10.71929/rubin/2583849](https://doi.org/10.71929/rubin/2583849)
- 3349 Kron, R. G. 1980, ApJS, 43, 305, doi: [10.1086/190669](https://doi.org/10.1086/190669)
- 3350 Kuijken, K. 2008, A&A, 482, 1053,
3351 doi: [10.1051/0004-6361:20066601](https://doi.org/10.1051/0004-6361:20066601)
- 3352 Lange, T., Nordby, M., Pollek, H., et al. 2024, in Society of
3353 Photo-Optical Instrumentation Engineers (SPIE)
3354 Conference Series, Vol. 13096, Ground-based and
3355 Airborne Instrumentation for Astronomy X, ed. J. J.
3356 Bryant, K. Motohara, & J. R. D. Vernet, 130961O,
3357 doi: [10.1117/12.3019302](https://doi.org/10.1117/12.3019302)
- 3358 Léget, P. F., Astier, P., Regnault, N., et al. 2021, A&A,
3359 650, A81, doi: [10.1051/0004-6361/202140463](https://doi.org/10.1051/0004-6361/202140463)
- 3360 Lim, K.-T. 2023, Proposal and Prototype for Prompt
3361 Processing, Data Management Technical Note
3362 DMTN-219, NSF-DOE Vera C. Rubin Observatory,
3363 doi: [10.71929/rubin/2585429](https://doi.org/10.71929/rubin/2585429)
- 3364 Louys, M., Tody, D., Dowler, P., et al. 2017, Observation
3365 Data Model Core Components, its Implementation in the
3366 Table Access Protocol Version 1.1., IVOA
3367 Recommendation 09 May 2017
3368 doi: [10.5479/ADS/bib/2017ivoa.spec.0509L](https://doi.org/10.5479/ADS/bib/2017ivoa.spec.0509L)
- 3369 LSST Dark Energy Science Collaboration (LSST DESC),
3370 Abolfathi, B., Alonso, D., et al. 2021, ApJS, 253, 31,
3371 doi: [10.3847/1538-4365/abd62c](https://doi.org/10.3847/1538-4365/abd62c)
- 3372 Lupton, R., Blanton, M. R., Fekete, G., et al. 2004, PASP,
3373 116, 133, doi: [10.1086/382245](https://doi.org/10.1086/382245)
- 3374 Lust, N. B., Jenness, T., Bosch, J. F., et al. 2023, arXiv
3375 e-prints, arXiv:2303.03313,
3376 doi: [10.48550/arXiv.2303.03313](https://doi.org/10.48550/arXiv.2303.03313)
- 3377 Mandelbaum, R., Hirata, C. M., Seljak, U., et al. 2005,
3378 MNRAS, 361, 1287,
3379 doi: [10.1111/j.1365-2966.2005.09282.x](https://doi.org/10.1111/j.1365-2966.2005.09282.x)
- 3380 Megias Homar, G., Kahn, S. M., Meyers, J. M., Crenshaw,
3381 J. F., & Thomas, S. J. 2024, The Astrophysical Journal,
3382 974, 108, doi: [10.3847/1538-4357/ad6cdc](https://doi.org/10.3847/1538-4357/ad6cdc)
- 3383 Megias Homar, G., Tighe, R., Thomas, S., et al. 2024, in
3384 Ground-based and Airborne Telescopes X, ed. H. K.
3385 Marshall, J. Spyromilio, & T. Usuda, Vol. 13094,
3386 International Society for Optics and Photonics (SPIE),
3387 130943C, doi: [10.1117/12.3019031](https://doi.org/10.1117/12.3019031)
- 3388 Melchior, P., Moolekamp, F., Jerdee, M., et al. 2018,
3389 Astronomy and Computing, 24, 129,
3390 doi: [10.1016/j.ascom.2018.07.001](https://doi.org/10.1016/j.ascom.2018.07.001)
- 3391 Mueller, F., et al. 2023, in ASP Conf. Ser., Vol. TBD,
3392 ADASS XXXII, ed. S. Gaudet, S. Gwyn, P. Dowler,
3393 D. Bohlender, & A. Hincks (San Francisco: ASP), in
3394 press. <https://dmtn-243.lsst.io>

- 3395 Naghib, E., Yoachim, P., Vanderbei, R. J., Connolly, A. J.,
3396 & Jones, R. L. 2019, *The Astronomical Journal*, 157, 151,
3397 doi: [10.3847/1538-3881/aafece](https://doi.org/10.3847/1538-3881/aafece)
- 3398 NSF-DOE Vera C. Rubin Observatory. 2021, Rubin
3399 Observatory LSST Tutorials [Computer Software],
3400 NSF-DOE Vera C. Rubin Observatory,
3401 doi: [10.11578/rubin/dc.20250909.20](https://doi.org/10.11578/rubin/dc.20250909.20)
- 3402 NSF-DOE Vera C. Rubin Observatory. 2025a, Legacy
3403 Survey of Space and Time Data Preview 1 [Data set],
3404 NSF-DOE Vera C. Rubin Observatory,
3405 doi: [10.71929/RUBIN/2570308](https://doi.org/10.71929/RUBIN/2570308)
- 3406 NSF-DOE Vera C. Rubin Observatory. 2025b, Legacy
3407 Survey of Space and Time Data Preview 1: raw dataset
3408 type [Data set], NSF-DOE Vera C. Rubin Observatory,
3409 doi: [10.71929/RUBIN/2570310](https://doi.org/10.71929/RUBIN/2570310)
- 3410 NSF-DOE Vera C. Rubin Observatory. 2025c, Legacy
3411 Survey of Space and Time Data Preview 1: visit_image
3412 dataset type [Data set], NSF-DOE Vera C. Rubin
3413 Observatory, doi: [10.71929/RUBIN/2570311](https://doi.org/10.71929/RUBIN/2570311)
- 3414 NSF-DOE Vera C. Rubin Observatory. 2025d, Legacy
3415 Survey of Space and Time Data Preview 1: deep_coadd
3416 dataset type [Data set], NSF-DOE Vera C. Rubin
3417 Observatory, doi: [10.71929/RUBIN/2570313](https://doi.org/10.71929/RUBIN/2570313)
- 3418 NSF-DOE Vera C. Rubin Observatory. 2025e, Legacy
3419 Survey of Space and Time Data Preview 1:
3420 template_coadd dataset type [Data set], NSF-DOE Vera
3421 C. Rubin Observatory, doi: [10.71929/RUBIN/2570314](https://doi.org/10.71929/RUBIN/2570314)
- 3422 NSF-DOE Vera C. Rubin Observatory. 2025f, Legacy
3423 Survey of Space and Time Data Preview 1:
3424 difference_image dataset type [Data set], NSF-DOE Vera
3425 C. Rubin Observatory, doi: [10.71929/RUBIN/2570312](https://doi.org/10.71929/RUBIN/2570312)
- 3426 NSF-DOE Vera C. Rubin Observatory. 2025g, Legacy
3427 Survey of Space and Time Data Preview 1: Source
3428 searchable catalog [Data set], NSF-DOE Vera C. Rubin
3429 Observatory, doi: [10.71929/RUBIN/2570323](https://doi.org/10.71929/RUBIN/2570323)
- 3430 NSF-DOE Vera C. Rubin Observatory. 2025h, Legacy
3431 Survey of Space and Time Data Preview 1: Object
3432 searchable catalog [Data set], NSF-DOE Vera C. Rubin
3433 Observatory, doi: [10.71929/RUBIN/2570325](https://doi.org/10.71929/RUBIN/2570325)
- 3434 NSF-DOE Vera C. Rubin Observatory. 2025i, Legacy
3435 Survey of Space and Time Data Preview 1: ForcedSource
3436 searchable catalog [Data set], NSF-DOE Vera C. Rubin
3437 Observatory, doi: [10.71929/RUBIN/2570327](https://doi.org/10.71929/RUBIN/2570327)
- 3438 NSF-DOE Vera C. Rubin Observatory. 2025j, Legacy
3439 Survey of Space and Time Data Preview 1: DiaSource
3440 searchable catalog [Data set], NSF-DOE Vera C. Rubin
3441 Observatory, doi: [10.71929/RUBIN/2570317](https://doi.org/10.71929/RUBIN/2570317)
- 3442 NSF-DOE Vera C. Rubin Observatory. 2025k, Legacy
3443 Survey of Space and Time Data Preview 1: DiaObject
3444 searchable catalog [Data set], NSF-DOE Vera C. Rubin
3445 Observatory, doi: [10.71929/RUBIN/2570319](https://doi.org/10.71929/RUBIN/2570319)
- 3446 NSF-DOE Vera C. Rubin Observatory. 2025l, Legacy
3447 Survey of Space and Time Data Preview 1:
3448 ForcedSourceOnDiaObject searchable catalog [Data set],
3449 NSF-DOE Vera C. Rubin Observatory,
3450 doi: [10.71929/RUBIN/2570321](https://doi.org/10.71929/RUBIN/2570321)
- 3451 NSF-DOE Vera C. Rubin Observatory. 2025m, Legacy
3452 Survey of Space and Time Data Preview 1: SSOBJECT
3453 searchable catalog [Data set], NSF-DOE Vera C. Rubin
3454 Observatory, doi: [10.71929/RUBIN/2570335](https://doi.org/10.71929/RUBIN/2570335)
- 3455 NSF-DOE Vera C. Rubin Observatory. 2025n, Legacy
3456 Survey of Space and Time Data Preview 1: SSSource
3457 searchable catalog [Data set], NSF-DOE Vera C. Rubin
3458 Observatory, doi: [10.71929/RUBIN/2570333](https://doi.org/10.71929/RUBIN/2570333)
- 3459 NSF-DOE Vera C. Rubin Observatory. 2025o, Legacy
3460 Survey of Space and Time Data Preview 1: CcdVisit
3461 searchable catalog [Data set], NSF-DOE Vera C. Rubin
3462 Observatory, doi: [10.71929/RUBIN/2570331](https://doi.org/10.71929/RUBIN/2570331)
- 3463 NSF-DOE Vera C. Rubin Observatory. 2025p, Legacy
3464 Survey of Space and Time Data Preview 1: survey
3465 property dataset type [Data set], NSF-DOE Vera C.
3466 Rubin Observatory, doi: [10.71929/RUBIN/2570315](https://doi.org/10.71929/RUBIN/2570315)
- 3467 Oke, J. B., & Gunn, J. E. 1983, *ApJ*, 266, 713,
3468 doi: [10.1086/160817](https://doi.org/10.1086/160817)
- 3469 O'Mullane, W., Economou, F., Huang, F., et al. 2024a, in
3470 *Astronomical Society of the Pacific Conference Series*,
3471 Vol. 535, *Astronomical Data Analysis Software and Systems*
3472 XXXI, ed. B. V. Hugo, R. Van Rooyen, & O. M.
3473 Smirnov, 227, doi: [10.48550/arXiv.2111.15030](https://doi.org/10.48550/arXiv.2111.15030)
- 3474 O'Mullane, W., AlSayyad, Y., Chiang, J., et al. 2024b, in
3475 *Society of Photo-Optical Instrumentation Engineers*
3476 (SPIE) Conference Series, Vol. 13101, *Software and*
3477 *Cyberinfrastructure for Astronomy VIII*, ed. J. Ibsen &
3478 G. Chiozzi, 131012B, doi: [10.1117/12.3018005](https://doi.org/10.1117/12.3018005)
- 3479 Onken, C. A., Wolf, C., Bessell, M. S., et al. 2019, *PASA*,
3480 36, e033, doi: [10.1017/pasa.2019.27](https://doi.org/10.1017/pasa.2019.27)
- 3481 Park, H. Y., Nomerotski, A., & Tsybychev, D. 2017,
3482 *Journal of Instrumentation*, 12, C05015,
3483 doi: [10.1088/1748-0221/12/05/C05015](https://doi.org/10.1088/1748-0221/12/05/C05015)
- 3484 Petrosian, V. 1976, *ApJL*, 210, L53,
3485 doi: [10.1086/18230110.1086/182253](https://doi.org/10.1086/18230110.1086/182253)
- 3486 Plazas, A. A., Shapiro, C., Smith, R., Huff, E., & Rhodes,
3487 J. 2018, *Publications of the Astronomical Society of the*
3488 *Pacific*, 130, 065004, doi: [10.1088/1538-3873/aab820](https://doi.org/10.1088/1538-3873/aab820)

- 3489 Plazas Malagón, A. A., Digel, S. W., Roodman, A.,
3490 Broughton, A., & LSST Camera Team. 2025, LSSTCam
3491 and LSSTComCam Focal Plane Layouts, Camera
3492 Technical Note CTN-001, NSF-DOE Vera C. Rubin
3493 Observatory, doi: [10.71929/rubin/2584019](https://doi.org/10.71929/rubin/2584019)
- 3494 Plazas Malagón, A. A., Waters, C., Broughton, A., et al.
3495 2025, *Journal of Astronomical Telescopes, Instruments,
3496 and Systems*, 11, 011209,
3497 doi: [10.1117/1.JATIS.11.1.011209](https://doi.org/10.1117/1.JATIS.11.1.011209)
- 3498 Refregier, A. 2003, *ARA&A*, 41, 645,
3499 doi: [10.1146/annurev.astro.41.111302.102207](https://doi.org/10.1146/annurev.astro.41.111302.102207)
- 3500 Reiss, D. J., & Lupton, R. H. 2016, Implementation of
3501 Image Difference Decorrelation, Data Management
3502 Technical Note DMTN-021, NSF-DOE Vera C. Rubin
3503 Observatory, doi: [10.71929/rubin/2586490](https://doi.org/10.71929/rubin/2586490)
- 3504 Roodman, A., Rasmussen, A., Bradshaw, A., et al. 2024, in
3505 Society of Photo-Optical Instrumentation Engineers
3506 (SPIE) Conference Series, Vol. 13096, Ground-based and
3507 Airborne Instrumentation for Astronomy X, ed. J. J.
3508 Bryant, K. Motohara, & J. R. D. Vernet, 130961S,
3509 doi: [10.1117/12.3019698](https://doi.org/10.1117/12.3019698)
- 3510 Rubin, V. C., & Ford, Jr., W. K. 1970, *ApJ*, 159, 379,
3511 doi: [10.1086/150317](https://doi.org/10.1086/150317)
- 3512 Rubin, V. C., Ford, Jr., W. K., & Thonnard, N. 1980, *ApJ*,
3513 238, 471, doi: [10.1086/158003](https://doi.org/10.1086/158003)
- 3514 Rubin Observatory Science Pipelines Developers. 2025, The
3515 LSST Science Pipelines Software: Optical Survey
3516 Pipeline Reduction and Analysis Environment, Project
3517 Science Technical Note PSTN-019, NSF-DOE Vera C.
3518 Rubin Observatory, doi: [10.71929/rubin/2570545](https://doi.org/10.71929/rubin/2570545)
- 3519 Rubin's Survey Cadence Optimization Committee, Bauer,
3520 F. E., Brough, S., et al. 2022, Survey Cadence
3521 Optimization Committee's Phase 1 Recommendation,
3522 Project Science Technical Note PSTN-053, NSF-DOE
3523 Vera C. Rubin Observatory, doi: [10.71929/rubin/2584276](https://doi.org/10.71929/rubin/2584276)
- 3524 Rubin's Survey Cadence Optimization Committee, Bauer,
3525 F. E., Bianco, F. B., et al. 2023, Survey Cadence
3526 Optimization Committee's Phase 2 Recommendations,
3527 Project Science Technical Note PSTN-055, NSF-DOE
3528 Vera C. Rubin Observatory, doi: [10.71929/rubin/2585249](https://doi.org/10.71929/rubin/2585249)
- 3529 Rubin's Survey Cadence Optimization Committee, Bianco,
3530 F. B., Jones, R. L., et al. 2025, Survey Cadence
3531 Optimization Committee's Phase 3 Recommendations,
3532 Project Science Technical Note PSTN-056, NSF-DOE
3533 Vera C. Rubin Observatory, doi: [10.71929/rubin/2585402](https://doi.org/10.71929/rubin/2585402)
- 3534 Rykoff, E. S., Tucker, D. L., Burke, D. L., et al. 2023, arXiv
3535 e-prints, arXiv:2305.01695,
3536 doi: [10.48550/arXiv.2305.01695](https://doi.org/10.48550/arXiv.2305.01695)
- 3537 Saunders, C. 2024, Astrometric Calibration in the LSST
3538 Pipeline, Data Management Technical Note DMTN-266,
3539 NSF-DOE Vera C. Rubin Observatory,
3540 doi: [10.71929/rubin/2583846](https://doi.org/10.71929/rubin/2583846)
- 3541 Schutt, T., Jarvis, M., Roodman, A., et al. 2025, The Open
3542 Journal of Astrophysics, 8, 26, doi: [10.33232/001c.132299](https://doi.org/10.33232/001c.132299)
- 3543 Sérsic, J. L. 1963, Boletín de la Asociacion Argentina de
3544 Astronomia La Plata Argentina, 6, 41
- 3545 Sersic, J. L. 1968, Atlas de Galaxias Australes (Cordoba,
3546 Argentina: Observatorio Astronomico)
- 3547 Shanks, T., Metcalfe, N., Chehade, B., et al. 2015,
3548 *MNRAS*, 451, 4238, doi: [10.1093/mnras/stv1130](https://doi.org/10.1093/mnras/stv1130)
- 3549 SLAC National Accelerator Laboratory, & NSF-DOE Vera
3550 C. Rubin Observatory. 2024, LSST Commissioning
3551 Camera, SLAC National Accelerator Laboratory (SLAC),
3552 Menlo Park, CA (United States),
3553 doi: [10.71929/RUBIN/2561361](https://doi.org/10.71929/RUBIN/2561361)
- 3554 Slater, C. T., Ivezić, Ž., & Lupton, R. H. 2020, *AJ*, 159, 65,
3555 doi: [10.3847/1538-3881/ab6166](https://doi.org/10.3847/1538-3881/ab6166)
- 3556 Smith, G. E. 2010, *Rev. Mod. Phys.*, 82, 2307,
3557 doi: [10.1103/RevModPhys.82.2307](https://doi.org/10.1103/RevModPhys.82.2307)
- 3558 Stalder, B., Reil, K., Claver, C., et al. 2020, in Society of
3559 Photo-Optical Instrumentation Engineers (SPIE)
3560 Conference Series, Vol. 11447, Ground-based and
3561 Airborne Instrumentation for Astronomy VIII, ed. C. J.
3562 Evans, J. J. Bryant, & K. Motohara, 114470L,
3563 doi: [10.1117/12.2561132](https://doi.org/10.1117/12.2561132)
- 3564 Stalder, B., Reil, K., Aguilar, C., et al. 2022, in Society of
3565 Photo-Optical Instrumentation Engineers (SPIE)
3566 Conference Series, Vol. 12184, Ground-based and
3567 Airborne Instrumentation for Astronomy IX, ed. C. J.
3568 Evans, J. J. Bryant, & K. Motohara, 121840J,
3569 doi: [10.1117/12.2630184](https://doi.org/10.1117/12.2630184)
- 3570 Stalder, B., Munoz, F., Aguilar, C., et al. 2024, in Society
3571 of Photo-Optical Instrumentation Engineers (SPIE)
3572 Conference Series, Vol. 13094, Ground-based and
3573 Airborne Telescopes X, ed. H. K. Marshall, J. Spyromilio,
3574 & T. Usuda, 1309409, doi: [10.1117/12.3019266](https://doi.org/10.1117/12.3019266)
- 3575 Swinbank, J. D., Axelrod, T. S., Becker, A. C., et al. 2020,
3576 Data Management Science Pipelines Design, Data
3577 Management Controlled Document LDM-151, NSF-DOE
3578 Vera C. Rubin Observatory, doi: [10.71929/rubin/2587108](https://doi.org/10.71929/rubin/2587108)
- 3579 Taranu, D. S. 2025, The MultiProFit astronomical source
3580 modelling code, Data Management Technical Note
3581 DMTN-312, NSF-DOE Vera C. Rubin Observatory,
3582 doi: [10.71929/rubin/2584108](https://doi.org/10.71929/rubin/2584108)
- 3583 Taylor, M. 2011, TOPCAT: Tool for OPerations on
3584 Catalogues And Tables,, *Astrophysics Source Code
3585 Library*, record ascl:1101.010

- 3586 Thomas, S., Connolly, A., Crenshaw, J. F., et al. 2023, in
3587 Adaptive Optics for Extremely Large Telescopes
3588 (AO4ELT7), 67, doi: [10.13009/AO4ELT7-2023-069](https://doi.org/10.13009/AO4ELT7-2023-069)
- 3589 Tonry, J. L., Denneau, L., Heinze, A. N., et al. 2018, PASP,
3590 130, 064505, doi: [10.1088/1538-3873/aabadf](https://doi.org/10.1088/1538-3873/aabadf)
- 3591 Wainer, T. M., Davenport, J. R. A., Bellm, E. C., et al.
3592 2025, Research Notes of the American Astronomical
3593 Society, 9, 171, doi: [10.3847/2515-5172/adecef](https://doi.org/10.3847/2515-5172/adecef)
- 3594 Wang, D. L., Monkewitz, S. M., Lim, K.-T., & Becla, J.
3595 2011, in State of the Practice Reports, SC '11 (New
3596 York, NY, USA: ACM), 12:1–12:11,
3597 doi: [10.1145/2063348.2063364](https://doi.org/10.1145/2063348.2063364)
- 3598 Waters, C. Z., Magnier, E. A., Price, P. A., et al. 2020,
3599 ApJS, 251, 4, doi: [10.3847/1538-4365/abb82b](https://doi.org/10.3847/1538-4365/abb82b)
- 3600 Whitaker, K. E., Ashas, M., Illingworth, G., et al. 2019,
3601 ApJS, 244, 16, doi: [10.3847/1538-4365/ab3853](https://doi.org/10.3847/1538-4365/ab3853)
- 3602 Wu, X., Roby, W., Goldian, T., et al. 2019, in Astronomical
3603 Society of the Pacific Conference Series, Vol. 521,
3604 Astronomical Data Analysis Software and Systems
3605 XXVI, ed. M. Molinaro, K. Shortridge, & F. Pasian, 32
3606 Xin, B., Claver, C., Liang, M., et al. 2015, ApOpt, 54,
3607 9045, doi: [10.1364/AO.54.009045](https://doi.org/10.1364/AO.54.009045)
- 3608 Yoachim, P. 2022, Survey Strategy: Rolling Cadence,
3609 Project Science Technical Note PSTN-052, NSF-DOE
3610 Vera C. Rubin Observatory, doi: [10.71929/rubin/2584109](https://doi.org/10.71929/rubin/2584109)
- 3611 Yoachim, P., Jones, L., Eric H. Neilsen, J., & Becker, M. R.
3612 2024, lsst/rubin_scheduler: v3.0.0, v3.0.0 Zenodo,
3613 doi: [10.5281/zenodo.13985198](https://doi.org/10.5281/zenodo.13985198)
- 3614 Zhang, T., Almoubayyed, H., Mandelbaum, R., et al. 2023,
3615 MNRAS, 520, 2328, doi: [10.1093/mnras/stac3350](https://doi.org/10.1093/mnras/stac3350)